Mathematical Models for Manoeuvring under Realistic Environmental Conditions

Von der Fakultät für Ingenieurwissenschaften, Abteilung Maschinenbau und Verfahrenstechnik

der

Universität Duisburg-Essen

zur Erlangung des akademischen Grades

eines

Doktors der Ingenieurwissenschaften

Dr.-Ing.

genehmigte Dissertation

von

Guillermo Arquímedes Vásquez Chillcce

aus

Perú

Gutachter: Prof. Dr.-Ing. Bettar Ould el Moctar

Prof. Dr. Hironori Yasukawa

Tag der mündlichen Prüfung: 31 Oktober 2023

Mathematical Models for Manoeuvring under Realistic Environmental Conditions

by

Guillermo Arquímedes Vásquez Chillcce

Examiners: Prof. Dr.-Ing. Bettar Ould el Moctar
Prof. Dr. Hironori Yasukawa

Abstract

This thesis deals with the prediction of the manoeuvrability of surface ships under realistic environmental conditions. For this purpose, numerical methods for predicting the manoeuvrability of ships in shallow water and in waves were developed and validated. An essential prerequisite for predicting the manoeuvrability of ships is the knowledge of the hydrodynamic forces and moments acting on a ship. Therefore, efficient mathematical models were developed in this work. First, a direct system identification method for fully appended ships in shallow water was developed and validated. Second, a data-driven system identification method (indirect system identification) based on trajectories was developed and validated. Third, a procedure based on the Euler equations for calculating hydrodynamic added masses was co-developed and used. Finally, a model for the calculation of hydrodynamic forces and moments was developed and validated considering second-order wave forces. The majority of this work has been published in several papers in peer reviewed journals and conference proceedings.

Zusammenfassung

Diese Arbeit befasst sich mit der Vorhersage der Manövrierbarkeit von Überwasserschiffen unter realistischen Umgebungsbedingungen. Zu diesem Zweck wurden numerische Methoden zur Vorhersage der Manövrierbarkeit von Schiffen im Flachwasser und in Wellen entwickelt und validiert. Eine wesentliche Voraussetzung für die Prognose der Manövrierbarkeit von Schiffen ist die Kenntnis der auf ein Schiff wirkenden hydrodynamischen Kräfte und Momente. Aus diesem Grund wurden in dieser Arbeit effiziente mathematische Modelle entwickelt. Zunächst wurde eine direkte Systemidentifikationsmethode für Schiffe mit Anhängen im Flachwasser entwickelt und validiert. Anschließend wurde eine datenbasierte Systemidentifikationsmethode (indirekte Systemidentifikation) auf der Grundlage von Trajektorien entwickelt und validiert. Darüber hinaus wurde eine Prozedur auf Grundlage der Euler-Gleichungen zur Berechnung von hydrodynamischen Massen mitentwickelt und eingesetzt. Schließlich wurde ein Modell zur Berechnung der hydrodynamischen Kräfte und Momente unter Berücksichtigung der Wellenkräfte zweiter Ordnung entwickelt und validiert. Der Großteil dieser Arbeit wurde in mehreren Publikationen in Fachzeitschriften und Konferenzbänden publiziert.

Acknowledgements

I would like to express my deepest gratitude to my supervisor, Professor Bettar Ould el Moctar, for his guidance and critical reflection on the work presented in this thesis. His insightful feedback has pushed me to sharpen my thinking. I am also grateful to Professor Hironori Yasukawa for his interest and critical reflection on my work. I would also like to extend my gratitude to Lahbib Zentari, Dr. Malte Riesner and Dr. Simon Mewes for their critical comments, meaningful discussions and scientific expertise, which allowed me to improve my research. I am also grateful to Dr. Udo Lantermann and Dr. Andreas Peters for the discussions on general scientific topics. I am also thankful to Dr. Thomas Schellin for critically reviewing the research work related to this thesis. Many thanks go out to all colleagues at the Institute of Ship Technology, Ocean Engineering and Transport Systems (ISMT) of the University of Duisburg-Essen for the collaborative work over the past years. My special thanks are to my family and my fiancé for their continuous support and motivation.

Declaration

Parts of the work described in this thesis have been previously published in the following references by the author:

- Chillcce, Guillermo and Ould el Moctar (2023). "Data-driven system identification of hydrodynamic manoeuvring coefficients from free running tests". In: *Physics of Fluids* 35, 057122. DOI: 10.1063/5.0148219
- Chillcce, Guillermo and Ould el Moctar (2022). "Viscous effects on squat". In: *Applied Ocean Research* 125, p. 103252. DOI: 10.1016/j.apor.2022.103252.
- Chillcce, Guillermo and Ould el Moctar (2018). "A numerical method for manoeuvring simulation in regular waves". In: *Ocean Engineering* 170, pp. 434-444. DOI: 10.1016/j.oceaneng.2018.09.047.
- Riesner, Malte, Guillermo Chillcce, and Ould el Moctar (2019). "Rankine source time domain method for nonlinear ship motions in steep oblique waves". In: *Ships and Offshore Structures* 14.3, pp. 295–308. DOI: 10.1080/17445302.2018.1498568.
- el Moctar, Ould, Udo Lantermann, and Guillermo Chillcce (2022). "An efficient and accurate approach for zero-frequency added mass for maneuvering simulations in deep and shallow water". In: *Applied Ocean Research* 126, p. 103259. DOI: 10.1016/j.apor.2022.103259.
- Chillcce, Guillermo, Ivana Martic, Manasés Tello Ruiz, Jorge Ramirez, Nastia Degiuli, and Ould el Moctar (2019). "RANS evaluation of the DTC's vertical motion sailing in finite water depth waves". In: *5th MASHCON: International conference on ship manoeuvring in shallow and confined water with non-exclusive focus on manoeuvring in waves, wind and current.* Conference proceedings, p.273-283.
- Martic, Ivana, Guillermo Chillcce, Manasés Tello Ruiz, Jorge Ramirez, Nastia Degiuli, and Ould el Moctar (2019). "Numerical assessment of added resistance in waves of the DTC container ship in finite water depths". In: *5th MASHCON*. Conference proceedings, p.273-283.

Contents

Acronyms

BEM	Boundary element method
BIE	Boundary integral equation
BVP	Boundary value problem
EFD	Experimental fluid dynamics
EEDI	The Energy Efficiency Design Index
FVM	Finite volume method
HRIC	High-resolution interface capturing
HSVA	Hamburg Ship Model Basin
ITTC	The International Towing Tank Conference
IMO	International Maritime Organization
CFD	Computational fluid dynamics
CFL	Courant-Friedrichs-Lewy
COG	Centre of gravity
CV	Control volume
DES	Detached-eddy simulation
DNS	Direct numerical simulation
DoF	Degrees of freedom
DST	Development Centre for Ship Technology and Transport System
DTC	Duisburg test case
KRISO	Korea Research Institute of Ships and Ocean Engineering
KVLCC2	KRISO Very Large Crude Carrier
LES	Large-eddy simulation
MARIN	Maritime Research Institute Netherlands
MARINTEK	Norwegian Marine Technology Research Institute
MMG	Manoeuvring Modelling Group
PMM	Planar motion mechanism
RANS	Reynolds-averaged Navier-Stokes
RIW	Reference inland waterway
RSM	Reynolds stress model

SST	Menter's Shear Stress Transport
VOF	Volume of fluid

Symbols

$(O\xi\eta\zeta)$	Inertial coordinate system fixed on earth with origin O and orthogonal axis ξ, η and ζ
$(oxyz)$	Non inertial coordinate system fixed on ship with origin o and orthogonal axis x, y and z
$\vec{\xi}_o$	Space vector tracking the point o, origin of the body-fixed reference frame, expressed in inertial coordinate system with component $(\xi_o, \eta_o, \zeta_o)^\intercal$
$\vec{\xi}_p$	Space vector from a generic point P expressed in inertial coordinate system $(O\xi\eta\zeta)$ with component $(\xi_p, \eta_p, \zeta_p)^\intercal$
$\vec{x}_p$	Space vector from a generic point P expressed in the body-fixed coordinate system $(oxyz)$ with component $(\xi_p, \eta_p, \zeta_p)^\intercal$
φ	Roll angle
θ	Pitch angle
ψ	Yaw angle
$\mathbf{T}(\varphi, \theta, \psi)$	Transformation matrix, from body-fixed coordinate system to inertial coordinate system
$\mathbf{S}_\phi$	Transformation matrix that only involves the roll angle ϕ
$\mathbf{S}_\theta$	Transformation matrix that only involves the pitch angle θ
$\mathbf{S}_\psi$	Transformation matrix that only involves the yaw angle ψ
$\vec{\Theta}$	Euler angle pseudo vector with components $(\varphi, \theta, \psi)^\intercal$
$\dot{\vec{\Theta}}$	Rate of change of the Euler angles psuedo vector with components $(\dot{\varphi}, \dot{\theta}, \dot{\psi})^\intercal$
$\vec{v}_o$	Ship velocity observed from the body-fixed coordinate system with components $(u, v, w)^\intercal$
$\dot{\vec{\xi}}_o$	Ship velocity observed from the inertial coordinate system with components $(\dot{\xi}, \dot{\eta}, \dot{\zeta})^\intercal$
$\vec{\omega}$	Ship angular velocity observed from the body-fixed coordinate system with components $(p, q, r)^\intercal$

$\vec{\Omega}$	Ship angular velocity observed from the inertial coordinate system with components $(\omega_x, \omega_y, \omega_z)^\intercal$
$\mathbf{S}(\varphi, \theta, \psi)$	Transformation matrix, that transform the rate of change of the Euler angles into the ship angular velocity obeserved from the body-fixed coordinate system
$\mathbf{R}(\varphi, \theta, \psi)$	Transformation matrix, that transform the rate of change of the Euler angles into the ship angular velocity obeserved from the inertial coordinate system
m	Ship mass or rigid body
$\vec{r}_G$	Position of the ship's centre of gravity in the body-fixed coordinate system with components $(x_G, y_G, z_G)^\intercal$
$\vec{\xi}_G$	Position of the ship's centre of gravity in the inertial coordinate system
$\vec{U}_G, \dot{\vec{\xi}}_G$	Velocity of the ship's centre of gravity observed from the inertial coordinate system
$\dot{\vec{U}}_G$	Acceleration of the ship's centre of gravity observed from the inertial coordinate system
$\vec{H}_G$	Ship angular momentum about the centre of gravity and expressed in the inertial coordinate system
$\vec{h}_G$	Ship angular momentum about the centre of gravity and expressed in the body-fixed coordinate system
$\vec{h}_o$	Ship angular momentum about the origin of the body-fixed coordinate system and expresed in body-fixed coordinate system
$\mathbf{I}_o$	Moment of inertia tensor about the origin of the body-fixed coordinate system with respect to the xyz axes
I_{xx}	Moment of inertia with respect to the x-axis
I_{yy}	Moment of inertia with respect to the y-axis
I_{zz}	Moment of inertia with respect to the z-axis
I_{xy}	Moment of inertia around y-axis when the ship rotates around x-axis
$\vec{F}$	Total external force expressed in the inertial coordinate system
$\vec{M}_o$	Total external moment about the point o expressed in the inertial coordinate system
$\vec{f}$	Total external force expressed in the body-fixed coordinate system with component $(X, Y, Z)^\intercal$

$\vec{m}_o$	Total external moment about point o expressed in the body-fixed coordinate system with components $(K, M, N)^\intercal$
u	Ship surge speed
v	Ship sway speed
w	Ship heave speed
p	Ship roll rotation rate
q	Ship pitch rotation rate
r	Ship yaw rotation rate
Sw	Skew symmetric matrix
F	Generalized external force
$\mathbf{F}_h$	Generalized hydrodynamic force
$\mathbf{F}_s$	Generalized hydrostatic force
$\mathbf{F}_g$	Generalized gravitational force
$\mathbf{F}_r$	Generalized force from other remaining external sources
g	Gravitational acceleration
$\vec{n}$	Vector normal to the ship surface
t	Time variable
ρ	Fluid density
V	Volume of a control volume (CV)
S	Surface enclosing a control volume
n	Normal vector to surface pointing outwads
v	Velocity vector of the fluid with components $(v_x, v_y, v_z)^\intercal$
$\boldsymbol{\tau}$	Viscous stress tensor
μ	Dynamic viscosity
D	Rate of strain tensor
μ_t	Turbulent eddy viscosity
k	Turbulent kinetic energy
ϕ	General scalar representation in finite volume methods
r_x	Refinament factor in x-axis
r_y	Refinament factor in y-axis
r_z	Refinament factor in z-axis
r_t	Refinament factor in time
Υ	Grid refinament ratio
δ_D	Discretization error
$U(\phi_i)$	Numerical uncertainty of the quantity ϕ with the i-th grid
$\phi(\mathbf{x}, t)$	Velocity potential depending on space and time

$\phi(\mathbf{x})$	Velocity potential depeding on space
U	Ship velocity magnitude
ζ	Wave elevation
$G(\mathbf{x}, \mathbf{x}_s)$	Green function or fundamental solution of the Laplace equation with source located at $\mathbf{x}_s$

1 Introduction

Two developments are currently revolutionizing the shipping industry. On the one hand, the International Maritime Organization (IMO) has committed itself to reducing the greenhouse gas emissions of the international shipping industry. The introduction of the energy efficiency design index (EEDI[1]) represents this effort and forces new ships to use more efficient equipment and engines. On the other hand, the economic, safety and environmental benefits of autonomous shipping have led to increased research into autonomous ships. This is particularly true for inland waterway ships, which operate in more controlled areas than seagoing vessels. Both developments require technological innovations of various ship components, but even more important is a better understanding of ship behaviour in realistic environmental conditions. This is because the environmental conditions constrain the operation of the ship and influence its motions. This thesis is part of the effort to understand ship behaviour, especially manoeuvring, in real environmental conditions.

1.1 Statement of the problem

Following the introduction of the EEDI, a debate began about the performance of ships in adverse environmental conditions. It was thought that reducing the installed power of a ship could undermine its manoeuvrability in adverse environmental conditions, such as in waves and wind. This risk is greater in coastal areas because, first, the shallow water depths alter the hydrodynamic manoeuvring behaviour of ships and second, the volume of ship traffic in the vicinity of ports or harbours is high. In response to these concerns, the IMO's Marine Environment Protection Committee has issued the "guidelines for determining minimum propulsion power to maintain the manoeuvrability of ships in adverse conditions." This has opened up a more technical discussion on how to assess the manoeuvrability of ships in realistic environmental conditions.

Predicting ship manoeuvring in realistic environmental conditions, such as manoeuvring simultaneously in shallow water and waves—manoeuvring in coastal areas—is not

[1] The Energy Efficiency Design Index (EEDI) was made mandatory for new ships with the adoption of amendments to MARPOL Annex VI (resolution MEPC.203(62)).

yet possible. The hydrodynamic modelling of such a situation has multiple layers of complexity that are difficult to handle. In the past, the study of ship dynamics was divided into seakeeping and manoeuvring aspects to reduce the complexity of dealing with manoeuvring in waves. Nowadays, the aim is to unify these two fields, but such a task is not easy, even in deep water conditions. Shigunov et al. (2018) presented the results of the "international benchmark study on numerical simulation methods for the prediction of manoeuvrability of ships in waves" (deep water). The main outcome was that none of the methods were able to predict the manoeuvrability of the ship in waves. This suggests that a considerable effort in research is needed to improve the accuracy of such predictions.

The problem has been divided into manoeuvring in shallow water in calm water conditions and manoeuvring in waves in deep water. Trying to solve separately this two-way problem could bring a better understanding of its unification. However, even when these two problems are treated separately, the hydrodynamic flows around the ship remain highly complex, especially when the interaction between hull, propeller and rudder is taken into account. For the manoeuvring in waves in deep water, a general theory of ship dynamics is being developed based on the theories proposed in the fields of seakeeping and manoeuvring. These theories are sometimes in conflict because the assumptions made for one field cannot be applied to the other or because the assumption cannot be generalized. Knowing this, it is also reasonable to review the assumptions made in modelling manoeuvring forces as well as the intermediate procedures used in calculating manoeuvring forces and evaluating them through the lens of generalized theory. Some potential aspects to be reviewed are the frequency dependence of the hydrodynamic manoeuvring coefficients, the validity of the mathematical model in shallow water, and the regression procedure to obtain the hydrodynamic coefficients.

Additional motivation comes from the autonomous ship industry, which is driving forward the study of manoeuvring in shallow water, in particular for inland waterway ships. An autonomous ship should be able to manoeuvre without human intervention in a variety of environmental conditions (current, wind, water depth). The water depth of rivers is of primary importance as it changes the manoeuvring characteristics of the ship. Therefore, a clear understanding of shallow water manoeuvring is needed to provide the autonomous ship with algorithms that can reliably predict the next dynamic state of the ship.

To date, a general theory of manoeuvring under realistic environmental conditions—considering wind, waves, currents and shallow water effects—is still under development. The hydrodynamic effects of hull, propeller and rudder and their interaction due to realistic environmental conditions are still unknown and much research is needed. In this

respect, numerical prediction of the manoeuvring of fully appended inland waterway ships in shallow water is missing, but it is essential for the progress of autonomous ship research.

1.2 Aim and scope

The aim of the thesis is to contribute to the accurate modelling of manoeuvring forces, leading to a better numerical prediction of manoeuvring under realistic environmental conditions.

The scope of this work is limited to two main environmental conditions: water depth and regular waves. Strictly speaking, regular waves are not a realistic condition, but rather an idealized, non-trivial sea condition in which new numerical methods can be tested. Shallow water manoeuvring is focused on inland waterway ships, and manoeuvring in waves is focused on seagoing ships in deep waters. No consideration is given to seaway or wind. These limitations are necessary to deal with the complexity of the problem. Among the various computational fluid dynamics methods, accuracy and computational speed are equally important. Therefore, the use of Reynolds-averaged Navier-Stokes (RANS) equations is preferred over more advanced methods, such as detached-eddy simulation (DES) or large-eddy simulation (LES). In terms of hull geometries, only two benchmark hull geometries were used: a modern seagoing containership and a representative inland waterway ship typically operating on the Rhine River.

1.3 Significance of the study

An intended outcome at the theoretical level is the creation of a mathematical manoeuvring model for inland waterway ships in shallow water conditions. This model can be used to train the algorithms for autonomous ships in virtual environments. A second intended outcome, at a practical level, is the creation of methods that reduce the computational time for calculating manoeuvring hydrodynamic forces, especially when the interaction of hull, propeller and rudder is required. Furthermore, a third intended outcome is the development of an alternative method to determine the hydrodynamic manoeuvring coefficients. Such a method could benefit other fields of study dealing with the control of autonomous vehicles. Finally, a mathematical model for manoeuvring in regular waves is proposed as a contribution to the development of a general theory of manoeuvring in realistic environmental conditions.

1.4 State of the art in prediction of manoeuvring in shallow water

Modern mathematical manoeuvring models are based on the contributions of Abkowitz (1964) and Norrbin (1971), which are representative of the two main divisions within mathematical models: formal mathematical models, also known as Abkowitz-type models, and modular models. Both mathematical models use hydrodynamic coefficients that need to be determined. At the beginning, these could only be obtained through captive model tests in specialized hydrodynamic laboratories. Among the important contributions of mathematical models are: the extended multivariable polynomial by Wolff (1981), the four-quadrant modelling by Oltmann and Sharma (1984), and the manoeuvring modelling group, best known as MMG, by Yasukawa and Yoshimura (2015). All these studies were performed for seagoing vessels manoeuvring in deep water.

There are fewer experimental fluid dynamic (EFD) studies of ship manoeuvring in shallow water than in deep water. Their results are used to experimentally study the phenomena and to validate data for numerical methods. Eloot (2006) provided a thorough review of mathematical manoeuvring models and an overview on the experimental fluid dynamics techniques used to obtain the hydrodynamic coefficients in shallow water conditions. Gronarz (1997) carried out systematic experiments to investigate the influence of water depth on the manoeuvring behaviour. Gronarz explicitly showed how each hydrodynamic coefficient varies with the water depth to draft ratio h/T. More recently, experimental captive model test data of a modern inland waterway vessel was published for benchmarking of numerical methods (Mucha, Dettmann, et al. 2019; Mucha, el Moctar, et al. 2017).

The introduction of the viscous flow computational fluid dynamics (CFD) opened up new research possibilities, with the benefit of obtaining hydrodynamic coefficients by numerical calculation. Initially, captive tests were reproduced by CFD using the double-body approach (el Moctar 2001). Later, it became possible to obtain the complete set of hydrodynamic coefficients (Cura-Hochbaum 2006; Toxopeus 2011). More recently, CFD has been applied to the direct simulation of rudder manoeuvres, where the hull, the rudder and the propeller are modelled directly in the numerical domain. Examples of this approach can be found in Carrica et al. (2013), el Moctar, Lantermann, et al. (2014), and Jin et al. (2019). D. Kim et al. (2022) performed free running manoeuvres in shallow water conditions for a containership.

The application of CFD in shallow water has encountered some challenges. Mucha (2017) showed that significant interactions between ship and flow restriction affect the

calculation of the hydrodynamic forces. It has also been shown that shallow water calculations require more computational time than deep water calculations. This increase is mainly due to the reduced under keel clearance and the associated ship's motions. A similar experience was reported by He et al. (2016).

Numerical predictions of the hydrodynamic forces acting on inland waterway vessel in shallow water are scarce. Despite the simplicity of the hull geometry, the propulsion and rudder configuration is more complex than for seagoing vessels. Simplified shallow water manoeuvring problems were studied. Liu (2017) studied in detail the forces of different rudder configurations in open water condition. Lu et al. (2022) added a layer of complexity and simulated the propeller-rudder as a system in open water condition. The authors demonstrated the ability of CFD to capture the hydrodynamic forces of single-propeller/single-rudder and twin-propeller/twin-rudder systems. Furthermore, Kaidi et al. (2018) numerically replicated the rudder captive test in straight ahead condition. The hull, propeller and rudder were considered as a single system, and the inflow interaction between them was captured. Zentari, el Moctar, et al. (2022) carried out resistance and propulsion tests of pusher-barge convoys treated as a single rigid-body and argued that the standard k-ω SST turbulence modelling is not adequate in some shallow water conditions. To date, the CFD-based calculations of the captive tests of a fully appended inland waterway vessel comprising hull, propeller and rudder in shallow water is still lacking.

1.5 State of the art in prediction of manoeuvring in waves

As mentioned above, ship manoeuvring in waves has received a considerable attention since the introduction of the energy efficiency design index. The International Towing Tank Conference (ITTC) formed a special committee on manoeuvring in waves to assess the progress made in this topic. The committee's final report includes a thorough literature review and an overview of the complexities associated with manoeuvring in waves (ITTC 2021). The reports by Tello Ruiz et al. (2012) and Skejic (2013) provide an additional perspective on the development of manoeuvring in waves and highlight the difficulties.

Experimental fluid dynamics (EFD) has been at the forefront of research. A pioneering paper by Hirano et al. (1980) showed the early desire to study this complex phenomenon. The addition of regular waves in the manoeuvring introduces three additional parameters: wave height, wave period and propagation direction. Mapping all possible realistic combinations of these three parameters is a tedious and laborious task. Nevertheless, EFD provided insight into some relevant parameter combinations. The advantage of EFD is that the ship models are self-propelled, i.e., the models are equipped with propeller and

rudder, so that all interactions and complex flows are implicitly taken into account. The manoeuvring of the ship model in waves follows a procedure similar to manoeuvring in calm water. First, the model sails straight ahead at a constant speed, and then the rudder is deflected, keeping the wave parameters constant at all times. Turning circle and zig-zag manoeuvres were usually chosen for testing.

Yasukawa (2006) performed turning circle manoeuvres with the S-175 containership model. Model tests were carried out in regular waves for wave lengths between $0.5L$ and $1.2L$ (0.5, 0.7, 1.0, 1.2) and a target wave height of $H = 0.02L$ in head and beam waves. The results in head waves showed that the smaller the wave length, the greater the drift of the ship's trajectory. Rudder deflection to port or starboard produces a quasi-symmetrical behaviour. The results in beam waves showed a different pattern. When sailing in a straight line, the waves propagate from starboard to port side. Therefore, when turning to starboard, the ship is sailing against the waves, which means that the drift forces of the ship are opposite to the ship's sailing direction. In this condition, the ship turns faster than when it starts the manoeuvre to port. Later, Yasukawa (2008) presented model test results of zig-zag and crash astern manoeuvres in regular waves of the same containership and under the same wave conditions. The two 10°/10° and 20°/20° zig-zag manoeuvres were performed. The results in head waves showed that the smaller the wave length, the faster the ship model reaches the test heading angle (yaw angle $\psi = 10°, 20°$). The results in beam waves showed that, for the 10°/10° zig-zag case, the ship model has difficulties to make the second turn for the wave length of $0.5L$.

Sprenger et al. (2017) presented turning circle and zig-zag manoeuvres in waves for the Duisburg test case (DTC) containership at the low speed of $Fn = 0.052$. For the turning circle manoeuvre, four parameters were varied, namely, the initial heading, the rudder direction, the wave period and the wave height. For the zig-zag manoeuvre, two parameters were varied, namely, the wave period and the time of rudder execution relative to the wave crest/trough. The results of the turning circle manoeuvre showed that the DTC containership drifts obliquely to the direction of wave propagation with a similar pattern as that of the S-175 ship of Yasukawa (2006). It was also found that the timing of the rudder deflection has a negligible effect on the ship's trajectories. Similar findings were presented by D. J. Kim et al. (2019). Sanada et al. (2019) documented that the presentation of manoeuvring in waves in terms of mean advance and tactical diameter is not appropriate, and they recommended a better definition for the analysis of manoeuvring in waves.

The use of RANS equations to calculate hydrodynamic forces in the fields of seakeeping and manoeuvring is well documented, and satisfactory results have been obtained. For

instance, Sigmund and el Moctar (2018) analysed the seakeeping behaviour of four ships for different wavelengths and wave headings. Cura-Hochbaum (2006) proposed the use of RANS to perform captive test simulations to obtain hydrodynamic coefficients.

Wang and Wan (2018) directly simulated turning circle and zig-zag manoeuvres in waves. The overset mesh method was used to discretize the numerical domain and to allow the ship and its appendages to move. A total of 7.13 million control volumes were used with a time step of 0.5 milliseconds, corresponding to 1.5° of propeller rotation per time step. The results showed that the wave effect is visible in the heave, roll and pitch motions. Comparison with experimental data showed that the turning circle manoeuvring parameters, such as advance, transfer and tactical diameter, are within 10% error. This is a good result, considering the complexity of this phenomenon. However, the computing time is enormous. For instance, the turning circle manoeuvre simulation took 1206 hours, which is about 50 days for just one complete turn.

The excessive time required by a RANS based method to analyse manoeuvring in waves motivated the development of practical approaches. In this regard, two main approaches have been proposed to simulate manoeuvring in waves: the two-time scale method and the unified method.

The two-time scale method splits the ship's motion into seakeeping (usually 6DoF) and manoeuvring motions (3DoF or 4DoF, accounting for surge, sway, yaw and roll), which are solved separately. Basically, it solves twice the equations of motion, one for seakeeping and another for manoeuvring. The ship's position, orientation and velocities are taken from the manoeuvring solver and transferred to the seakeeping solver. Meanwhile, second order forces are calculated in the seakeeping solver and transferred to the manoeuvring solver. This data exchange is maintained at each time step during the simulation. The latest development of the two-time scale method uses a seakeeping solver in the time domain, and the solution of the boundary value problem includes the sway and yaw velocities as shown by Zhang et al. (2017).

The unified method treats the seakeeping and the manoeuvring theories within a single set of equations of motion. A conflict in the assumptions used in each independent theory made the merge difficult. For instance, the assumption of "slow motion derivatives" used in manoeuvring to obtain hydrodynamic coefficients has been questioned because, in practice, they are obtained at high frequencies due to the physical limitations of towing tanks (ITTC 2021). The inclusion of memory effects in the modelling of the forces is also discussed. Fluid memory effects have been considered by Letki and Hudson (2005) and Sutulo and Guedes Soares (2006). A common characteristic was the use of the strip theory method to calculate the wave forces. It should be emphasized that the strip theory method

does not account for surge motion although some approximation can be made. However, these approaches did not include the second order wave forces.

Cura-Hochbaum and Uharek (2016) and Fournarakis et al. (2016) presented a method for manoeuvring simulation in waves. The method is based on solving the 4DoF motion equations in a hybrid coordinate system that follows the ship's motions except for roll. In both studies, the authors calculated the hydrodynamic manoeuvring coefficients in calm water using a RANS solver. To compute the mean second wave forces, Cura-Hochbaum and Uharek (2016) used a RANS solver, while Fournarakis et al. (2016) opted for a solver based on potential theory. A common characteristic of these practical methods is the low accuracy (Shigunov et al. 2018). Further work is needed to better assess the forces as well as to revise the assumptions under which the forces are calculated.

In summary, the literature review showed that the theory of manoeuvring in waves is being developed. The experimental studies showed that the drift characteristics in turning circle manoeuvre and the associated drift direction and drift amplitude depend on wave length, wave amplitude and propagation direction. Furthermore, the mean average wave force was shown to be the dominant force during manoeuvres in waves. The addition of the three new parameters wave height, wave period and propagation direction increases the number of tests. RANS based simulations of manoeuvring in waves are limited due to the excessive computational time required for a single case. Practical approaches provided qualitative predictions, but further research is needed to improve the quantitative predictions.

1.6 Overview

The major challenge in predicting manoeuvring under realistic environmental conditions is the accurate calculation of the hydrodynamic forces acting on the hull, propeller, and rudder and their interaction. Two realistic environmental conditions are studied: manoeuvring in shallow water and manoeuvring in waves. For manoeuvring in shallow water, the focus is on inland waterway ships. Due to their complex propulsion system, the flow interaction of hull, propeller and rudder is difficult to simulate, which affects the reliable calculation of forces. For manoeuvring in waves, the focus is on a modern containership sailing in deep water.

The literature review showed that the numerical prediction of the forces of a fully appended inland waterway ship has not yet been achieved, but is necessary for the development of autonomous ships and for a better understanding of the shallow water effect on ship manoeuvring. For manoeuvring in waves, the literature review highlighted the

complexity of the problem and the need to explore new ways to improve the accuracy of the fast methods.

This thesis consists of five further chapters. Chapters 2 and 3 present the fundamental state-of-the-art theory and the numerical methods used for the research. Chapter 2 presents the fundamental equations of ship dynamics and discusses the available mathematical models. Chapter 3 briefly describes the numerical methods used to calculate the hydrodynamic forces.

Chapters 4 and 5 present the main contributions of the thesis. Chapter 4 presents research in the field of ship manoeuvring in shallow water. A mathematical model for manoeuvring in shallow water is proposed and efficient numerical techniques are presented to calculate the manoeuvring hydrodynamic coefficients. Validation of forces and ship trajectories are provided. Chapter 5 presents a mathematical model for manoeuvring in regular waves. In contrast to previous studies, the equations of motion of the ship are solved in the inertial coordinate system. Validation of the trajectories of turning circle manoeuvres in waves is provided.

Chapter 6 provides a general discussion of the research results. It also provides a reflective evaluation of the study from which the final conclusions are drawn. Finally, possible topics for further research are suggested.

2 Ship dynamics and mathematical manoeuvring models

Considering a ship as a rigid body, six principle motions are possible when sailing on the open sea. The source of the forces causing the motion may be environmental, such as waves, wind, or current, in which case the motion is defined as involuntary. Or the motion may be a consequence of the ship changing its course—voluntary motion—by means of forces produced by the control surfaces. A third possible type of motion, called semi-voluntary, could occur as a side effect of a voluntary motion, for example the rolling of a ship during a turning circle manoeuvre. The characteristics of these types of motion have been embodied in the division of ship dynamics into two fields: seakeeping and manoeuvring. Seakeeping studies the involuntary motion caused by wave forces and manoeuvring studies the voluntary motion caused by the action of the control surfaces. This division of ship dynamics was made in response to the need to reduce the complexity of the general ship motion problem.

The fields of seakeeping and manoeuvring have developed independently and the conventions for describing ship motions are specific to each field. However, the separate studies made in each field have contributed to a better understanding of the nature of the forces involved in each field. The purpose of the following chapter is to obtain the general equations of motion of a ship, with particular emphasis on the nonlinear coupling terms that link all the degrees of freedom.

2.1 Reference frame

Two coordinate systems are used to describe the motions of the ship. The earthbound inertial coordinate system ($O\xi\eta\zeta$) used to measure the ship's position and later to describe the wave propagation. The body-fixed coordinate system ($oxyz$), describes the ship's kinematic quantities, the geometry of the hull, and the inertial properties of the ship. Its origin 'o' could be located in any part of the ship, its x-axis pointing forward, its y-axis

to port, and its z-axis upward. Figure 2.1 shows the coordinate systems and Table 2.1 describes these coordinate systems.

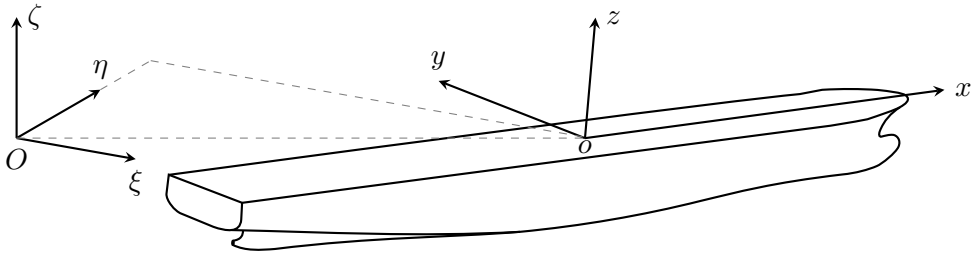

Figure 2.1: Coordinate systems

Table 2.1: Description of coordinate systems

Symbol	Name	Description	Type
$(O\xi\eta\zeta)$	earth-fixed	Used to track the ship's positions and define wave propagation	Inertial
$(oxyz)$	body-fixed	Used to define the ship kinematics, geometry and moment of inertia	Non inertial

2.1.1 Relation between coordinate systems

For a given point, a unique relation between the coordinate systems exists. For instance, a point P can be expressed as $\vec{x}_p = (x_p, y_p, z_p)^\intercal$ in the body-fixed coordinate system, or as $\vec{\xi}_p = (\xi_p, \eta_p, \zeta_p)^\intercal$ in the inertial coordinate system, as shown in Figure 2.2. These two representations of the point P are equivalent.

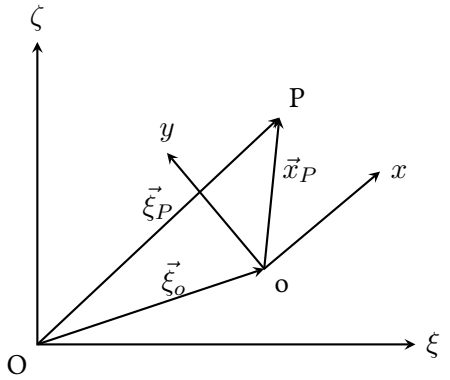

Figure 2.2: Relation between coordinate systems. For the same point two equivalent representations are possible, one in $(O\xi\eta\zeta)$ and one in $(oxyz)$

In Figure 2.2, $\vec{\xi}_o$ represents the origin of the body-fixed coordinate system expressed in the inertial coordinate system. The vector $\vec{\xi}_p$ can be expressed as a sum of vectors $\vec{\xi}_o$ and $\vec{x}_p$. Before making the sum, the vector $\vec{x}_p$ must be transformed to the inertial coordinate system. This can be done as follows:

$$\vec{\xi}_p = \vec{\xi}_o + \mathbf{T}(\varphi, \theta, \psi)\vec{x}_p \tag{2.1}$$

$$\begin{bmatrix} \xi_p \\ \eta_p \\ \zeta_p \end{bmatrix} = \begin{bmatrix} \xi_o \\ \eta_o \\ \zeta_o \end{bmatrix} + \mathbf{T}(\varphi, \theta, \psi) \begin{bmatrix} x_p \\ y_p \\ z_p \end{bmatrix} \tag{2.2}$$

Where $\mathbf{T}(\varphi, \theta, \psi)$ is called a transformation matrix and is a function of three rotation angles (Euler angles): roll angle φ, pitch angle θ, and yaw angle ψ. This matrix transforms the unit vectors of vector $\vec{x}_p$ into the unit vector of the $\vec{\xi}_o$. Therefore, equation (2.2) converts any position vector expressed in the body-fixed coordinate system into the inertial coordinate system ($\vec{x}_p \rightarrow \vec{\xi}_p$).

2.1.2 Transformation matrix

There are several methods for performing a transformation between two orthogonal coordinate systems (quaternions, Euler angles, directional cosines). In marine dynamics, Euler angles are commonly used, following the Tait-Bryans "ξ-η-ζ" rotation convention.

To obtain the transformation matrix $\mathbf{T}(\varphi, \theta, \psi)$, a sequence of rotations from the inertial frame to the body-fixed frame must be performed according to the sequence shown in Figure 2.3. Where $(ox_1y_1z_1)$ and $(ox_2y_2z_2)$ are intermediate auxiliary coordinate systems. The sequence order from the inertial to the body-fixed coordinate system is defined as follows: $\psi \rightarrow \theta \rightarrow \varphi$.

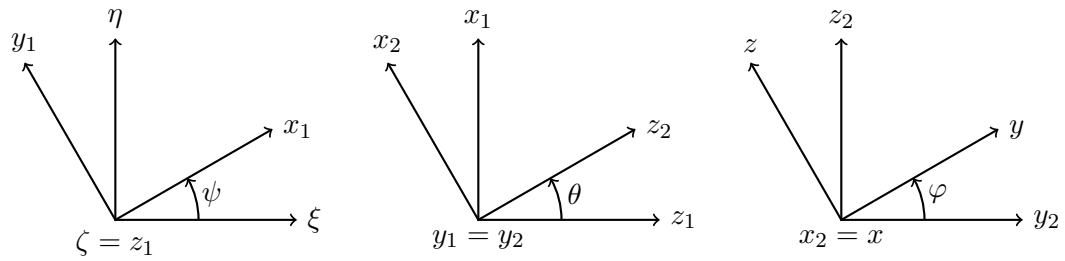

Figure 2.3: Sequence of rotations from $(O\xi\eta\zeta)$ to $(oxyz)$

The first rotation in the sequence is yaw. The transformation matrix $\mathbf{S}_\psi$ relates the newly rotated coordinate system $(ox_1y_1z_1)$ and the inertial coordinate system $(O\xi\eta\zeta)$. The relation between the two coordinate systems reads:

$$\begin{bmatrix}\xi\\ \eta\\ \zeta\end{bmatrix} = \begin{bmatrix}\cos\psi & -\sin\psi & 0\\ \sin\psi & \cos\psi & 0\\ 0 & 0 & 1\end{bmatrix}\begin{bmatrix}x_1\\ y_1\\ z_1\end{bmatrix} \tag{2.3}$$

The second rotation is pitch. The transformation matrix $\mathbf{S}_\theta$, which relates the auxiliary coordinate systems $(ox_1y_1z_1)$ and $(ox_2y_2z_2)$ reads:

$$\begin{bmatrix}x_1\\ y_1\\ z_1\end{bmatrix} = \begin{bmatrix}\cos\theta & 0 & \sin\theta\\ 0 & 1 & 0\\ -\sin\theta & 0 & \cos\theta\end{bmatrix}\begin{bmatrix}x_2\\ y_2\\ z_2\end{bmatrix} \tag{2.4}$$

The third rotation is the roll. After this rotation, the coordinate system has landed in the body-fixed coordinate system. The transformation matrix $\mathbf{S}_\varphi$, which relates the auxiliary coordinate system $(ox_2y_2z_2)$ to the body-fixed coordinate system reads:

$$\begin{bmatrix}x_2\\ y_2\\ z_2\end{bmatrix} = \begin{bmatrix}1 & 0 & 0\\ 0 & \cos\varphi & -\sin\varphi\\ 0 & \sin\varphi & \cos\varphi\end{bmatrix}\begin{bmatrix}x\\ y\\ z\end{bmatrix} \tag{2.5}$$

Therefore the transformation matrix $\mathbf{T}(\varphi,\theta,\psi)$ that relates the inertial and body-fixed coordinate systems can be obtained by multiplying the three above rotations in strict order.

$$\begin{aligned}\mathbf{T}(\varphi,\theta,\psi) &= \mathbf{S}_\psi\cdot\mathbf{S}_\theta\cdot\mathbf{S}_\varphi\\ &= \begin{bmatrix}\cos\psi & -\sin\psi & 0\\ \sin\psi & \cos\psi & 0\\ 0 & 0 & 1\end{bmatrix}\begin{bmatrix}\cos\theta & 0 & \sin\theta\\ 0 & 1 & 0\\ -\sin\theta & 0 & \cos\theta\end{bmatrix}\begin{bmatrix}1 & 0 & 0\\ 0 & \cos\varphi & -\sin\varphi\\ 0 & \sin\varphi & \cos\varphi\end{bmatrix}\end{aligned}$$

$$\mathbf{T} = \begin{bmatrix}\cos\psi\cos\theta & \cos\psi\sin\theta\sin\varphi-\sin\psi\cos\varphi & \cos\psi\sin\theta\cos\varphi+\sin\psi\sin\varphi\\ \sin\psi\cos\theta & \sin\psi\sin\theta\sin\varphi+\cos\psi\cos\varphi & \sin\psi\sin\theta\cos\varphi-\cos\psi\sin\varphi\\ -\sin\theta & \cos\theta\sin\varphi & \cos\theta\cos\varphi\end{bmatrix} \tag{2.6}$$

Notice that the matrix $\mathbf{T}$ is orthogonal i.e. that $\mathbf{T}^{-1} = \mathbf{T}^{\intercal}$. Thus, the inverse of the transformation matrix is made by simply transposing the matrix. Therefore, transformation from inertial coordinate system to body-fixed coordinate system can be done easily.

2.2 Kinematics

A ship moving in three-dimensional space has 6 degrees of freedom (DoF), three translations that are measured by the position of the body-fixed origin ($\vec{\xi}_o$) and three rotations that are measured by the Euler angles $\vec{\Theta} = (\varphi, \theta, \psi)^{\intercal}$. These motions have special names in naval architecture and are defined in the body-fixed coordinate system. Table 2.2 shows the definitions and symbols used to describe the ship motions.

Table 2.2: Definition of ship motions

DoF	name	description	velocities
1	surge	translation in the x-axis direction	u
2	sway	translation in the y-axis direction	v
3	heave	translation in the z-axis direction	w
4	roll	rotation around x-axis	p
5	pitch	rotation around y-axis	q
6	yaw	rotation around z-axis	r

2.2.1 Relation between velocities

The translation velocity or simple velocity is a free vector that can be expressed in any coordinate system. Here, the ship's velocity is represented in the body-fixed coordinate system by $\vec{v}_o = (u, v, w)^{\intercal}$ and in the inertial coordinate system by $\dot{\vec{\xi}}_o = (\dot{\xi}, \dot{\eta}, \dot{\zeta})^{\intercal}$. Both are related by the transformation matrix $\mathbf{T}(\varphi, \theta, \psi)$.

$$\begin{bmatrix} \dot{\xi} \\ \dot{\eta} \\ \dot{\zeta} \end{bmatrix} = \mathbf{T}(\varphi, \theta, \psi) \begin{bmatrix} u \\ v \\ w \end{bmatrix} \tag{2.7}$$

2.2.2 Relation between angular velocities

The body angular velocity is also a free vector and can therefore be represented in any coordinate system. The angular velocity is represented in the body-fixed coordinates system by $\vec{\omega} = (p, q, r)^{\intercal}$ and in the inertial coordinate system by $\vec{\Omega} = (\omega_x, \omega_y, \omega_z)^{\intercal}$. Analogous

to translation velocities, the angular velocities are related by the transformation matrix $\mathbf{T}(\varphi, \theta, \psi)$.

$$\vec{\Omega} = \mathbf{T}(\varphi, \theta, \psi)\vec{\omega} \tag{2.8}$$
$$\begin{bmatrix} \omega_x \\ \omega_y \\ \omega_z \end{bmatrix} = \mathbf{T}(\varphi, \theta, \psi) \begin{bmatrix} p \\ q \\ r \end{bmatrix}$$

However, in order to describe the rotations, it is more advantageous to relate the rate of change of the Euler angles $\dot{\vec{\Theta}} = (\dot{\varphi}, \dot{\theta}, \dot{\psi})^\intercal$ to the body angular velocities $\vec{\omega}$ or $\vec{\Omega}$. It is therefore possible to assume that such a relation is given by a transformation matrix $\mathbf{S}(\varphi, \theta, \psi)$ and $\mathbf{R}(\varphi, \theta, \psi)$ which satisfies the following conditions:

$$\vec{\omega} = \mathbf{S}(\varphi, \theta, \psi)\dot{\vec{\Theta}} \tag{2.9}$$
$$\vec{\Omega} = \mathbf{R}(\varphi, \theta, \psi)\dot{\vec{\Theta}} \tag{2.10}$$

The above relationship should not be interpreted as a coordinate transformation. It simply expresses how the body-fixed coordinate system is oriented with respect to the inertial frame. Furthermore, it can be shown that the matrices **S** and **R** do not satisfy the orthogonal coordinate transformation property i.e. $\mathbf{S}^{-1} \neq \mathbf{S}^\intercal$. The matrix $\mathbf{S}(\varphi, \theta, \psi)$ can be obtained following the Tait-Bryans ξ-η-ζ sequence rotation.

$$\begin{bmatrix} p \\ q \\ r \end{bmatrix} = \begin{bmatrix} \dot{\varphi} \\ 0 \\ 0 \end{bmatrix} + \mathbf{S}_\varphi \begin{bmatrix} 0 \\ \dot{\theta} \\ 0 \end{bmatrix} + \mathbf{S}_\varphi \mathbf{S}_\theta \begin{bmatrix} 0 \\ 0 \\ \dot{\psi} \end{bmatrix} \tag{2.11}$$

$$\begin{bmatrix} p \\ q \\ r \end{bmatrix} = \begin{bmatrix} 1 & 0 & -\sin\theta \\ 0 & \cos\varphi & \cos\theta\sin\varphi \\ 0 & -\sin\varphi & \cos\theta\cos\varphi \end{bmatrix} \begin{bmatrix} \dot{\varphi} \\ \dot{\theta} \\ \dot{\psi} \end{bmatrix} \tag{2.12}$$

Therefore, by comparing the equations (2.9) and (2.12) gives the expression for the matrix $\mathbf{S}(\varphi, \theta, \psi)$. Furthermore, this matrix does not depend on the yaw angle ψ.

$$\mathbf{S}(\varphi, \theta, \psi) = \begin{bmatrix} 1 & 0 & -\sin\theta \\ 0 & \cos\varphi & \cos\theta\sin\varphi \\ 0 & -\sin\varphi & \cos\theta\cos\varphi \end{bmatrix} \tag{2.13}$$

The matrix $\mathbf{R}(\varphi, \theta, \psi)$ can be obtained from equation (2.8), from which the relation $\mathbf{R} = \mathbf{TS}$ stands and the transformation matrix $\mathbf{R}$ is defined.

$$\vec{\Omega} = \mathbf{T}\vec{\omega} = \mathbf{TS}\dot{\vec{\Theta}} \quad \rightarrow \quad \mathbf{R} = \mathbf{TS}$$

$$\mathbf{R}(\varphi, \theta, \psi) = \begin{bmatrix} \cos\psi\cos\theta & -\sin\psi & 0 \\ \sin\psi\cos\theta & \cos\psi & 0 \\ -\sin\theta & 0 & 1 \end{bmatrix} \tag{2.14}$$

If the rate of change of the Euler angles is needed, then the inverse matrix $\mathbf{S}^{-1}(\varphi, \theta, \psi)$ can be used.

$$\mathbf{S}^{-1}(\varphi, \theta, \psi) = \begin{bmatrix} 1 & \sin\varphi\tan\theta & \cos\varphi\tan\theta \\ 0 & \cos\varphi & -\sin\varphi \\ 0 & \sin\varphi/\cos\theta & \cos\varphi/\cos\theta \end{bmatrix} \tag{2.15}$$

Notice that $\mathbf{S}^{-1}(\varphi, \theta, \psi)$ is singular for a pitch angle $\theta = \pm 90°$. However, no ship experiences such large pitch motion.

2.3 Rigid body dynamics

Ship dynamics are described by the equations of motion of rigid bodies, first introduced by Euler. These equations, known as the Newton-Euler equations, are valid only in an inertial reference frame and are expressed with respect to the centre of gravity (COG). The general forms can be written as:

$$\vec{F} = \frac{d}{dt}(m\vec{U}_G) = m\dot{\vec{U}}_G \tag{2.16}$$

$$\vec{M}_G = \frac{d}{dt}(\vec{H}_G) = \dot{\vec{H}}_G \tag{2.17}$$

where

$\vec{F}$	:	Total external force
$\vec{M}_G$	:	Total moment of external forces about the COG
m	:	Mass of rigid body
$\vec{U}_G$	:	Velocity of the COG
$m\vec{U}_G$	:	Linear momentum
$\vec{H}_G$	:	Angular momentum about the COG

All the terms in the Newton-Euler equations must be expressed in the inertial coordinate system. However, sometimes it is easier to calculate forces in the body-fixed co-

ordinate system and transform them later. All moments are about the COG, but can be calculated at another convenient point (amidship) and then transferred to the COG.

2.3.1 Position and motions of the centre of gravity

For general simulation purpose it is convenient to express the Newton-Euler equations on the origin of the body-fixed coordinate system, which not always coincide with the centre of gravity. Therefore, the Newton-Euler equations will be expressed as a function of the origin of the body-fixed coordinate system. The vector $\vec{r}_G$ define the position of the centre of gravity in the body-fixed coordinate system. Thus, following equation (2.1) the position of the centre of gravity in the inertial coordinate system reads

$$\vec{\xi}_G = \vec{\xi}_o + \mathbf{T}\vec{r}_G \tag{2.18}$$

The corresponding velocity and acceleration are obtained by direct time derivation in the earth-fixed frame. For instance, the velocity reads

$$\vec{U}_G = \frac{d}{dt}\vec{\xi}_G = \frac{d}{dt}\vec{\xi}_o + \frac{d}{dt}\mathbf{T}\vec{r}_G \tag{2.19}$$

$$\dot{\vec{\xi}}_G = \dot{\vec{\xi}}_o + \dot{\mathbf{T}}\vec{r}_G + \mathbf{T}\dot{\vec{r}}_G \tag{2.20}$$

$$\dot{\vec{\xi}}_G = \dot{\vec{\xi}}_o + \mathbf{T}(\vec{\omega} \times \vec{r}_G) \tag{2.21}$$

In this equation the term $\dot{\vec{\xi}}_G$ is the velocity of the ship's centre of gravity and $\dot{\vec{\xi}}_o$ is the velocity of the origin of the body-fixed coordinate system. Both expressed in the inertial coordinate system. $\vec{\omega}$ is the angular velocity expressed in the body-fixed coordinate system. Note that the position of the centre of gravity is constant on the body-fixed coordinate system (rigid body assumption $\dot{\vec{r}}_G = 0$).

The acceleration of the centre of gravity can be obtained as the time derivative of the velocity.

$$\dot{\vec{U}}_G = \frac{d}{dt}\dot{\vec{\xi}}_o + \frac{d}{dt}\mathbf{T}(\vec{\omega} \times \vec{r}_G) \tag{2.22}$$

$$\dot{\vec{U}}_G = \ddot{\vec{\xi}}_G = \ddot{\vec{\xi}}_o + \mathbf{T}\big[\dot{\vec{\omega}} \times \vec{r}_G + \vec{\omega} \times (\vec{\omega} \times \vec{r}_G)\big] \tag{2.23}$$

2.3.2 Angular momentum at centre of gravity

The angular momentum $\vec{H}_G$ in equation (2.17) can be described better in the body-fixed coordinate system.

$$\vec{H}_G = \mathbf{T}\vec{h}_G \tag{2.24}$$

$$\vec{h}_G = \vec{h}_o - m\vec{r}_G \times (\vec{\omega} \times \vec{r}_G) \tag{2.25}$$

where $\vec{h}_G$ is the angular momentum about the COG and $\vec{h}_o$ about the origin of the body-fixed coordinate system. This angular momentum is calculated as:

$$\vec{h}_o = \begin{bmatrix} I_{xx} & -I_{xy} & -I_{xz} \\ -I_{yx} & I_{yy} & -I_{yz} \\ -I_{zx} & -I_{zy} & I_{zz} \end{bmatrix} \begin{bmatrix} p \\ q \\ r \end{bmatrix} = \mathbf{I}_o\vec{\omega} \tag{2.26}$$

where $\mathbf{I}_o$ is the moment of inertia tensor calculated with respect to the origin of the body-fixed coordinate system. Note that $\mathbf{I}_o$ is constant in the body-fixed coordinate system and if all the masses m_i belonging to the ship and its load are fixed to the ship, the moment of inertia can be calculated as follows:

$$\mathbf{I}_o = \begin{bmatrix} \sum_i m_i(y_i^2 + z_i^2) & -\sum_i m_i x_i y_i & -\sum_i m_i x_i z_i \\ -\sum_i m_i y_i x_i & \sum_i m_i(x_i^2 + z_i^2) & -\sum_i m_i y_i z_i \\ -\sum_i m_i z_i x_i & -\sum_i m_i z_i y_i & \sum_i m_i(x_i^2 + y_i^2) \end{bmatrix} \tag{2.27}$$

The time derivative of the angular momentum is needed in equation (2.17). This, is computed as:

$$\frac{d}{dt}(\vec{H}_G) = \frac{d}{dt}(\mathbf{T}\vec{h}_G) = \frac{d}{dt}\mathbf{T}\Big[\vec{h}_o - m\vec{r}_G \times (\vec{\omega} \times \vec{r}_G)\Big] \tag{2.28}$$

$$= \frac{d}{dt}(\mathbf{T}\vec{h}_o) - m\frac{d}{dt}\mathbf{T}\big[\vec{r}_G \times (\vec{\omega} \times \vec{r}_G)\big] \tag{2.29}$$

$$= \mathbf{T}(\dot{\vec{h}}_o + \vec{\omega} \times \vec{h}_o) - m\mathbf{T}\big[\vec{r}_G \times (\dot{\vec{\omega}} \times \vec{r}_G)\big] \tag{2.30}$$

2.3.3 Equation of motion with respect to a generic point

The equations in (2.16) and (2.17) are written in relation to the ship's centre of gravity. However, it is more convenient to relate the equations to the origin of the body-fixed coordinate system. This allows for example, a direct comparison with experimental measurements. In experiments it is easier to measure forces and motions at amidship than at

the COG. Transferring the force and moment from the COG to the origin of the body-fixed coordinate system gives the equations:

$$m\frac{d}{dt}(\vec{U}_G) = \vec{F} \tag{2.31}$$

$$\frac{d}{dt}(\vec{H}_G) = \vec{M}_o - \mathbf{T}\vec{r}_G \times \vec{F} \tag{2.32}$$

Replacing equation (2.23) into equation (2.31) gives:

$$m\Big[\ddot{\vec{\xi}}_o + \mathbf{T}(\dot{\vec{\omega}} \times \vec{r}_G) + \mathbf{T}\big[\vec{\omega} \times (\vec{\omega} \times \vec{r}_G)\big]\Big] = \vec{F} \tag{2.33}$$

Similarly, replacing equations (2.30) and (2.33) into equation (2.32) the moment equation becomes:

$$\mathbf{T}(\dot{\vec{h}}_o+\vec{\omega}\times\vec{h}_o)-m\mathbf{T}\big[\vec{r}_G\times(\dot{\vec{\omega}}\times\vec{r}_G)\big] = \vec{M}_o-m\mathbf{T}\vec{r}_G\times\Big[\ddot{\vec{\xi}}_o + \mathbf{T}(\dot{\vec{\omega}} \times \vec{r}_G) + \mathbf{T}\big[\vec{\omega} \times (\vec{\omega} \times \vec{r}_G)\big]\Big] \tag{2.34}$$

performing operations on the right-hand side of the above equation, it reduces to:

$$\mathbf{T}(\dot{\vec{h}}_o+\vec{\omega}\times\vec{h}_o)-m\mathbf{T}\big[\vec{r}_G\times(\dot{\vec{\omega}}\times\vec{r}_G)\big] = \vec{M}_o-m\mathbf{T}\vec{r}_G\times\ddot{\vec{\xi}}_o-m\mathbf{T}\big[\vec{r}_G\times(\dot{\vec{\omega}}\times\vec{r}_G)\big] \tag{2.35}$$

where the second term on the left-hand side and the last term on the right hand side cancel each other out and the equation is simplified to:

$$\mathbf{T}(\dot{\vec{h}}_o + \vec{\omega} \times \vec{h}_o) + m\mathbf{T}\vec{r}_G \times \ddot{\vec{\xi}}_o = \vec{M}_o \tag{2.36}$$

Therefore, the ship dynamic equation generalized to a point that coincides with the origin of the body-fixed coordinate system reads

$$m\ddot{\vec{\xi}}_o + m\mathbf{T}(\dot{\vec{\omega}} \times \vec{r}_G) + m\mathbf{T}\big[\vec{\omega} \times (\vec{\omega} \times \vec{r}_G)\big] = \vec{F} \tag{2.37}$$

$$\mathbf{T}\dot{\vec{h}}_o + \mathbf{T}(\vec{\omega} \times \vec{h}_o) + m\mathbf{T}\vec{r}_G \times \ddot{\vec{\xi}}_o = \vec{M}_o \tag{2.38}$$

2.3.4 Equations of motion in body-fixed coordinate system

The equations of motion can be expressed entirely using only vectors in the body-fixed coordinate system. This form of representation is used extensively in the analysis of manoeuvring in calm water. Thus, equations (2.37) and (2.38) will be transformed from

the earth coordinate system into the body-fixed one. For that, the acceleration of the origin of the body-fixed coordinate system is expressed as:

$$\ddot{\vec{\xi}}_o = \frac{d}{dt}(\vec{U}_o) = \mathbf{T}(\dot{\vec{v}}_o + \vec{\omega} \times \vec{v}_o) \tag{2.39}$$

where $\vec{v}_o = (u, v, w)^\intercal$ is the velocity and $\dot{\vec{v}}_o = (\dot{u}, \dot{v}, \dot{w})^\intercal$ the acceleration of the origin of the body-fixed coordinate system, both expressed in the body-fixed frame. Replacing the above values into the equations (2.37) and (2.38) the equations yield

$$m\mathbf{T}(\dot{\vec{v}}_o + \vec{\omega} \times \vec{v}_o) + m\mathbf{T}(\dot{\vec{\omega}} \times \vec{r}_G) + m\mathbf{T}\big[\vec{\omega} \times (\vec{\omega} \times \vec{r}_G)\big] = \vec{F} \tag{2.40}$$

$$\mathbf{T}\dot{\vec{h}}_o + \mathbf{T}(\vec{\omega} \times \vec{h}_o) + m\mathbf{T}\big[\vec{r}_G \times (\dot{\vec{v}}_o + \vec{\omega} \times \vec{v}_o)\big] = \vec{M}_o \tag{2.41}$$

Multiplying both equations by the inverse transformation matrix $\mathbf{T}^{-1}$, the equation becomes

$$m(\dot{\vec{v}}_o + \vec{\omega} \times \vec{v}_o) + m\dot{\vec{\omega}} \times \vec{r}_G + m\vec{\omega} \times (\vec{\omega} \times \vec{r}_G) = \vec{f} \tag{2.42}$$

$$\dot{\vec{h}}_o + \vec{\omega} \times \vec{h}_o + m\vec{r}_G \times (\dot{\vec{v}}_o + \vec{\omega} \times \vec{v}_o) = \vec{m}_o \tag{2.43}$$

where $\vec{f} = \mathbf{T}^{-1}\vec{F}$ and $\vec{m}_o = \mathbf{T}^{-1}\vec{M}_o$ are respectively the force and moment expressed in the body-fixed coordinate system. Regrouping terms the equation reads

$$m(\dot{\vec{v}}_o + \dot{\vec{\omega}} \times \vec{r}_G) + m\vec{\omega} \times \vec{v}_o + m\vec{\omega} \times (\vec{\omega} \times \vec{r}_G) = \vec{f} \tag{2.44}$$

$$(\dot{\vec{h}}_o + m\vec{r}_G \times \dot{\vec{v}}_o) + \vec{\omega} \times \vec{h}_o + m\vec{r}_G \times (\vec{\omega} \times \vec{v}_o) = \vec{m}_o \tag{2.45}$$

The above equations represent the rigid body equations of motion expressed in the body-fixed coordinate system. These equations are also found in classical mechanics of rigid bodies (Lurie 2002). Equation (2.44) relates to the total external force $\vec{f}$ acting on the body with the translatory acceleration $\dot{\vec{v}}_o$, angular acceleration $\dot{\vec{\omega}}$, translatory velocity $\vec{v}_o$, angular velocity $\vec{\omega}$, the position of the centre of gravity $\vec{r}_G$ and the body mass m. Similarly, equation (2.45) relates to the total external moment $\vec{m}_o$ acting on the body with the angular momentum $\dot{\vec{h}}_o$ and with the variables already described. Note that the sub-index 'o' indicates that the quantity is measured at the origin of the body-fixed coordinate system.

It is common to present the equations of motion in a decoupled form. Using vector components $\vec{f} = (X, Y, Z)^\intercal$, $\vec{m}_o = (K, M, N)^\intercal$, $\vec{r}_G = (x_G, y_G, z_G)^\intercal$ and following

vector algebraic analysis and rearrangement of terms of equations (2.44) and (2.45) , the 6DoF rigid body equation of motions reads

$$\begin{aligned}
m[\dot{u} - vr + wq - x_G(q^2 + r^2) + y_G(pq - \dot{r}) + z_G(pr + \dot{q})] &= X \quad (2.46)\\
m[\dot{v} - wp + ur - y_G(r^2 + p^2) + z_G(qr - \dot{p}) + x_G(qp + \dot{r})] &= Y \quad (2.47)\\
m[\dot{w} - uq + vp - z_G(p^2 + q^2) + x_G(rp - \dot{q}) + y_G(rq + \dot{p})] &= Z \quad (2.48)\\
I_{xx}\dot{p} + (I_{zz} - I_{yy})qr - (\dot{r} + pq)I_{xz} + (r^2 - q^2)I_{yz} + (pr - \dot{q})I_{xy} & \\
+m[y_G(\dot{w} - uq + vp) - z_G(\dot{v} - wp + ur)] &= K \quad (2.49)\\
I_{yy}\dot{q} + (I_{xx} - I_{zz})rp - (\dot{p} + qr)I_{xy} + (p^2 - r^2)I_{zx} + (qp - \dot{r})I_{yz} & \\
+m[z_G(\dot{u} - vr + wq) - x_G(\dot{w} - uq + vp)] &= M \quad (2.50)\\
I_{zz}\dot{r} + (I_{yy} - I_{xx})pq - (\dot{q} + rp)I_{yz} + (q^2 - p^2)I_{xy} + (rq - \dot{p})I_{zx} & \\
+m[x_G(\dot{v} - wp + ur) - y_G(\dot{u} - vr + wq)] &= N \quad (2.51)
\end{aligned}$$

2.3.5 Equations of motion in inertial coordinate system

The rigid body equations are expressed in vector form in equations (2.37) and (2.38) , with some vectors expressed in the inertial coordinate system and others in the body-fixed coordinate system. Seakeeping uses the linearized version of these equations expressed in an inertial frame moving straight ahead at the ship's average speed. However, the seakeeping equations are not valid for general curvilinear ship motions. For this reason, the nonlinear equation expressed in the inertial coordinate system is derived here. The main motivation for deriving these equations is their use in manoeuvring in waves, where wave propagation and spatial constraints can be described directly in this reference frame.

1. Momentum equation

The momentum equation was presented in equation (2.37) and is rewritten below. Now the equation should be written in matrix-vector form with terms in the inertial coordinate system only. For this task, the skew symmetric matrix (**Sw**) is used in order to convert the cross vector product into a matrix-vector multiplication (details of the skew symmetric matrix are given in Appendix A.

$$\begin{aligned}
\vec{F} &= m\ddot{\vec{\xi}}_o + m\mathbf{T}(\dot{\vec{\omega}} \times \vec{r}_G) + m\mathbf{T}[\vec{\omega} \times (\vec{\omega} \times \vec{r}_G)]\\
&= m\ddot{\vec{\xi}}_o + m\mathbf{T}\mathbf{S}\mathbf{w}^{\mathsf{T}}(\vec{r}_G)\dot{\vec{\omega}} + m\mathbf{T}\mathbf{S}\mathbf{w}(\vec{\omega})\mathbf{S}\mathbf{w}(\vec{\omega})\vec{r}_G \quad (2.52)\\
&= m\ddot{\vec{\xi}}_o + m\mathbf{T}\Big\{\mathbf{S}\mathbf{w}^{\mathsf{T}}(\vec{r}_G)\dot{\vec{\omega}} + \mathbf{S}\mathbf{w}(\vec{\omega})\mathbf{S}\mathbf{w}(\vec{\omega})\vec{r}_G\Big\} \quad (2.53)
\end{aligned}$$

where

(a) the matrix-vector multiplication $\mathbf{Sw}^{\mathsf{T}}(\vec{r}_G)\dot{\vec{\omega}}$ is

$$\mathbf{Sw}^{\mathsf{T}}(\vec{r}_G)\dot{\vec{\omega}} = \underbrace{\begin{bmatrix} 0 & z_G & -y_G \\ -z_G & 0 & x_G \\ y_G & -x_G & 0 \end{bmatrix}}_{\mathbf{G}_1} \begin{bmatrix} \dot{p} \\ \dot{q} \\ \dot{r} \end{bmatrix} = \mathbf{G}_1\dot{\vec{\omega}} \tag{2.54}$$

(b) the matrix-vector multiplication $\mathbf{Sw}(\vec{\omega})\mathbf{Sw}(\vec{\omega})\vec{r}_G$ is

$$\mathbf{Sw}(\vec{\omega})\mathbf{Sw}(\vec{\omega})\vec{r}_G = \begin{bmatrix} 0 & -r & q \\ r & 0 & -p \\ -q & p & 0 \end{bmatrix} \begin{bmatrix} 0 & -r & q \\ r & 0 & -p \\ -q & p & 0 \end{bmatrix} \begin{bmatrix} x_G \\ y_G \\ z_G \end{bmatrix} \tag{2.55}$$

$$= \begin{bmatrix} -q^2 - r^2 & pq & rp \\ pq & -p^2 - r^2 & rq \\ rp & rq & -p^2 - q^2 \end{bmatrix} \begin{bmatrix} x_G \\ y_G \\ z_G \end{bmatrix} \tag{2.56}$$

$$= \underbrace{\begin{bmatrix} 0 & z_G & y_G \\ z_G & 0 & x_G \\ y_G & x_G & 0 \end{bmatrix}}_{\mathbf{G}_2} \underbrace{\begin{bmatrix} qr \\ rp \\ pq \end{bmatrix}}_{\vec{\omega}_1} - \underbrace{\begin{bmatrix} 0 & x_G & x_G \\ y_G & 0 & y_G \\ z_G & z_G & 0 \end{bmatrix}}_{\mathbf{G}_3} \underbrace{\begin{bmatrix} p^2 \\ q^2 \\ r^2 \end{bmatrix}}_{\vec{\omega}_2} \tag{2.57}$$

$$= \mathbf{G}_2\vec{\omega}_1 - \mathbf{G}_3\vec{\omega}_2 \tag{2.58}$$

Thus, the momentum equation yields

$$\vec{F} = m\ddot{\vec{\xi}}_o + m\mathbf{T}\Big(\mathbf{G}_1\dot{\vec{\omega}} + \mathbf{G}_2\vec{\omega}_1 - \mathbf{G}_3\vec{\omega}_2\Big) \tag{2.59}$$

Where matrices $\mathbf{G}_1$, $\mathbf{G}_2$ and $\mathbf{G}_3$ only depend on the ship centre of gravity.

2. Angular momentum equation

The angular momentum equation was presented in equation (2.38), which is rewritten below. Again, the body acceleration should be expressed in the inertial coordinate system. However, it is more advantageous to express the angular momentum in the body coordinate system. This is done, because the moment of inertia of a given body is constant in relation to the body-fixed coordinate system.

$$\vec{M}_o = \frac{d}{dt}\mathbf{T}\vec{h}_o + m(\mathbf{T}\vec{r}_G) \times \ddot{\vec{\xi}}_o$$

where:

(a) the angular momentum $\vec{h}_o$ in body-fixed coordinate system can be expressed as a multiplication of the inertia tensor $\mathbf{I}_o$ and the body angular velocity $\vec{\omega}$:

$$\vec{h}_o = \begin{bmatrix} I_{xx} & -I_{xy} & -I_{xz} \\ -I_{yx} & I_{yy} & -I_{yz} \\ -I_{zx} & -I_{zy} & I_{zz} \end{bmatrix} \begin{bmatrix} p \\ q \\ r \end{bmatrix} = \mathbf{I}_o \vec{\omega} \tag{2.60}$$

(b) the time derivative of the momentum $\frac{d}{dt}\mathbf{T}\vec{h}_o$ is:

$$\frac{d}{dt}\mathbf{T}\vec{h}_o = \mathbf{T}\Big(\dot{\vec{h}}_o + \vec{\omega} \times \vec{h}_o\Big) \tag{2.61}$$

$$= \mathbf{T}\Big(\mathbf{I}_o\dot{\vec{\omega}} + \vec{\omega} \times (\mathbf{I}_o\vec{\omega})\Big) \tag{2.62}$$

Expressing the vector cross product as a matrix-vector multiplication, the equation reads:

$$\frac{d}{dt}\mathbf{T}\vec{h}_o = \mathbf{T}\Big(\mathbf{I}_o\dot{\vec{\omega}} + \mathbf{Sw}(\vec{\omega})\mathbf{I}_o\vec{\omega}\Big) \tag{2.63}$$

(c) the term $\mathbf{Sw}(\vec{\omega})\mathbf{I}_o\vec{\omega}$ can be written as:

$$\mathbf{Sw}(\vec{\omega})\mathbf{I}_o\vec{\omega} = \begin{bmatrix} 0 & -r & q \\ r & 0 & -p \\ -q & p & 0 \end{bmatrix} \begin{bmatrix} I_{xx} & -I_{xy} & -I_{xz} \\ -I_{yx} & I_{yy} & -I_{yz} \\ -I_{zx} & -I_{zy} & I_{zz} \end{bmatrix} \begin{bmatrix} p \\ q \\ r \end{bmatrix} \tag{2.64}$$

$$= \underbrace{\begin{bmatrix} (I_{zz} - I_{yy}) & I_{yx} & -I_{zx} \\ -I_{xy} & (I_{xx} - I_{zz}) & I_{zy} \\ I_{xz} & -I_{yz} & (I_{yy} - I_{xx}) \end{bmatrix}}_{\mathbf{I}_2} \underbrace{\begin{bmatrix} qr \\ rp \\ pq \end{bmatrix}}_{\vec{\omega}_1}$$

$$+ \underbrace{\begin{bmatrix} 0 & -I_{zy} & I_{yz} \\ I_{zx} & 0 & -I_{xz} \\ -I_{yx} & I_{xy} & 0 \end{bmatrix}}_{\mathbf{I}_1} \underbrace{\begin{bmatrix} p^2 \\ q^2 \\ r^2 \end{bmatrix}}_{\vec{\omega}_2} \tag{2.65}$$

$$= \mathbf{I}_2\vec{\omega}_1 + \mathbf{I}_1\vec{\omega}_2 \tag{2.66}$$

(d) For the term $(\mathbf{T}\vec{r}_G) \times \ddot{\vec{\xi}}_o$: the position of the centre of gravity expressed in the inertial coordinate system is given by $\mathbf{T}\vec{r}_G = (G_\xi, G_\eta, G_\zeta)^\intercal$ and the cross product can be written as:

$$(\mathbf{T}\vec{r}_G) \times \ddot{\vec{\xi}}_o = \mathbf{Sw}(\mathbf{T}\vec{r}_G)\ddot{\vec{\xi}}_o = \underbrace{\begin{bmatrix} 0 & -G_\zeta & G_\eta \\ G_\zeta & 0 & -G_\xi \\ -G_\eta & G_\xi & 0 \end{bmatrix}}_{\mathbf{G}} \begin{bmatrix} \ddot{\xi}_o \\ \ddot{\eta}_o \\ \ddot{\zeta}_o \end{bmatrix} = \mathbf{G}\ddot{\vec{\xi}}_o \tag{2.67}$$

Therefore the angular momentum can be written as

$$\vec{M}_o = \mathbf{T}\Big(\mathbf{I}_o\dot{\vec{\omega}} + \mathbf{I}_2\vec{\omega}_1 + \mathbf{I}_1\vec{\omega}_2\Big) + m\mathbf{G}\ddot{\vec{\xi}}_o \tag{2.68}$$

where the matrices $\mathbf{I}_o$, $\mathbf{I}_1$ and $\mathbf{I}_2$ depend only on the components of the inertial tensor. Matrix $\mathbf{G}$ depends on the position of the centre of gravity and the Euler angles. Therefore, the translation and angular momentum equations are:

$$\vec{F} = m\ddot{\vec{\xi}}_o + m\mathbf{T}\Big(\mathbf{G}_1\dot{\vec{\omega}} + \mathbf{G}_2\vec{\omega}_1 - \mathbf{G}_3\vec{\omega}_2\Big) \tag{2.69}$$

$$\vec{M}_o = m\mathbf{G}\ddot{\vec{\xi}}_o + \mathbf{T}\Big(\mathbf{I}_o\dot{\vec{\omega}} + \mathbf{I}_2\vec{\omega}_1 + \mathbf{I}_1\vec{\omega}_2\Big) \tag{2.70}$$

3. Equations with generalized variables

The equations of motion of a rigid body can be solved using six generalized variables $(\vec{\xi}_o, \vec{\Theta})^\intercal = (\xi_o, \eta_o, \zeta_o, \psi, \theta, \varphi)^\intercal$. The first three variables correspond to the ship's position and the last three to its orientation. The angular acceleration $\vec{\omega} = (\dot{p}, \dot{q}, \dot{r})^\intercal$ on equations (2.69) and (2.70) is replaced by the generalised velocity $\dot{\vec{\Theta}} = (\dot{\psi}, \dot{\theta}, \dot{\varphi})^\intercal$. This can be done using equation (2.12) which states

$$\vec{\omega} = \mathbf{S}^{-1}(\varphi, \theta, \psi)\dot{\vec{\Theta}}$$

$$\begin{bmatrix} p \\ q \\ r \end{bmatrix} = \begin{bmatrix} 1 & 0 & -\sin\theta \\ 0 & \cos\varphi & \cos\theta\sin\varphi \\ 0 & -\sin\varphi & \cos\theta\cos\varphi \end{bmatrix} \begin{bmatrix} \dot{\varphi} \\ \dot{\theta} \\ \dot{\psi} \end{bmatrix} = \begin{bmatrix} \dot{\varphi} - \dot{\psi}\sin\theta \\ \dot{\theta}\cos\varphi + \dot{\psi}\cos\theta\sin\varphi \\ -\dot{\theta}\sin\varphi + \dot{\psi}\cos\theta\cos\varphi \end{bmatrix} \tag{2.71}$$

making a time derivative of the above expression

$$\begin{bmatrix}\dot{p}\\ \dot{q}\\ \dot{r}\end{bmatrix} = \begin{bmatrix}\ddot{\varphi} - \ddot{\psi}\sin\theta - \dot{\psi}\dot{\theta}\cos\theta \\ \ddot{\theta}\cos\varphi - \dot{\theta}\dot{\varphi}\sin\varphi + \ddot{\psi}\cos\theta\sin\varphi - \dot{\psi}\dot{\theta}\sin\theta\sin\varphi + \dot{\psi}\dot{\varphi}\cos\theta\cos\varphi \\ -\ddot{\theta}\sin\varphi - \dot{\theta}\dot{\varphi}\cos\varphi + \ddot{\psi}\cos\theta\cos\varphi - \dot{\psi}\dot{\theta}\sin\theta\cos\varphi - \dot{\psi}\dot{\varphi}\cos\theta\sin\varphi\end{bmatrix} \tag{2.72}$$

which can be expressed as:

$$\begin{aligned}\begin{bmatrix}\dot{p}\\ \dot{q}\\ \dot{r}\end{bmatrix} = &\underbrace{\begin{bmatrix}1 & 0 & -\sin\theta \\ 0 & \cos\varphi & \cos\theta\sin\varphi \\ 0 & -\sin\varphi & \cos\theta\cos\varphi\end{bmatrix}}_{\mathbf{Q}_1}\underbrace{\begin{bmatrix}\ddot{\varphi}\\ \ddot{\theta}\\ \ddot{\psi}\end{bmatrix}}_{\ddot{\vec{\Theta}}} \\ &+ \underbrace{\begin{bmatrix}0 & -\cos\theta & 0 \\ -\sin\varphi & -\sin\theta\sin\varphi & \cos\theta\cos\varphi \\ -\cos\theta & -\sin\theta\cos\varphi & -\cos\theta\sin\varphi\end{bmatrix}}_{\mathbf{Q}_2}\underbrace{\begin{bmatrix}\dot{\varphi}\dot{\theta}\\ \dot{\theta}\dot{\psi}\\ \dot{\psi}\dot{\varphi}\end{bmatrix}}_{\dot{\vec{\Theta}}_1}\end{aligned} \tag{2.73}$$

therefore:

$$\dot{\vec{\omega}} = \mathbf{Q}_1\ddot{\vec{\Theta}} + \mathbf{Q}_2\dot{\vec{\Theta}}_1 \tag{2.74}$$

Substituting the above expressions into equations (2.69) and (2.70) gives:

$$\vec{F} = m\ddot{\vec{\xi}}_o + m\mathbf{T}\Big(\mathbf{G}_1\mathbf{Q}_1\ddot{\vec{\Theta}} + \mathbf{G}_1\mathbf{Q}_2\dot{\vec{\Theta}}_1 + \mathbf{G}_2\vec{\omega}_1 - \mathbf{G}_3\vec{\omega}_2\Big) \tag{2.75}$$

$$\vec{M}_o = m\mathbf{G}\ddot{\vec{\xi}}_o + \mathbf{T}\Big(\mathbf{I}_o\mathbf{Q}_1\ddot{\vec{\Theta}} + \mathbf{I}_o\mathbf{Q}_2\dot{\vec{\Theta}}_1 + \mathbf{I}_2\vec{\omega}_1 + \mathbf{I}_1\vec{\omega}_2\Big) \tag{2.76}$$

or better:

$$\vec{F} = m\ddot{\vec{\xi}}_o + m\mathbf{T}\mathbf{G}_1\mathbf{Q}_1\ddot{\vec{\Theta}} + m\mathbf{T}\Big(\mathbf{G}_1\mathbf{Q}_2\dot{\vec{\Theta}}_1 + \mathbf{G}_2\vec{\omega}_1 - \mathbf{G}_3\vec{\omega}_2\Big) \tag{2.77}$$

$$\vec{M}_o = m\mathbf{G}\ddot{\vec{\xi}}_o + \mathbf{T}\mathbf{I}_o\mathbf{Q}_1\ddot{\vec{\Theta}} + \mathbf{T}\Big(\mathbf{I}_o\mathbf{Q}_2\dot{\vec{\Theta}}_1 + \mathbf{I}_2\vec{\omega}_1 + \mathbf{I}_1\vec{\omega}_2\Big) \tag{2.78}$$

Now it is possible to join equations (2.77) and (2.78) in one equation involving all the generalised variables $(\ddot{\vec{\xi}}_o, \ddot{\vec{\Theta}})^\intercal = (\ddot{\xi}_o, \ddot{\eta}_o, \ddot{\zeta}_o, \ddot{\varphi}, \ddot{\theta}, \ddot{\psi})^\intercal$. The result is a matrix-vector equation involving all six degrees of freedom

$$\begin{bmatrix} m\mathbf{I} & m\mathbf{T}\mathbf{G}_1\mathbf{Q}_1 \\ m\mathbf{G} & \mathbf{T}\mathbf{I}_\mathbf{o}\mathbf{Q}_1 \end{bmatrix} \begin{bmatrix} \ddot{\vec{\xi}}_o \\ \ddot{\vec{\Theta}} \end{bmatrix} + \begin{bmatrix} m\mathbf{T}\mathbf{G}_1\mathbf{Q}_2 \\ \mathbf{T}\mathbf{I}_\mathbf{o}\mathbf{Q}_2 \end{bmatrix} \left[\dot{\vec{\Theta}}_1\right] + \begin{bmatrix} m\mathbf{T}\mathbf{G}_2 \\ \mathbf{T}\mathbf{I}_2 \end{bmatrix} \left[\vec{\omega}_1\right] + \begin{bmatrix} -m\mathbf{T}\mathbf{G}_3 \\ \mathbf{T}\mathbf{I}_1 \end{bmatrix} \left[\vec{\omega}_2\right] = \begin{bmatrix} \vec{F} \\ \vec{M}_o \end{bmatrix} \tag{2.79}$$

2.4 External forces

The external forces expressed in equation (2.37) can be subdivided according to the nature of the force, such as hydrodynamic $\mathbf{F}_h$, hydrostatic $\mathbf{F}_s$, gravitational $\mathbf{F}_g$ and other external forces $\mathbf{F}_r$ such as wind. Here the force and moment are written together as a generalised vector as follows:

$$\mathbf{F} = \begin{bmatrix} \vec{F} \\ \vec{M}_o \end{bmatrix} \tag{2.80}$$

$$\mathbf{F} = \mathbf{F}_h + \mathbf{F}_s + \mathbf{F}_g + \mathbf{F}_r \tag{2.81}$$

In the present study, the hydrodynamic forces acting on the ship can be caused by the disturbance of the flow created by a rudder deflection (manoeuvring forces) or by the disturbance of the flow by waves (seakeeping forces). In both cases, the disturbances change the flow velocity and pressure around the ship, creating hydrodynamic forces that modify the dynamic state of the ship. From now on, unless otherwise stated, forces and moments will be referred to simply as forces.

2.4.1 Gravitational forces

A direct consequence of gravity is the weight of the ship. The direction of gravity is always aligned with the vertical-axis of the inertial frame ζ, as shown in Figure 2.4. Furthermore, the weight acts as a vector force through the centre of gravity of the ship and in the inertial frame the force is written as shown in equation (2.82).

$$\vec{F}_g = mg \begin{bmatrix} 0 \\ 0 \\ -1 \end{bmatrix} \tag{2.82}$$

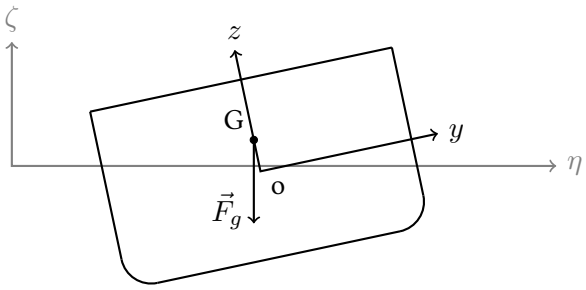

Figure 2.4: Gravitational force calcualtion variables

where m is the mass of the ship and g is the gravity acceleration. Note, that this force does not produce a moment about the centre of gravity, but about the origin of the coordinate system. Thus, the generalized gravitational force reads:

$$\mathbf{F}_g = \begin{bmatrix} \vec{F}_g \\ \vec{r}_G \times \vec{F}_g \end{bmatrix} \tag{2.83}$$

2.4.2 Hydrostatic forces

Hydrostatic forces and moments can be calculated directly if the hydrostatic pressure and ship geometry are known. Typically, the ship is discretized into small panels in the body-fixed coordinate system. A point on the hull surface is denoted by $\vec{r}$ and the vector normal to the surface is $\vec{n}$, as shown in Figure 2.5. The hydrostatic pressure is calculated directly in the inertial coordinate system as $p = \rho g \zeta_r$. Then the hydrostatic force and moment can be calculated as:

$$\vec{F}_s = \iint_S p\mathbf{T}\vec{n}\, dS \tag{2.84}$$

$$\vec{M}_s = \iint_S p\mathbf{T}[(\vec{r} - \vec{r}_G) \times \vec{n}]\, dS \tag{2.85}$$

where S is the wetted ship surface below the free surface, $\mathbf{T}$ is the transformation matrix and $\vec{r}_G$ us the centre of gravity position. Note that the hydrostatic force and moment are calculated in the inertial coordinate system. Thus the generalized hydrostatic force reads:

$$\mathbf{F}_s = \begin{bmatrix} \vec{F}_s \\ \vec{M}_s \end{bmatrix} \tag{2.86}$$

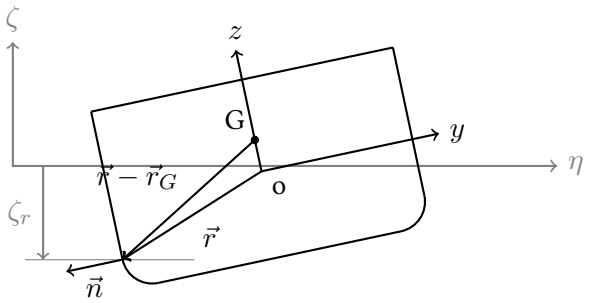

Figure 2.5: Hydrostatic force calculation variables

2.4.3 Hydrodynamic forces

Hydrodynamic forces are of two types, shear force and pressure force. The shear force acts tangential to the surface of a body, while the pressure force—which includes only the contribution of the dynamic pressure—acts perpendicular to the surface. Hydrodynamic forces are the most difficult of all forces to calculate because they require the fluid flow around the ship to be resolved. The numerical methods used to resolve the fluid flow around the ship are described in the next chapter.

2.5 Manoeuvring mathematical models

Manoeuvring mathematical models are a simplified expression of the forces acting on the ship during rudder manoeuvres. Two main types of models can be found in the literature. The formal mathematical model, also known as Abkowitz-type model, inspired by the multi-variable Taylor's expansion and the modular model, based on physical observations (Clarke 2003; Sutulo and Guedes Soares 2011). Both types use hydrodynamic coefficients, which are assumed to be constant, and ship dynamic parameters to calculate the forces. The main difference between the two approaches is how they treat the interaction between the hull, propeller and rudder.

Abkowitz-type manoeuvring models assume that the ship's hull, propeller and rudder are a single system. This means that interactions between its parts are internally balanced and no description of their interactions is required. This allows high accuracy over a range of manoeuvres. At the same time, it implies that no internal part of this system can be modified or changed. Some examples of this model can be found in Abkowitz (1964),

Mucha (2017), and Wolff (1981). The hydrodynamic force is expressed as a function of the ship's acceleration, velocity, rudder deflection δ, and propeller rotation rate n.

$$\mathbf{F}_h = \mathbf{F}(\dot{\vec{v}}, \dot{\vec{\omega}}, \vec{v}, \vec{\omega}, \delta, \dot{\delta}, n, \dot{n}; t) \tag{2.87}$$

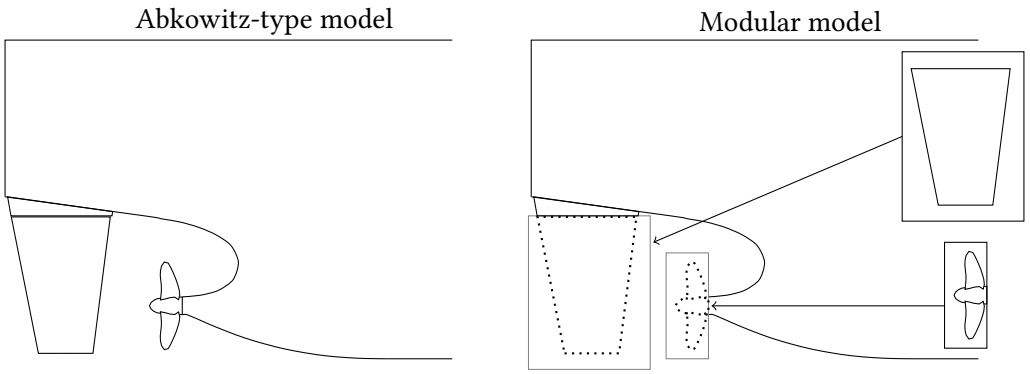

Figure 2.6: Abkowitz based models (left) express the hydrodynamic forces of hull, propeller and rudder together. Modular models (right) express the hull, propeller and rudder independently and approxmate their interaction

Modular models separate the ship's hull, propeller and rudder as independent modular elements. Therefore, in addition to calculating the hydrodynamic forces of each modular component, the relevant interaction effects between the modules should also be modelled. This allows modular models to change the propeller or rudder without affecting the other modules. Only their interaction needs to be corrected. This property is particularly attractive in early ship design, where several prototypes need to be considered. The flexibility of modular approaches is also used to perform more complex manoeuvres and is commonly used in manoeuvring simulators. Some examples of this model can be found in Norrbin (1960), Oltmann and Sharma (1984), and Yasukawa and Yoshimura (2015). The hydrodynamic forces of modular models are expressed as the sum of their components.

$$\mathbf{F}_h = \mathbf{F}_{hull} + \mathbf{F}_{propeller} + \mathbf{F}_{rudder} \tag{2.88}$$

Figure 2.6 sketches the Abkowitz-type model, where the propeller and rudder are fixed to the ship and form a single system. In the modular model, the propeller and rudder are separate modules that can be coupled to the hull. In the present study, the Abkowitz-type model is preferred because higher accuracy for specific manoeuvring scenarios, such as collision avoidance, is required for training autonomous ship algorithms.

2.5.1 Formal mathematical models

The formal mathematical models are based on Abkowitz (1964) and Abkowitz (1969), who proposed a Taylor expansion of the hydrodynamic forces in terms of ship kinematic parameters and rudder deflection for the 3DoF planar motions. The expansion is made from a reference forward speed $u = U_0$ and $v = r = \delta = 0$. Within the formal mathematical models, relevant modifications of the original Abkowitz formulation have been introduced by Wolff (1981) and Mucha (2017).

Note that the proposed mathematical models are not general, but rather depend on the type of ship and the environmental conditions, such as deep or shallow water. Nevertheless, the mathematical expression can be adapted to new conditions by adding some additional terms. The original model of Abkowitz reads:

$$\begin{aligned} X =& X_{\dot{u}}\dot{u} + X_u\Delta u + X_{uu}\Delta u^2 + X_{uuu}\Delta u^3 + X_{vv}v^2 + X_{rr}r^2 + X_{\delta\delta}\delta^2 \\ &+ X_{vr}vr + X_{v\delta}v\delta + X_{r\delta}r\delta + X_{vvu}v^2\Delta u + X_{rru}r^2\Delta u + X_{\delta\delta u}\delta^2\Delta u \\ &+ X_{vru}vr\Delta u + X_{v\delta u}v\delta\Delta u + X_{r\delta u}r\delta\Delta u \end{aligned} \tag{2.89}$$

$$\begin{aligned} Y =& Y_0 + Y_{\dot{v}}\dot{v} + Y_{\dot{r}}\dot{r} + Y_v v + Y_r r + Y_\delta\delta + Y_{vu}v\Delta u + Y_{ru}r\Delta u + Y_{\delta u}\delta\Delta u \\ &+ Y_{vvv}v^3 + Y_{rrr}r^3 + Y_{\delta\delta\delta}\delta^3 + Y_{vrr}vr^2 + Y_{rvv}rv^2 \\ &+ Y_{v\delta\delta}v\delta^2 + Y_{r\delta\delta}r\delta^2 + Y_{vuu}v\Delta u^2 \\ &+ Y_{ruu}r\Delta u^2 + Y_{\delta vv}\delta v^2 + Y_{\delta rr}\delta r^2 + Y_{\delta uu}\delta\Delta u^2 \\ &+ Y_{rv\delta}rv\delta \end{aligned} \tag{2.90}$$

$$\begin{aligned} N =& N_0 + N_{\dot{v}}\dot{v} + N_{\dot{r}}\dot{r} + N_v v + N_r r + N_\delta\delta + N_{vu}v\Delta u + N_{ru}r\Delta u + N_{\delta u}\delta\Delta u \\ &+ N_{vvv}v^3 + N_{rrr}r^3 + N_{\delta\delta\delta}\delta^3 + N_{vrr}vr^2 + N_{rvv}rv^2 \\ &+ N_{v\delta\delta}v\delta^2 + N_{r\delta\delta}r\delta^2 + N_{vuu}v\Delta u^2 \\ &+ N_{ruu}r\Delta u^2 + N_{\delta vv}\delta v^2 + N_{\delta rr}\delta r^2 + N_{\delta uu}\delta\Delta u^2 \\ &+ N_{rv\delta}rv\delta \end{aligned} \tag{2.91}$$

where $\Delta u = u - U_0$ is the variation of the surge velocity from the approach speed. In the expansion, terms higher than third order are considered small and therefore negligible. Here, a simplified notation is used to relate the force and the hydrodynamic coefficients. For example, the simplified notation of equation (2.89) reads:

$$\begin{aligned} X: \quad & \dot{u},\ \Delta u,\ \Delta u^2,\ \Delta u^3,\ v^2,\ r^2,\ \delta^2,\ vr,\ v\delta,\ r\delta, \\ & v^2\Delta u,\ r^2\Delta u,\ \delta^2\Delta u,\ vr\Delta u,\ v\delta\Delta u,\ r\delta\Delta u \end{aligned} \tag{2.92}$$

Table 2.3 shows the mathematical models proposed by Abkowitz, Wolff and Mucha using the simplified notation for a better comparison. In the Abkowitz-model, the hull port-starboard symmetry of the hull is used to disregard odd components in the surge force and even components in sway force and yaw moment. Ships with single-screw propellers generate lateral forces, which are captured by the coefficients Y_0 and N_0. However, Wolff has added the deleted coefficients, arguing that Y_0 and N_0 are insufficient to capture the asymmetry of the forces. Furthermore, Wolff argues that a better representation of the forces is possible by including more terms. For instance, rudder coefficients of fourth and fifth order are used to better capture the rudder forces at large angles.

Mucha (2017) performed a sensitivity study of all the coefficients in the Wolff-model. Mucha varied each coefficient by 20% and evaluated its effect on manoeuvring. The turning circle tactical diameter and zig-zag overshoot angle were evaluated. If the deviation was less than 5%, the coefficient was dropped. As a result, Mucha proposed a reduced model in which only the most relevant coefficients were retained.

Table 2.3: Formal mathematical models. The number 1 represents the constant coefficient Y_0 or N_0. The Abkowitz-model contains 62 coefficients, Wolff-model 84 coefficients, and Mucha-model 31 coefficients.

Model	X	Y & N
Abkowitz	$\dot{u},\ \Delta u,\ \Delta u^2,\ \Delta u^3,$ $v^2,\ r^2,\ \delta^2,\ vr,\ v\delta,\ r\delta,$ $v^2\Delta u,\ r^2\Delta u,\ \delta^2\Delta u,$ $vr\Delta u,\ v\delta\Delta u,\ r\delta\Delta u$	$1, \dot{v},\ \dot{r},\ v,\ r,\ \delta,$ $v^3,\ r^3,\ \delta^3,\ vr^2,\ rv^2,\ v\delta^2,\ r\delta^2,$ $v\Delta u^2,\ r\Delta u^2,\ \delta v^2,\ \delta r^2,\ \delta\Delta u^2,$ $v\Delta u,\ r\Delta u,\ \delta\Delta u,\ rv\delta$
Wolff	$\dot{u},\ \dot{u}u^2,\ u,\ u^2,\ v^2,\ r^2,\ \delta^2,$ $v^2\Delta u,\ r^2\Delta u,\ vr,\ v\delta,\ r\delta,$ $vr\Delta u,\ v\delta\Delta u,\ r\delta\Delta u,$ $v,\ v\Delta u^2,\ r,\ r\Delta u,\ r\Delta u^2,$ $\delta,\ v^2\delta,\ r^2\delta,\ v^2r,\ vr^2,\ \delta^4$	$1, \dot{v},\ \dot{v}v^2,\ \dot{r},\ \dot{r}r^2,\ \Delta u,\ \Delta u^2,$ $v,\ v^2,\ v^3,\ v\Delta u,\ v\Delta u^2,\ vr^2,\ v\delta^2,$ $r,\ r^2,\ r^3,\ r\Delta u,\ r\Delta u^2,\ rv^2,\ r\delta^2,$ $\delta,\ \delta^4,\ \delta^5,\ \delta v^2,\ \delta r^2$ $v\|v\|,\ r\|r\|,\ \delta\|\delta\|$
Mucha	$\dot{u},\ \Delta u,\ \Delta u^2,$ $v^2,\ r^2,\ \delta^2,\ vr$	$1, \dot{v},\ \dot{r},\ v,\ r,\ \delta,\ v^3,\ r^3,\ \delta^3,$ $vr^2,\ rv^2,\ \delta\Delta u$

Mucha's reduced model is attractive because it provides a base model that captures the essential manoeuvring features. It should be noted that these coefficients were obtained using only three seagoing ships (tanker, mariner and ferry) with single-screw propellers and cannot be generalized. Nevertheless, a more complex model can be built on the basis of the Mucha-model.

Another important characteristic of the models is the number of coefficients, which need to be determined. The Abkowitz-model has a total of 62 coefficients, the Wolff-model

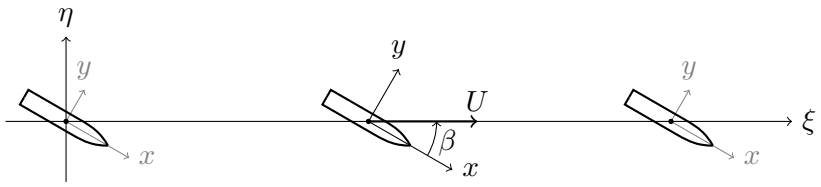

Figure 2.7: Drift test with constant speed U and constant drift angle β. All variables are positive

has 84 coefficients, and the Mucha-model has 31 coefficients. In general, the greater the number of coefficients, the greater the number of tests required to identify them.

2.5.2 Hydrodynamic coefficient identification

There are two main methods for obtaining the hydrodynamic coefficients: direct and indirect system identification. The direct system identification method uses forces measured from captive model tests. Nowadays, these captive tests can be replaced by CFD calculations. The indirect system identification method uses kinematic measurements from free running manoeuvring tests or ship trials to obtain the hydrodynamic coefficients.

For the direct system identification captive model tests are required. These model tests are carried out in specialized hydrodynamic facilities where the environmental conditions are controlled. The tests can be divided into two groups, the steady tests, which aim to achieve a steady-state condition during the test, and the dynamic tests, which use the planar motion mechanism (PMM) to impose a harmonic motion on the ship model. The steady tests are used to obtain coefficients that depend on velocities, whereas the dynamic tests are used to obtain coefficients that depend on both velocity and acceleration. The steady tests are preferred because they provide frequency independent coefficients.

An example of a steady captive test is the oblique resistance test, also known as the drift test, as shown in Figure 2.7. The ship is towed at a constant speed U and a constant drift angle β. The process is repeated for different drift angles, and the forces and moments are measured together with the sinkage and trim. Similarly, steady rudder tests are carried out, but instead of the drift angle, the rudder angle is varied in each test.

Dynamic tests impose the ship model to move harmonically on the ξ-η plane. This means that the position and velocities of the model follow a harmonic motion. Three types of harmonic motion are often used: pure sway, pure yaw and yaw with drift motion. In the pure sway test, the model sways harmonically while advancing with constant surge speed, and the yaw motion is constrained to $\psi = 0$. Figure 2.8 shows a ship model performing a pure sway motion around the centre-line of a towing tank. The carriage moves at constant velocity U_0 while the model is forced to oscillate in sway with an

amplitude y_0. The oscillation is completed every $2\pi U_0/\omega$. The sway velocity and sway acceleration are also harmonic. The period of the oscillation $T = 2\pi/\omega$ characterizes the movement.

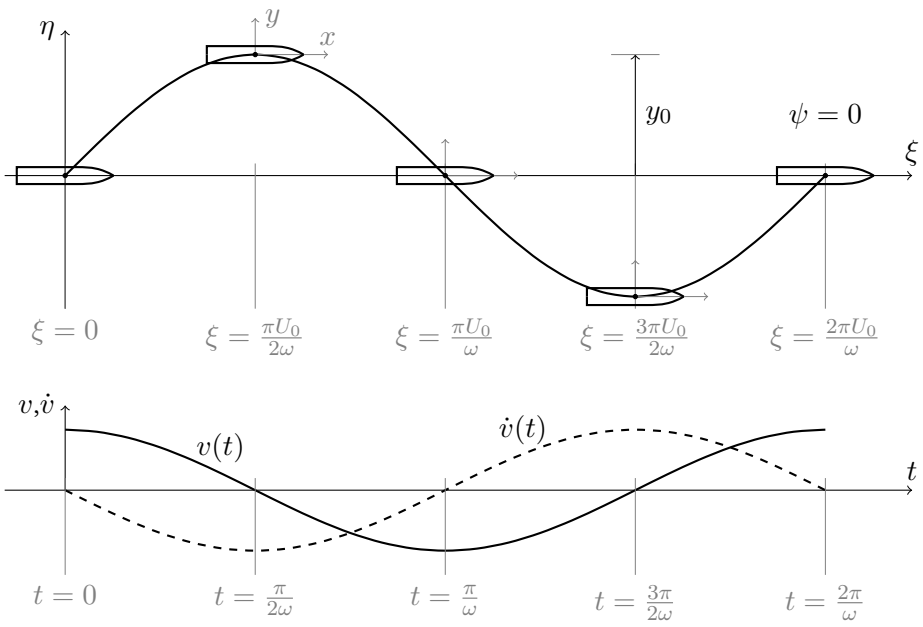

Figure 2.8: Pure sway planar motion with period $T = 2\pi/\omega$

Figure 2.9 shows the pure yaw test, where the ship model is forced to yaw harmonically but it is not allowed to sway. This is achieved by forcing the ship's model orientation to follow the ship's path tangentially, as shown in Figure 2.9. The drift angle is therefore zero at all times ($\beta = 0$), which means there is no sway velocity.

Once the forces and moments have been obtained from the captive tests, a multivariable regression is performed to identify the hydrodynamic coefficients. A common procedure is to obtain the coefficients step by step, where a test is used to find coefficients that are directly dependent on the variable that was varied in the captive test, thus reducing the number of coefficients to be identified in each step. Alternatively, a procedure based on linear regression using all tests simultaneously may be more advantageous, as this approach minimizes the global error of the system identification.

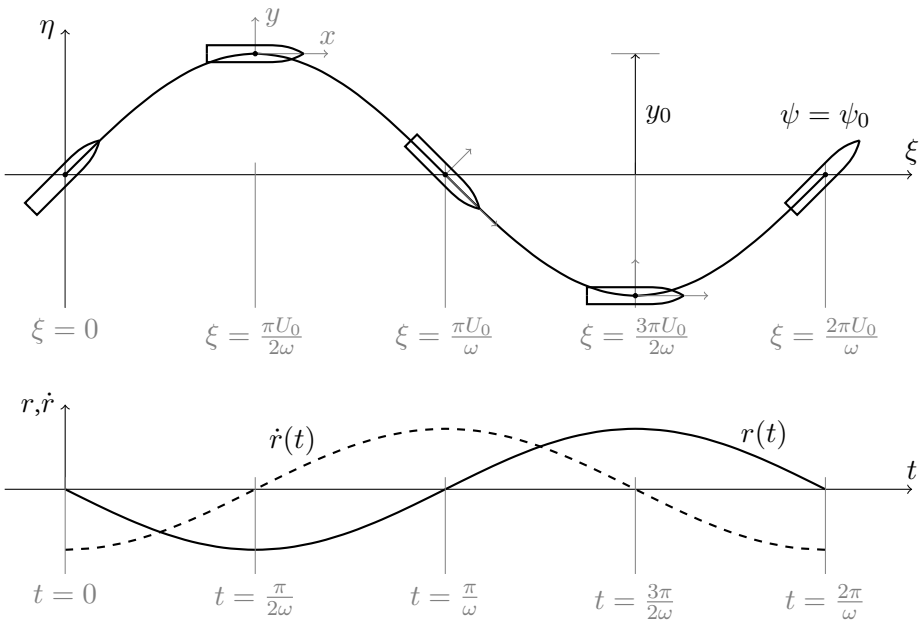

Figure 2.9: Pure yaw planar motion with period $T = 2\pi/\omega$

3 Numerical methods

Accurate calculation of external forces is the key component in predicting ship dynamics. Due to the different nature of the external forces, different numerical methods were used to calculate these forces. Viscous related forces were calculated using the Reynolds-averaged Navier-Stokes (RANS) equations. The added masses were calculated using the Euler equations. The commercial solver STAR-CCM+ (Siemens Digital Industries Software 2021) was used for both methods. Finally, the wave-induced forces were calculated using potential flow theory by means of the GLRankine solver (von Graefe 2014). A brief summary of these three numerical methods is given in this chapter.

3.1 Reynolds-averaged Navier-Stokes equations

The Reynolds-averaged Navier-Stokes equations are one of the best practical methods for modelling complex turbulent flows. A detailed derivation of the equations and description of the method can be found in Ferziger et al. (2020). The RANS equations are derived from the continuity equation (3.1) and the Navier-Stokes equation (3.2), which represent the conservation of mass and momentum, respectively, of a control volume. Although solving the Navier-Stokes equations, (3.1) and (3.2), should be sufficient to determine the turbulent flow around the ship, the numerical solution of these equations for marine hydrodynamics is still practically impossible. The Navier-Stokes equations for incompressible flows are as follows:

$$\frac{\partial}{\partial t}\int_V \rho dV + \int_S \rho \mathbf{v}\cdot\mathbf{n}dS = 0 \tag{3.1}$$

$$\frac{\partial}{\partial t}\int_V \rho \mathbf{v}dV + \int_S \rho \mathbf{v}\mathbf{v}\cdot\mathbf{n}dS = \int_S (\boldsymbol{\tau} - p\mathbf{I})\cdot\mathbf{n}dS + \int_V \rho\mathbf{b}dV \tag{3.2}$$

where ρ is the fluid density, t is time, V is the volume of a control volume (CV), S is the boundary surface of a control volume, $\mathbf{n}$ is an outward surface normal vector, $\mathbf{v}$ is a velocity vector of the fluid, p is pressure, $\mathbf{b}$ is a body force per unit mass, $\mathbf{I}$ is the unit

tensor, and $\boldsymbol{\tau}$ is the viscous stress tensor defined in equation (3.3) , with μ being the fluid dynamic viscosity, also known as molecular viscosity, and $\mathbf{D}$ the rate of strain tensor.

$$\boldsymbol{\tau} = \mu\big[\nabla\mathbf{v} + (\nabla\mathbf{v})^T\big] = 2\mu\mathbf{D}, \quad \text{with} \quad \mathbf{D} = \frac{1}{2}\big[\nabla\mathbf{v} + (\nabla\mathbf{v})^T\big] \tag{3.3}$$

A direct numerical simulation (DNS), which is the numerical solution of the Navier-Stokes equations, requires extremely fine discretizations in space and time to resolve all turbulent vortex scales. It is well known that the size of turbulent vortices decreases with increasing Reynolds number. This increases the difficulty of performing DNS, especially in marine hydrodynamics, which is characterized by high Reynolds number flows.

In many marine applications, the variable of interest is an averaged value, such as ship resistance. In these cases, the Reynolds-averaged Navier-Stokes (RANS) equations can be used. In general, ensemble averaging of the Navier-Stokes equations is used to derive the transient RANS equations and the time-averaging of the Navier-Stokes equations is used to derive the steady state RANS equations. Their derivation is based on the assumption that velocities and pressures are decomposed into mean values and turbulent fluctuations as follows:

$$\mathbf{v} = \overline{\mathbf{v}} + \mathbf{v}' \qquad \text{and} \qquad p = \overline{p} + p' \tag{3.4}$$

where $\overline{\mathbf{v}}$ and $\overline{p}$ are the time averages of velocity and pressure, respectively, and $\mathbf{v}'$ and p' are their fluctuations. This time-averaging of the Navier-Stokes equations, introduced by Reynolds, represents a statistical consideration of turbulence. This approach is appropriate for most engineering applications, where only the average flow quantities are of interest. Inserting equation (3.4) into the Navier-Stokes equations and averaging them (note that averages of fluctuating quantities are by definition zero) gives the Reynolds-averaged Navier-Stokes equations:

$$\frac{\partial}{\partial t}\int_V \rho dV + \int_S \rho\overline{\mathbf{v}}\cdot\mathbf{n}dS = 0 \tag{3.5}$$

$$\frac{\partial}{\partial t}\int_V \rho\overline{\mathbf{v}}dV + \int_S \rho\overline{\mathbf{v}}\,\overline{\mathbf{v}}\cdot\mathbf{n}dS = \int_S (\boldsymbol{\tau} - \overline{p}\mathbf{I} - \rho\overline{\mathbf{v}'\mathbf{v}'})\cdot\mathbf{n}dS + \int_V \rho\mathbf{b}dV \tag{3.6}$$

The averaging process of most terms produces only their mean value, but the averaging of the convective term $\rho\mathbf{vv}$ results in an additional term with six new unknowns of the form $\rho\overline{\mathbf{v}'\mathbf{v}'}$. Analogous to the viscous stress tensor, $\boldsymbol{\tau}$, this term is called the Reynolds stress tensor, although it describes a transport process and must be modelled to close the system of equations.

3.1.1 Turbulence modelling

The aim of the turbulence modelling is to provide a closure for the RANS equations. From the literature, two main approaches appear to be appropriate for ship hydrodynamics: eddy viscosity models and the Reynolds stress transport model. A detailed explanation of turbulence modelling can be found in Wilcox (1993).

Eddy viscosity models are based on the Boussinesq approximation, which assumes that the Reynolds stress is a linear function of the mean velocity gradients. For incompressible flows, this reads as follows:

$$\boldsymbol{\tau}_R = -\rho\overline{\mathbf{v}'\mathbf{v}'} = \mu_t\left[\nabla\overline{\mathbf{v}} + (\nabla\overline{\mathbf{v}})^T\right] - \frac{2}{3}\rho k\mathbf{I} \tag{3.7}$$

where μ_t is the turbulent eddy viscosity, which is flow dependent, and k is the turbulent kinetic energy defined as follows:

$$k = \frac{1}{2}\overline{\mathbf{v}' \cdot \mathbf{v}'} \tag{3.8}$$

This model of the Reynolds stress is called the eddy viscosity model because of its analogy to the viscous stress tensor and molecular viscosity. This model reduces the six unknowns of the Reynolds stress tensor, $\rho\overline{\mathbf{v}'\mathbf{v}'}$, to the two unknowns μ_t and k. The k-ϵ and the k-ω turbulence models are typical examples of eddy viscosity models. In this thesis, the k-ω shear-stress-transport (SST) variant of Menter (1994) was used. This method combines the k-ϵ and k-ω models, taking advantage of the better prediction of the k-ϵ model in the shear layers and the better prediction of the k-ω model in the boundary layers. It should be noted that this modelling approach considers only isotropic turbulence, i.e. the turbulence properties are independent of direction. The turbulent kinetic energy transport equations, k, and the specific dissipation rate transport equation, ω, are given by:

$$\frac{\partial\rho k}{\partial t} + \nabla\cdot(\rho\mathbf{v}k) = \nabla\cdot\left[\left(\mu + \frac{\mu_t}{\sigma_k}\right)\nabla k\right] + S^k \tag{3.9}$$

$$\frac{\partial\rho\omega}{\partial t} + \nabla\cdot(\rho\mathbf{v}\omega) = \nabla\cdot\left[\left(\mu + \frac{\mu_t}{\sigma_\omega}\right)\nabla\omega\right] + S^\omega \tag{3.10}$$

where σ_k and σ_ω are constants, and S^k and S^ω stand for auxiliary relations.

The Reynolds stress model (RSM) calculates each component of the Reynolds-stress tensor $\boldsymbol{\tau}_R$ directly by solving its respective governing transport equation. The additional

equations are obtained by multiplying the Navier-Stokes equation by a fluctuating property and then time averaging the product, yielding:

$$\frac{\partial \tau_{ij}}{\partial t} + \overline{u}_k \frac{\partial \tau_{ij}}{\partial x_k} = -\left(\tau_{ik}\frac{\partial \overline{u}_j}{\partial x_k} + \tau_{jk}\frac{\partial \overline{u}_i}{\partial x_k}\right) + \epsilon_{ij} - \mathbf{\Pi}_{ij} + \frac{\partial}{\partial x_k}\left(\nu\frac{\partial \tau_{ij}}{\partial x_k} + C_{ijk}\right) \tag{3.11}$$

where

$$\text{Pressure-strain :} \qquad \mathbf{\Pi}_{ij} = \overline{p'\left(\frac{\partial u_i'}{\partial x_j} + \frac{\partial u_j'}{\partial x_i}\right)} \tag{3.12}$$

$$\text{Disipation tensor :} \qquad \epsilon_{ij} = \overline{2\mu\frac{\partial u_i'}{\partial x_k}\frac{\partial u_j'}{\partial x_i}} \tag{3.13}$$

$$\text{Turbulent diffusion :} \qquad C_{ijk} = \rho\overline{u_i'u_j'u_k'} + \overline{p'u_i'}\delta_{jk} + \overline{p'u_j'}\delta_{ik} \tag{3.14}$$

The Reynolds stress model has the potential to predict complex flows. Some of its advantages are the ability to account for turbulence anisotropy, streamline curvature, swirl rotation and high strain rates. At the same time, this modelling increases the computational time and makes the numerical solution stiffer.

3.1.2 Pressure equation

Pressure is a state variable that must be determined in order to calculate the hydrodynamic forces acting on the ship. For incompressible flows, there is no explicit equation from which the pressure can be determined. It is therefore derived by taking the divergence of the momentum equation, which yields:

$$\nabla^2 p = \nabla\cdot(\nabla p) = -\nabla\cdot\left[\frac{\partial \rho\mathbf{v}}{\partial t} + \nabla\cdot(\rho\mathbf{v}\mathbf{v} - \boldsymbol{\tau}) - \rho\mathbf{g}\right] \tag{3.15}$$

This equation is further simplified if the density, viscosity and body force are constants. Then the transient and viscous terms vanish by virtue of the continuity equation:

$$\nabla^2 p = -\nabla\cdot[\nabla\cdot(\rho\mathbf{v}\mathbf{v})] \tag{3.16}$$

There are two approaches to obtaining the pressure, the first approach aims to compute the pressure itself in the next iteration, while the second approach defines the pressure as the sum of an older pressure value plus a pressure correction, $p = p^{\text{old}} + p'$. In the second approach, only p' needs to be calculated in each iteration.

The pressure and momentum equations are solved using an iterative procedure. First, the momentum equation is solved using previously known values of the pressure, result-

ing in a new velocity estimate. Second, the pressure equation is solved using the new velocity estimate. The updated pressure estimate is used in the momentum equation and the cycle continues until the changes in the pressure field satisfy a convergence condition. This iterative process is known as the semi-implicit method for pressure linked equations (SIMPLE) algorithm.

3.1.3 Free surface flows

Ship hydrodynamics involves the interaction of two immiscible fluids: water and air. The volume of fluid (VOF) method is used to capture the interface between air and water, i.e. the free surface. This method uses an additional transport equation with the variable α as shown in the equation (3.17). This variable is called the volume fraction and quantifies the volume of water or air within a control volume, i.e. $\alpha = V_{fluid}/V_{CV}$. Here, the value of $\alpha = 0.5$ indicates the free surface, which corresponds to the interface between water and air.

$$\frac{\partial}{\partial t}\int_V \alpha dV + \int_S \alpha \mathbf{v}\cdot\mathbf{n}dS = 0 \tag{3.17}$$

Although water and air are modelled, the fluid properties are treated as a single fluid, whose properties vary in space according to the volume fraction of each phase.

$$\rho = \rho_{water}\alpha + \rho_{air}(1-\alpha), \quad \mu = \mu_{water}\alpha + \mu_{air}(1-\alpha), \tag{3.18}$$

The VOF modelling requires a fine grid resolution around the free surface to resolve accurately and avoid numerical diffusion. Furthermore, the high-resolution interface capturing (HRIC) scheme, developed by Muzaferija and Peric (1999), is used to obtain a sharp interface. This scheme mimics the convective transport of the two immiscible fluids.

3.1.4 Boundary conditions

The RANS equations are supplemented by a set of boundary conditions. Two types are often used: the Dirichlet and the Neumann boundary conditions. The Dirichlet condition specifies the value of the variable and the Neumann condition specifies its gradient.

Figure 3.1 shows typical boundary conditions used in ship hydrodynamics. At the hull boundary, the no-slip wall condition is specified, i.e. the fluid particles in contact with the hull stick to the surface and move at the same velocity as the surface—a Dirichlet boundary condition. The flow velocity is specified at the velocity inlet. The hydrostatic pressure is specified at the pressure outlet, which is far from the ship wave disturbance. At the bottom boundary, the no-slip wall condition is specified with an additional tangential

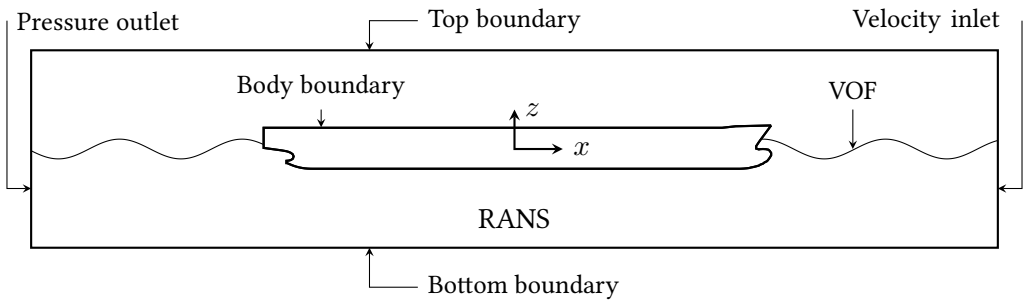

Figure 3.1: RANS boundary conditions

velocity. This velocity is equal to the relative velocity between the ship and the bottom. At the top boundary, and at the sides of the numerical domain, the velocity is specified.

3.1.5 Numerical solution

The numerical solution of the RANS equations is performed using the finite volume method (FVM). This method transforms the integral differential equations into discrete algebraic equations over finite volumes. Therefore, the numerical domain is divided into a finite number of small control volumes whose faces are shared by adjacent control volumes. This discretized domain is referred to as the grid or mesh of the numerical domain. A detailed description of the method can be found in Moukalled et al. (2016). Here, a brief overview of the features of the method is presented on the generic conservation equation of a scalar quantity ϕ. For simplicity, I consider only the steady-state problem. Therefore, the transient term is dropped and the equation becomes:

$$\underbrace{\int_S \rho\phi\mathbf{v}\cdot\mathbf{n}dS}_{\text{Convective term}} = \underbrace{\int_S \Gamma\nabla\phi\cdot\mathbf{n}dS}_{\text{Diffusive term}} + \underbrace{\int_V qdV}_{\text{Source term}} \tag{3.19}$$

where Γ is the diffusivity for the quantity ϕ and q is the source or sink of ϕ. The integrals in equation (3.19) are approximated using Gaussian quadrature. Usually only one point is used, located at the centroid of the control volume or the centroid of the surface. This approximation gives second order accuracy and is exact if the integrated function is linear.

Convective term The surface integral over a control volume is equal to the sum of the fluxes through each face. Each surface flux is evaluated using Gaussian quadrature with a point located at the centroid of the face.

$$\int_S \rho\phi\mathbf{v}\cdot\mathbf{n}dS = \sum_{f=1}^{faces}\int_f(\rho\phi\mathbf{v})\cdot\mathbf{n}dS \approx \sum_{f=1}^{faces}(\rho\phi\mathbf{v}\cdot\mathbf{n})_f S_f \tag{3.20}$$

Diffusion term The procedure is similar to the convective term. The surface integral over the control volume is equal to the sum of the fluxes in each face.

$$\int_S \Gamma\nabla\phi\cdot\mathbf{n}dS = \sum_{f=1}^{faces}\int_f(\Gamma\nabla\phi)\cdot\mathbf{n}dS \approx \sum_{f=1}^{faces}(\Gamma\nabla\phi\cdot\mathbf{n})_f S_f \tag{3.21}$$

Source term Volume integration is approximated by Gaussian quadrature integration. When using one point, it is located at the centroid of the control volume. Thus, q_C is the source evaluated at the centroid and V is the volume of the control volume.

$$\int_V qdV \approx q_C V \tag{3.22}$$

The result of the discretized equation for one integration point, is shown in equation (3.23). Where the flux terms are evaluated in the face centroid and the source term in the control volume centroid. Further steps aim to express the face and volume fluxes in terms of the neighbouring values and to linearize the equation.

$$\sum_{f=1}^{faces}(\rho\phi\mathbf{v}-\Gamma\nabla\phi)_f\cdot\mathbf{S}_f = q_C V \tag{3.23}$$

3.1.6 Numerical error estimation

The calculation of forces by numerical methods contains errors. Quantifying the error is an important aspect of the calculation, not only for accuracy purposes but also to know how reliable the calculations are. For numerical calculations, three main sources of error have been identified: modelling error, input error and numerical error. The modelling error can be large if the wrong set of equations is chosen. It is therefore necessary to rely on previous studies to select the most appropriate model for a given physical phenomenon. Input errors arise from the difference between the physical and numerical conditions,

such as the domain size or initial conditions. The numerical error is the sum of all errors introduced in the numerical solution of the equations.

The numerical error is defined as the difference between the exact (analytical) solution of the equations and the calculated (discretized) solution. Four numerical errors are distinguished: round-off error, iterative error, statistical error and discretization error. The latter is usually the largest error and its estimation is necessary to ensure the quality of the simulations.

I used the approach of Oberhagemann and el Moctar (el Moctar, Schellin, et al. 2021; Oberhagemann 2016) to calculate the discretization errors. This method considers a uniform refinement in all directions (space and time), which means that the Courant number is kept constant. Time is considered as a fourth direction, which seems particularly useful for free surface flows. The one dimensional Courant number (CFL) is defined as follows:

$$CFL = \frac{u\Delta t}{\Delta x} \tag{3.24}$$

where u is the water particle velocity, Δt is the time step, and Δx is the grid spacing. For an unstructured grid discretization, one option is to have the grid topology depend on a base size and be maintained for each grid. This means that the entire discretization of the domain is related to this unique base topology (Burmester et al. 2020; Mewes 2021). In this method, the coarsest grid is the reference grid, and the refined grids are obtained by systematic refinement using refinement factors r_x, r_y, r_z, and r_t. The r_x factor is equal to the grid spacing of the reference grid divided by the grid spacing of the refined grid. The refinement factors read:

$$r_x = \frac{\Delta x_{i+1}}{\Delta x_i}, \quad r_y = \frac{\Delta y_{i+1}}{\Delta y_i}, \quad r_z = \frac{\Delta z_{i+1}}{\Delta z_i}, \quad r_t = \frac{\Delta t_{i+1}}{\Delta t_i}, \tag{3.25}$$

The index i is the level of refinement. r_x, r_y, r_z, and r_t are the refinement factors in x, y, z directions and time respectively. Note that all this refinement factors are advised to be the same. The spatial grid refinement ratio, Υ, determined from equation (3.26), gives a normalized grid scale in which $\Upsilon = 1$ represents the coarser grid, and $\Upsilon = 0$

represents the limit case in which the grid space Δx, Δy, Δz and time step Δt approach zero. Hence, representing the grid-independent solution.

$$\begin{aligned}\Upsilon_i &= \sqrt{\frac{1}{4}\left[\left(\frac{\Delta x_i}{\Delta x_1}\right)^2+\left(\frac{\Delta y_i}{\Delta y_1}\right)^2+\left(\frac{\Delta z_i}{\Delta z_1}\right)^2+\left(\frac{\Delta t_i}{\Delta t_1}\right)^2\right]} \\ &= \sqrt{\frac{1}{4}\left[\left(\frac{1}{r_x}\right)^{2(i-1)}+\left(\frac{1}{r_y}\right)^{2(i-1)}+\left(\frac{1}{r_z}\right)^{2(i-1)}+\left(\frac{1}{r_t}\right)^{2(i-1)}\right]}\end{aligned} \tag{3.26}$$

The associated discretization error, δ_D, is defined as follows:

$$\delta_D = \phi_i - \phi_0 = a_1\Upsilon_i + a_2\Upsilon_i^2 + ... \tag{3.27}$$

where, ϕ is the solution of interest, ϕ_i is the solution obtained on grid i, and ϕ_0 is the extrapolated (grid-independent) solution. Constants a_1 and a_2 correspond to the error level, and their values are determined by the least squares method shown in equation (3.28) with three refinement levels ($n_g = 3$).

$$S_2(\phi_0, a_1, a_2) = \sqrt{\sum_{i=1}^{n_g}(\phi_i - (\phi_0 + a_1\Upsilon_i + a_2\Upsilon_i^2))^2} \tag{3.28}$$

The associated uncertainty of the numerical calculation was calculated according to equation (3.29) of Mewes (2021). The convergence ratio P represents the order of convergence between the theoretical and the observed solutions. The safety factor of $F_s = 1.25$ is applied for monotonically converging solutions, where the order of convergence is in a similar range to the theoretical order of convergence, i.e. the convergence ratio P is close to unity. Otherwise, the safety factor would be $F_s = 3.0$.

$$U(\phi_i) = F_s\delta_D(\phi_i), \quad \text{with:} \quad F_s = \begin{cases} 1.25 & 0.8 < P < 1.2 \text{ \& Monotonic} \\ 3.0 & \text{otherwise} \end{cases} \tag{3.29}$$

3.2 Euler method

In many practical hydrodynamic problems, the effects of viscosity are very small. For instance, if the boundary layer is thin, the fluid can be considered to be inviscid. In such a cases the viscosity can be neglected. Thus, the stress tensor is reduced only to its pressure

component $\mathbf{T} = -p\mathbf{I}$. In other words the viscous stress tensor $\boldsymbol{\tau}$ is set to zero. Replacing it in the Navier-Stokes equations yields

$$\frac{d}{dt}\int_V \rho dV + \int_S \rho \mathbf{v} \cdot \mathbf{n} dS = 0 \tag{3.30}$$

$$\frac{d}{dt}\int_V \rho \mathbf{v} dV + \int_S \rho \mathbf{v}\mathbf{v} \cdot \mathbf{n} dS = -\int_S p\mathbf{I} \cdot \mathbf{n} dS + \int_V \rho \mathbf{b} dV \tag{3.31}$$

An important physical consequence of using the Euler equations is the absence of the boundary layer in the flow solution.

The numerical solution of the Euler equations is carried out using the finite volume method. Therefore, the description given in the previous section is also valid for the solution of the Euler equations.

3.3 Potential flow

Potential flow equations are a further simplification of the Euler equations. If the fluid is assumed to be inviscid and the flow is irrotational $\nabla \times \mathbf{v} = 0$, then a velocity potential $\phi(\mathbf{x}, t)$ exists and, thus, the velocity can be expressed as: $\mathbf{v} = \nabla\phi$. This description of the velocity $\mathbf{v}$ as the gradient of a velocity potential ϕ, reduces the three velocity unknowns to just one. As a result, the conservation of mass is reduced to the Laplace equation (3.32), and the conservation of momentum is reduced to the integral Euler equation (3.33), better known as Bernoulli's equation. A detailed description of the method can be found in el Moctar, Schellin, et al. (2021).

$$\nabla \cdot \mathbf{v} = \nabla^2\phi = 0 \tag{3.32}$$

$$\frac{\partial\phi}{\partial t} + \frac{1}{2}(\nabla\phi \cdot \nabla\phi) + \frac{p}{\rho} + gz = C(t) \tag{3.33}$$

Where g is the gravitational acceleration and $C(t)$ is an arbitrary constant that may depend on time but not on spatial variables. Furthermore, due to the large difference in the density between air and water, hydrodynamic forces dominate and aerodynamic forces can be neglected in seakeeping problems. Therefore, only the water flow is modelled.

The problem of a ship travelling straight ahead at constant speed U in waves is formulated as a boundary value problem (BVP). The mathematical tool known as boundary integral equations (BIE) is used to analyse the BVP. The numerical solution of the BIE is called the boundary element method (BEM). This sequence is commonly used by seakeeping methods based on potential flow theory. Within the boundary value problem a

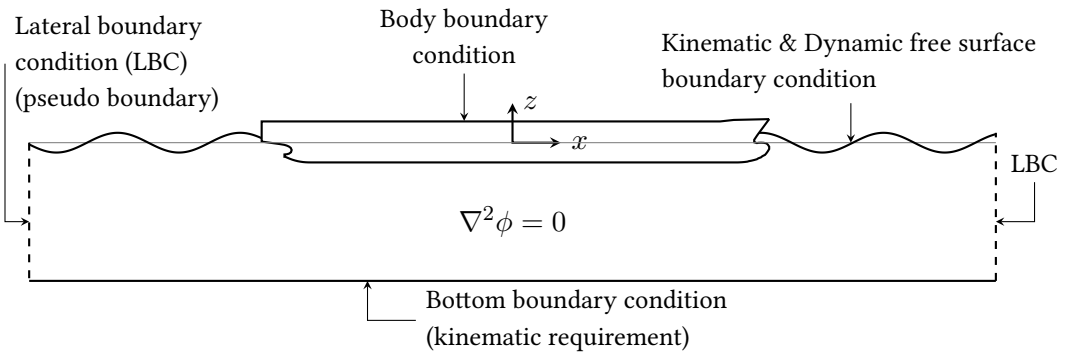

Figure 3.2: Seakeeping boundary value problem

portion of the fluid surrounding the ship is chosen as the region of interest, together with the boundary that encloses it, as shown in Figure 3.2. The governing differential equation within the region and the boundary conditions read:

$$\nabla^2\phi = 0 \qquad \text{within the fluid domain} \tag{3.34}$$

$$\frac{\partial\phi}{\partial t} - \frac{1}{2}|\nabla\phi|^2 + g\zeta - \frac{1}{2}U^2 = 0 \qquad \text{on the free surface} \tag{3.35}$$

$$\frac{\partial\phi}{\partial z} - \frac{\partial\zeta}{\partial t} - \nabla\phi\cdot\nabla\zeta = 0 \qquad \text{on the free surface} \tag{3.36}$$

$$\nabla\phi\cdot\mathbf{n} = 0 \qquad \text{on the body surface} \tag{3.37}$$

$$\nabla\phi\cdot\mathbf{n} = 0 \qquad \text{on the bottom} \tag{3.38}$$

Note, that in general the velocity potential $\phi(\mathbf{x}, t)$ depends on space $\mathbf{x}$ and time t, and is formulated in a coordinate system moving at the average ship forward speed U. The potential ϕ is composed of five parts as shown in equation (3.39). The first two components are steady in the body fixed coordinate system and the last three potentials oscillate periodically with the encounter frequency ω.

$$\phi(\mathbf{x}, t) = -Ux + \phi_0 + \phi_w + \phi_d + \sum_{j=1}^{6}\phi_j \tag{3.39}$$

where:

$-Ux$	:	potential of the parallel inflow
ϕ_0	:	potential of the steady disturbance of the inflow due to the hull
ϕ_w	:	potential of the wave flow propagation
ϕ_d	:	potential of the diffracted flow due to wave
ϕ_j	:	potential of the radiated flow due to ship motion

The lateral boundary condition can have different expressions depending on the problem. For instance, when waves propagate in a large domain, the lateral boundary conditions are periodic in space and time and can be expressed as a periodic condition depending on the wave length λ and the wave period T.

$$\phi(x,t) = \phi(x+\lambda,t) \tag{3.40}$$

$$\phi(x,t) = \phi(x,t+T) \tag{3.41}$$

To solve the BVP, a fundamental solution of the Laplace equation (sources and sinks) is distributed over the boundary surfaces. At the beginning, the sources and sinks were placed on the boundary, requiring special integration methods to avoid the singularities. A practical option is to place the fundamental solution shifted from the boundary out of the fluid domain, which is known as desingularised boundary integral equation (Cao et al. 1991). Two types of non-singular boundary integral formulations are available: direct and indirect. The direct method uses the Green's second identity to derive the boundary integral equation. In the indirect method the velocity potential is expressed as the integration of fundamental solution distributed over a surface shifted from the boundary as shown in:

$$\phi(\mathbf{x}) = \int_S \sigma(\mathbf{x}_s) G(\mathbf{x}, \mathbf{x}_s) ds \tag{3.42}$$

where G represents a fundamental solution of the Laplace equation and σ its strength. $\mathbf{x}_s$ is location of the fundamental solution outside the fluid region.

3.3.1 Numerical solution

The boundary integral equations are solved numerically using a boundary element method developed by Söding, Shigunov, et al. (2014) and Söding, von Graefe, et al. (2013). The solution of the velocity potential is performed sequentially as shown in Figure 3.3, where each block corresponds to one sub-problem. Each sub-problem is solved with a similar procedure and an example is given here for the steady potential. A detailed description of the method can be found in von Graefe (2014).

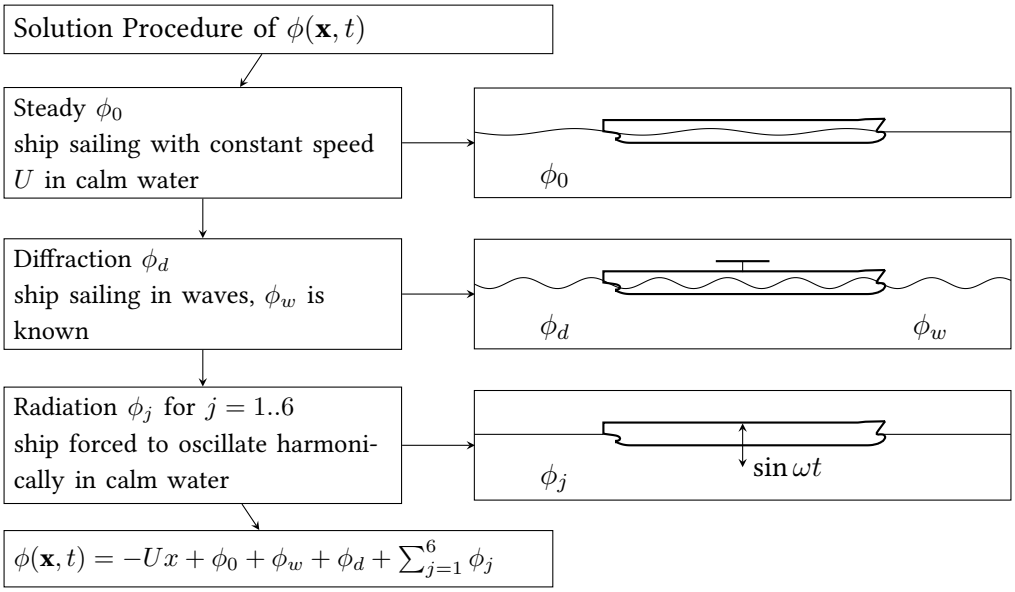

Figure 3.3: Seakeeping BVP general solution.

The problem of a ship travelling straight ahead with constant velocity $\mathbf{U} = (U, 0, 0)^\intercal$ is formulated. The boundary value problem is nonlinear in the free surface and an iterative process is used to find the solution. The equations in the domain and the boundary conditions that the steady potential ϕ_0 must satisfy read:

$$\Delta\phi_0 = 0 \qquad \text{within the fluid domain} \tag{3.43}$$

$$\mathbf{U} \cdot \nabla\phi_0 - \frac{1}{2}|\nabla\phi_0|^2 + g\zeta = 0 \qquad \text{on the free surface} \tag{3.44}$$

$$(\nabla\phi_0 + \mathbf{U}) \cdot \mathbf{n} = 0 \qquad \text{on the free surface} \tag{3.45}$$

$$(\nabla\phi_0 + \mathbf{U}) \cdot \mathbf{n} = 0 \qquad \text{on the body surface} \tag{3.46}$$

$$\nabla\phi_0 \cdot \mathbf{n} = 0 \qquad \text{on the bottom} \tag{3.47}$$

For the numerical solution, the boundary surface is discretized. An unstructured triangular grid is used on the submerged ship surface and a block-structured quadrilateral grid is employed on the free surface. Rankine sources are chosen as fundamental solution and are located at points ξ_j outside of the fluid slightly above centre points of each panel. The bottom condition is treated employing mirror image of the original sources with respect to a flat bottom. Thus, the potential can be expressed as superposition of Rankine sources:

$$\phi_0(\mathbf{x}) = \sum_{j=1}^{n} q_j G(\mathbf{x}, \xi_j) \tag{3.48}$$

$$G(\mathbf{x}, \xi_j) = \frac{1}{|\mathbf{x} - \xi_j|} \tag{3.49}$$

The patch method (Söding 1993) is used to satisfy the boundary conditions (3.45) to (3.47). In this method, the boundary conditions are fulfilled in the average over each panel τ_i and not at discrete collocation points. In order to fulfil boundary conditions on the body and on the free surface, the residuum for a panel τ_j is introduced, equal to the total flow through the panel.

$$r_i = \int_{\tau_i} (\nabla\phi_0 + \mathbf{U}) \cdot \mathbf{n} dS = \sum_{j=1}^{n} q_j \int_{\tau_i} \nabla G(\mathbf{x}, \xi_j) \cdot \mathbf{n}\, dS + \int_{\tau_i} \mathbf{U} \cdot \mathbf{n}\, dS = 0 \tag{3.50}$$

$$r_i = \sum_{j=1}^{n} q_j a_{ij} + \int_{\tau_i} \cdot n\, dS \quad \text{with} \quad a_{ij} = \int_{\tau_i} \nabla G(\mathbf{x}, \xi_j) \cdot \mathbf{n}\, dS \tag{3.51}$$

The variable a_{ij} is the solid angle of the triangular shaped panel τ_i seen from the source point ξ_j. The integration over each panel leads to a system of equations with equal number of unknown source strengths q_j. Once the solution is obtained the wave elevation ζ is computed using (3.44). However, the potential ϕ_0 depends on ζ. Thus, an iterative process is carried out. Once the potential is known the total pressure is computed using equation (3.52) and hydrodynamic forces and moments are calculated.

$$p = \frac{\rho}{2}\left(|\mathbf{U}|^2 - |\mathbf{U} + \nabla\phi|^2\right) - \rho g z \tag{3.52}$$

The position of the panel centroid is used in the computation of the hydrostatic pressure.

4 Manoeuvring in shallow water

This chapter presents my contributions to the field of manoeuvring in shallow water. A mathematical manoeuvring model for inland waterway ship was developed taking into account shallow water conditions. In order to obtain a reliable and accurate mathematical model, the intermediate procedures involved in the calculation of forces and the identification of hydrodynamic coefficients were critically reviewed. As a result, efficient numerical methods for calculating the hydrodynamic coefficients are presented. A new method for calculating the added mass coefficients at zero frequency based on the Euler equations is introduced. Furthermore, the viscous related hydrodynamic forces are calculated using RANS based captive test on a fully appended ship, i.e. physical modelling of hull, propellers and rudders, which is beyond the state of the art. An alternative method to obtain the hydrodynamic coefficients based on ship kinematics and rudder angle measurements from free running tests is presented. Finally, the mathematical model is validated with trajectories of free running manoeuvres of a typical inland waterway ship sailing the Rhine River.

4.1 Mathematical model for manoeuvring in shallow water

I present an Abkowitz-type mathematical manoeuvring model for inland waterway ships, which typically have complex stern geometries with ducted propellers and twin-rudders. The method is intended to cover the manoeuvring in shallow water and extreme shallow water conditions. The derivation of the model is described in detail.

4.1.1 Model derivation

The hydrodynamic manoeuvring forces are described by means of an Abkowitz-type mathematical model. The hydrodynamic force is expressed as a function of the ship's acceleration, its velocity and its rudder deflection. It is assumed that this force is divided as shown in equation (4.1), where the first term represents the forces induced by the ac-

celeration; a change in acceleration also produces a change in velocity. The second term represents the forces induced by velocity and rudder deflection.

$$\mathbf{F}_h(\dot{\mathbf{v}}, \mathbf{v}, \delta) = \mathbf{F}(\dot{\mathbf{v}}, \mathbf{v}) + \mathbf{F}(\mathbf{v}, \delta) \tag{4.1}$$

The influence of the acceleration on the hydrodynamic forces can be better seen if we assume an ideal fluid—inviscid fluid and irrotational flow—in which forces depending on velocity are zero. When a rigid body is accelerated in an ideal fluid, forces proportional to acceleration appear, the proportionality coefficients being the so-called added mass coefficients.

Imlay (1961) presented the complete expressions of the forces of a rigid-body accelerating in any way in an ideal fluid. These forces are expressed in terms of the 21 added masses, which is the maximum number that are independent for a Cartesian set of body axes. Imlay's expression included the so-called Munk moments. These moments are no longer used because in real flows they are intrinsically coupled to the viscous forces and it is not possible to separate them. Therefore, the Munk moments were dropped from the expressions. Considering, three degrees of freedom and ship symmetry, only four independent added masses are needed ($X_{\dot{u}}$, $Y_{\dot{v}}$, $N_{\dot{r}}$, and $Y_{\dot{r}} = N_{\dot{v}}$). The forces acting on the body are calculated as follows:

$$F_x = X_{\dot{u}}\dot{u} - Y_{\dot{v}}vr - Y_{\dot{r}}r^2 + X(u, v, r, \delta) \tag{4.2}$$

$$F_y = Y_{\dot{v}}\dot{v} + Y_{\dot{r}}\dot{r} + X_{\dot{u}}ur + Y(u, v, r, \delta) \tag{4.3}$$

$$M_z = N_{\dot{v}}\dot{v} + N_{\dot{r}}\dot{r} + N_{\dot{v}}ur + N(u, v, r, \delta) \tag{4.4}$$

Where X, Y, and N are the forces and moment acting on the ship, excluding the added mass components. These forces are modelled using an Abkowitz-type model and depend only on the ship velocities and rudder deflection. Their mathematical expressions read:

$$\begin{aligned} X =& X_u\Delta u + X_{uu}\Delta u^2 + X_{vv}v^2 + X_{rr}r^2 + X_{\delta\delta}\delta^2 \\ &+ X_{vr}vr + X_{vvrr}v^2r^2 + X_{vvvv}v^4 + X_{\delta\delta\delta\delta}\delta^4 + X_{u\delta\delta}\Delta u\delta^2 \end{aligned} \tag{4.5}$$

$$\begin{aligned} Y =& Y_0 + Y_v v + Y_r r + Y_\delta\delta + Y_{vvv}v^3 + Y_{rrr}r^3 + Y_{\delta\delta\delta}\delta^3 \\ &+ Y_{vvr}v^2r + Y_{vrr}vr^2 + Y_{u\delta}\Delta u\delta + Y_{u\delta\delta\delta}\Delta u\delta^3 \end{aligned} \tag{4.6}$$

$$\begin{aligned} N =& N_0 + N_v v + N_r r + N_\delta\delta + N_{vvv}v^3 + N_{rrr}r^3 + N_{\delta\delta\delta}\delta^3 \\ &+ N_{vvr}v^2r + N_{vrr}vr^2 + N_{u\delta}\Delta u\delta + N_{u\delta\delta\delta}\Delta u\delta^3 \end{aligned} \tag{4.7}$$

The higher order terms were introduced to model the forces in shallow water conditions. Reports from model tests show that longitudinal forces change sign from negative to positive in very shallow water. The term X_{vvvv} was therefore added to capture this behaviour. Similar reasoning was used for the other higher order coefficients. If such nonlinear behaviour is not present in the calculated forces, the regression analysis returns zero values for these coefficients.

It should be noted that the model is only valid for a range close to the equilibrium condition for which the coefficients were derived. Physically, this means that the hydrodynamic flow around the ship is close to that used to determine the hydrodynamic coefficients. In practical terms, this means that the ship's speed is at least 40% of the reference speed. If velocities fall below this range, errors start to arise. Another limitation is that in Abkowitz-type models the propeller rotation rate cannot be changed. If a different rotation rate is required, a new set of coefficients must be determined.

4.1.2 Numerical captive tests

Two different types of calculations are required to obtain the hydrodynamic coefficients. One for the added mass coefficients and another for the viscous related coefficients. A new method, described in detail in the following section, is used to calculate the added mass coefficients. This method uses an impulsive acceleration and as a result gives the zero frequency added masses. Table 4.1 lists the impulsive tests required to obtain the added mass coefficients.

For the viscous related coefficients, seven sets of numerically calculated captive tests are required to obtain all the hydrodynamic coefficients of the mathematical manoeuvring model: propulsion tests, rudder tests, drift tests, rotating tests, coupled rotation with drift tests, coupled drift with rudder tests, and coupled rotation with rudder tests. Table 4.2 lists the corresponding parameters used for these calculations and the associated state variables.

Table 4.1: Required impulsive tests to obtain added mass coefficients

	Type of captive test	Kinematic parameters	Related variables
1	Impulsive surge motion	$\dot{u}$	$X_{\dot{u}}$
2	Impulsive sway motion	$\dot{v}$	$Y_{\dot{v}}, N_{\dot{v}}$
3	Impulsive yaw motion	$\dot{r}$	$Y_{\dot{r}}, N_{\dot{r}}$

Table 4.2: Required captive tests to obtain hydrodynamic manoeuvring coefficients

	Type of captive test	Kinematic parameters	Related variables
1	Propulsion	$u/U_0 = 0.4 : 0.2 : 1.1$ rpm constant for U_0	$X = f(u)$
2	Rudder	$\delta = -50° : 10° : 50°$ $u/U_0 = 0.6, 1.0$	$X, Y, N = f(u, \delta)$
3	Drift	$\beta = -20° : 5° : 20°$ $u/U_0 = 0.6, 1.0$	$X, Y, N = f(u, v)$
4	Rotatory arm	$r' = -0.5 : 0.1 : 0.5$	$X, Y, N = f(r)$
5	Rotation with drift	$\beta = -2°, -5°, -8°, -12°$ $r' = 0.1 : 0.1 : 0.5$	$X, Y, N = f(v, r)$
6	Drift with rudder	$\beta = 0°, \pm 10°, \pm 20°$ $\delta = 0° : \pm 10° : \pm 40°$	$X, Y, N = f(v, \delta)$
7	Rotation with rudder	$r' = 0, \pm 0.2, \pm 0.4$ $\delta = 0° : \pm 10° : \pm 40°$	$X, Y, N = f(r, \delta)$

4.2 Test cases

The manoeuvring simulations were carried out with two representative ships. The Duisburg test case (DTC) containership (el Moctar, Shigunov, et al. 2012) and the reference inland waterway (RIW) ship test case (Mucha, el Moctar, et al. 2017), which is a general-purpose cargo vessel typically sailing on the Rhine River.

Table 4.3 lists their principal particulars. Figure 4.1 shows the hull geometry of the DTC, and Figure 4.2 the hull geometry of the RIW. As full-scale counterparts do not exist, they represent reference ships for benchmarking numerical studies and for clarifying flow physics. The associated model scale ratio λ corresponds to model tests carried out at the Norwegian Marine Technology Research Institute (MARINTEK) and the Maritime Research Institute Netherlands (MARIN), for DTC and RIW, respectively.

Table 4.3: Principal particulars of the DTC containership and the RIW ship

Principal particulars	Symbol	Units	DTC ship	model	RIW ship	model
Scale	λ	-	1.0	63.65	1.0	16.0
Length between perp.	L_{pp}	m	355	5.58	135.0	8.4375
Breadth	B	m	51	0.80	11.45	0.7150
Draft	T	m	14.5	0.2278	3.5	0.2188
Block coefficient	Cb	-	0.66	0.66	0.92	0.92
Displacement	Δ	t,m3	173468	0.6726	4992	1.2187
Wetted surface	Sw	m	22032	54.38	2376.1	9.2817
Longitudinal COG	LCG	m	174.1	2.721	-0.1718	-0.01074
Vertical COG	VCG	m	19.8	0.312	2.04	0.1275
Metacentric height	GMt	m	5.1	0.080	2.4	0.15
Mass	M	kg	-	672.7	-	1216.9
Inertia radius y	r_{xx}	m	20.3	0.339	0.4B	0.286
Inertia radius x	r_{yy}	m	87.3	1.371	$0.25Lpp$	2.1094
Inertia radius z	r_{zz}	m	87.4	1.387	$0.25Lpp$	2.1094
Reference speed	U_0	m/s		0.387		0.556
Water density	ρ	kg/m^3		1000		1000

Figure 4.1: The Duisburg test case (DTC) containership

Figure 4.2: The reference inland waterway (RIW) ship

At first glance, the hull geometry of inland waterway ships appears simpler than that of a seagoing ships. This impression changes when the focus is on the stern of the ship. Complex stern geometries are common on inland waterway ships, mainly due to the

space constraints of the propulsion system. A typical inland waterway ship has tunnels in front of the propeller to improve inflow, a ducted propeller and a twin-rudder behind the propeller. Figure 4.3 shows the stern of both ships, the DTC and the RIW.

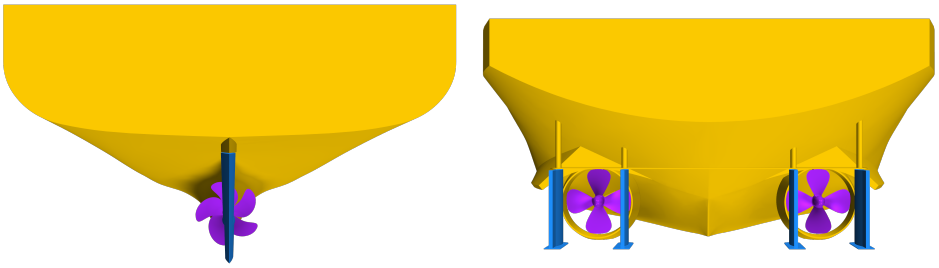

Figure 4.3: Stern view of the DTC containership (left) and the RIW ship (right)

4.3 Added mass at zero frequency in deep and shallow water

Manoeuvring simulations using mathematical models require the added mass coefficients at zero frequency. To date, these coefficients have been calculated using potential flow theory or unsteady RANS, replicating the planar motion mechanism (PMM) model tests. From the theoretical point of view, the latter approach always gives frequency dependent coefficients. Potential theory, in particular the three dimensional panel methods, is able to compute added mass coefficients with frequency close to zero ($\omega = 0.04\,\mathrm{rad/s}$), but its convergence is difficult, even in deep water conditions. This is particularly true for the coupling terms.

The above problem motivated the development of the present method, which computes the added mass coefficients for zero frequency. The method is robust in deep and shallow water and the computation is fast.

4.3.1 Method procedure

The added mass problem is solved with the Euler equation using the finite volume method. The numerical domain discretization is similar to that used for RANS calculations. However, coarse control volumes can be used as there is no boundary layer or turbulence in an inviscid flow.

1. Ship with zero forward speed

   For a ship starting its motion from zero speed, the hull is impulsively accelerated from zero to a given speed within a single time step (see Figure 4.4). This means

that the entire domain is moved within one time step without deforming the control volumes. As the Euler equations are solved, the speed-dependent forces and moments are zero, i.e., the forces and moments acting on the hull depend only on the acceleration. When the calculation has reached convergence for each acceleration mode, the added masses are obtained as follows:

$$\text{surge acceleration:} \qquad X_{\dot{u}} = \frac{F_x}{\dot{u}} \tag{4.8}$$

$$\text{sway acceleration:} \qquad Y_{\dot{v}} = \frac{F_y}{\dot{v}} \qquad N_{\dot{v}} = \frac{M_z}{\dot{v}} \tag{4.9}$$

$$\text{yaw acceleration:} \qquad N_{\dot{r}} = \frac{M_z}{\dot{r}} \qquad Y_{\dot{r}} = \frac{F_y}{\dot{r}} \tag{4.10}$$

Where $X_{\dot{u}}$ is the surge added mass, $Y_{\dot{v}}$ the sway added mass, $N_{\dot{r}}$ the yaw added moment of inertia. $N_{\dot{v}}$ and $Y_{\dot{r}}$ are the coupled added mass terms, F_x the hydrodynamic surge force, F_y the hydrodynamic sway force, M_z the hydrodynamic yaw moment, $\dot{u}$ the surge acceleration, $\dot{v}$ the sway acceleration, $\dot{r}$ the yaw angular acceleration. Due to the impulsive acceleration of the hull, the hydrodynamic forces and moments acting on the hull are calculated at zero frequency, as required for manoeuvring simulations.

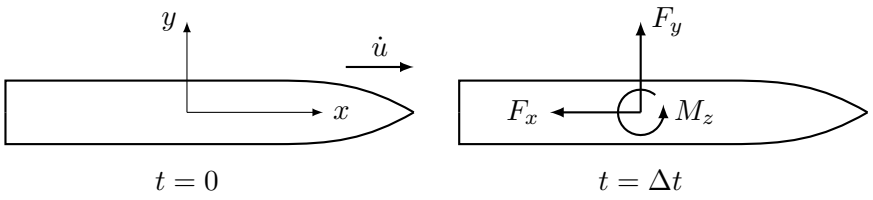

Figure 4.4: Surge impulsive acceleration over one time step and measured forces and moment

To ensure convergence of the numerical solution, the normalized residuals of the flow variables need to be reduced by several orders of magnitude. This requires several outer iterations within the time step. Since this simulation over one-time step for a numerical grid consisting of several million control volumes takes only a few minutes on a common workstation, the method proves to be computationally efficient.

2. Ship with forward speed

   To calculate the added masses by taking into account the forward speed of the ship, the method consisted of two steps. First, I determined the steady state flow around the advancing ship. This took little time as the flow had to reach a steady state

condition. The flow calculated in this way was then used as a starting solution for the accelerated flow around the hull to be calculated afterwards. The validity of the method was tested at slow forward speeds, $F_n < 0.1$, in order to use the double-body approach. Under this condition, it was found that the forward speed only affects the added moment of inertia $N_{\dot{r}}$ within one percent. The first step was therefore unnecessary. A similar conclusion can be reached by analysing the formulations of the added mass coefficients based on potential theory. For a given forward speed, the added mass coefficient is related to the added mass at zero-speed as follows:

$$A_{11}^U = A_{11}^0 \tag{4.11}$$

$$A_{22}^U = A_{22}^0 \tag{4.12}$$

$$A_{26}^U = A_{26}^0 + \frac{U}{\omega^2} B_{22}^0 \tag{4.13}$$

$$A_{62}^U = A_{62}^0 - \frac{U}{\omega^2} B_{22}^0 \tag{4.14}$$

$$A_{66}^U = A_{66}^0 + \frac{U^2}{\omega^2} A_{22}^0 \tag{4.15}$$

where symbols A_{jk} are the added mass in j-mode due to acceleration in the k-mode, and B_{jk} the potential damping ($j, k = 1, 2, 6$ are surge, sway and yaw, respectively). Symbol U is the ship forward speed and ω is the frequency of oscillation. From these equations, the forward speed only affects the added moment of inertia A_{66}, because at zero frequency the potential damping is zero. Therefore, the added masses calculated for zero speed are a good approximation even for cases where the forward speed is not zero.

3. Normalized added mass

I normalized the computed added masses coefficients against physical mass, moment of inertia and ship length between perpendiculars:

$$A_{11} = \frac{X_{\dot{u}}}{m}, \quad A_{22} = \frac{Y_{\dot{v}}}{m}, \quad A_{66} = \frac{N_{\dot{r}}}{I_{zz}}, \quad A_{26} = \frac{N_{\dot{v}} L_{pp}}{I_{zz}}, \quad A_{62} = \frac{Y_{\dot{r}} L_{pp}}{I_{zz}} \tag{4.16}$$

Where A_{11} is the non-dimensional surge added mass, A_{22} the non-dimensional sway added mass, A_{66} the non-dimensional added moment of inertia, m the physical ship mass, I_{zz} the physical moment of inertia about the z-axis, and L_{pp} the length between perpendiculars.

4.3.2 Validation with the ellipsoid

To validate the computations, the surge and sway added mass as well as the added moment of inertia of a fully submerged ellipsoid in infinite water were computed. Figure 4.5 shows the geometry and presents its dimension and mass properties. The grid consisted of 2.2 million control volumes, see Figure 4.6.

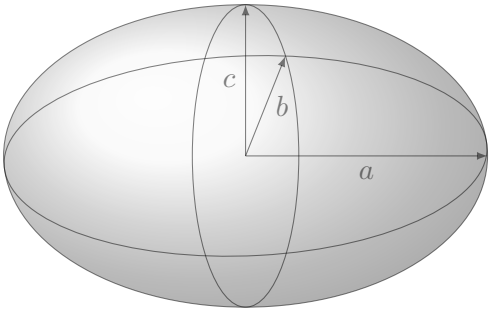

$a = 3.0\,\mathrm{m}$
$b = 1.5\,\mathrm{m}$
$c = 1.5\,\mathrm{m}$

$M = 28\,274.30\,\mathrm{kg}$
$I_{zz} = 63\,617.25\,\mathrm{kg\,m^2}$

Figure 4.5: Geometry of investigated Ellipsoid with half-axes a, b, and c, mass M and moment of inertia about the vertical axis I_{zz}

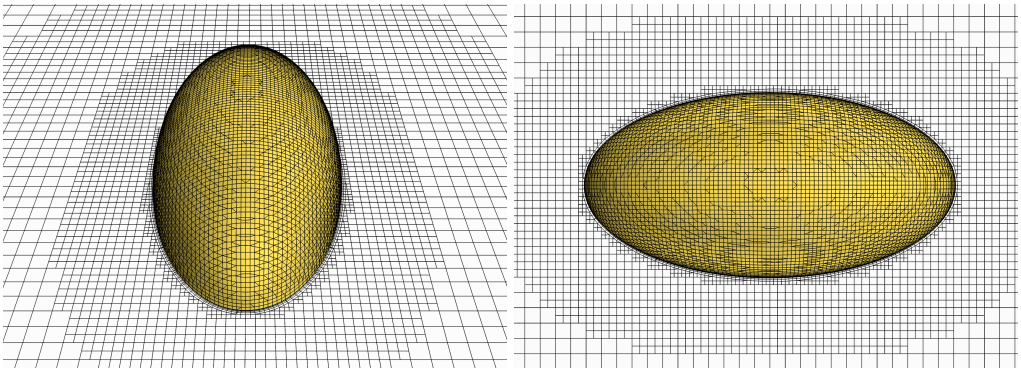

Figure 4.6: Top and frontal view of the Ellipsoid mesh topology

Figure 4.7 shows the longitudinal velocity and pressure field due to a surge acceleration. The direction of acceleration is to the right and the force is in the opposite direction. In the longitudinal axis the pressure gradient has the same direction as the acceleration, high at the bow and low at the stern. However, the force direction is always the negative of the pressure gradient, which means that the longitudinal force direction is opposite to the acceleration.

Korotkin (2009) provided the analytical values of the added mass and the added moment of inertia in the case of the motion of an ellipsoid in infinite ideal fluid, Fig. 4.5. The non-

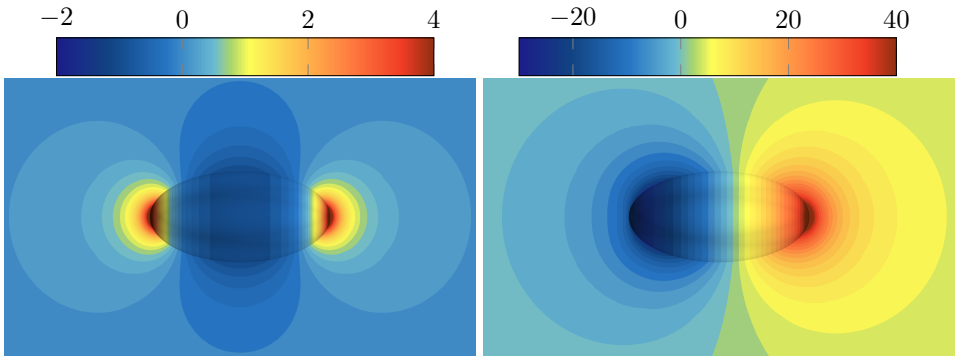

Figure 4.7: Longitudinal speed and pressure due to a surge acceleration of the Ellipsoid

dimensional added masses of a three-axial ellipsoid with half-axes a, b, and c are given by

$$A_{11} = \frac{A_0}{2 - A_0}$$
$$A_{22} = \frac{B_0}{2 - B_0}$$
$$A_{66} = \frac{(a^2 - b^2)^2 (B_0 - A_0)}{[2(a^2 - b^2) + (A_0 - B_0)(a^2 + b^2)](a^2 + b^2)}$$

where

$$A_0 = abc \int_0^\infty \frac{du}{(a^2 + u)\sqrt{(a^2 + u)(b^2 + u)(c^2 + u)}}$$
$$B_0 = abc \int_0^\infty \frac{du}{(b^2 + u)\sqrt{(a^2 + u)(b^2 + u)(c^2 + u)}}$$

Table 4.4 lists comparative analytical and computed values of non-dimensional surge added mass A_{11}, sway added mass A_{22}, and added moment of inertia A_{66} together with the percentage deviations between the analytical and the extrapolated values. The numerical results correlate well with the analytical solution. The computed surge added mass deviated by 1.02 % from the analytical solution, the sway added mass by 0.43 % and the added moment of inertia by 1.09 %.

Table 4.4: Analytical and computed non-dimensional surge added mass (A_{11}), sway added mass (A_{22}), added moment of inertia (A_{66}) and their deviations for the Ellipsoid. The deviation is computed as the difference between the analytical solution and the extrapolated value.

Added mass	Analytical	Grid 3	Grid 2	Grid 1	Extrapolated	Deviation
Surge: A_{11}	0.210015	0.21175	0.21200	0.21209	0.21215	−1.02 %
Sway: A_{22}	0.704210	0.70661	0.70702	0.70717	0.70724	−0.43 %
Yaw: A_{66}	0.239424	0.24132	0.24132	0.24182	0.24204	−1.09 %

4.3.3 Validation with the DTC containership

The added masses of the DTC containership calculated by the Euler method are compared with the added masses obtained from a boundary element method (BEM). The calculations were performed with a Froude number $F_n = 0.05$ (6 knots full scale). The BEM was calculated for a range of frequencies from $\omega = 0.04\,\text{rad/s}$ to $\omega = 8\,\text{rad/s}$ and the zero frequency added masses were obtained by extrapolation. Figure 4.8 shows the DTC added masses calculated by these two methods.

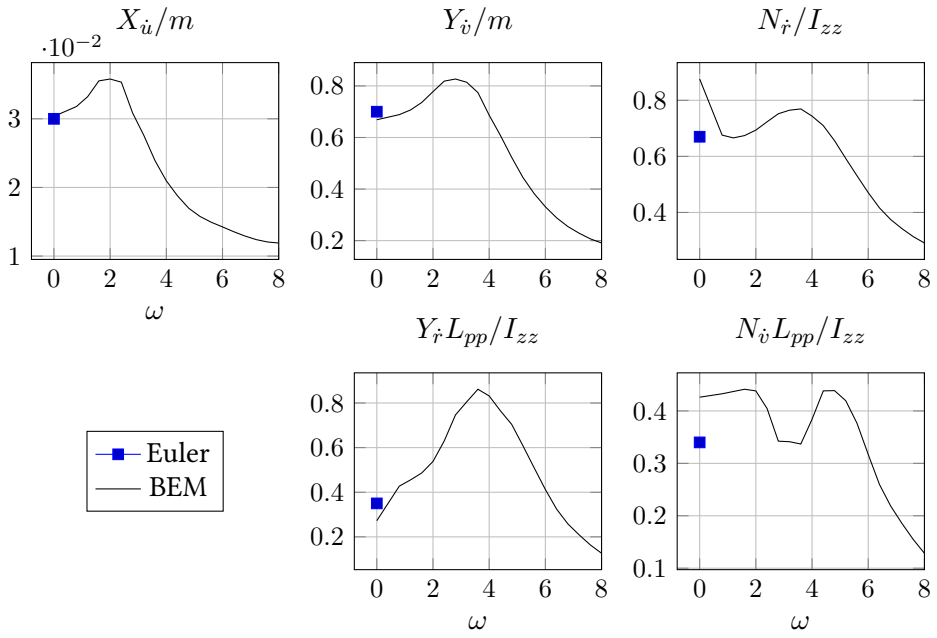

Figure 4.8: DTC non-dimensional added mass coefficients for $F_n = 0.05$. Computations were made with two methods: the presented Euler method and a boundary element method (BEM)

As seen in Fig. 4.8, the surge and sway added masses calculated by the Euler and BEM methods correlate well. Small deviations are observed in the BEM yaw added moment

of inertia due to difficulties of numerical convergence at small frequencies. Table 4.5 lists the zero frequency added mass values calculated by the Euler and BEM methods. The Timman-Newman relation (Newman 2018; Timman and Newman 1963) states that $Y_{\dot{r}} = N_{\dot{v}}$, which is true for cases where the ship has zero speed. However, for a ship with forward speed, the Timman-Newman relation does not hold, but the magnitudes of the added masses are still close to each other for the Euler method, as shown in Table 4.5.

Table 4.5: DTC added mass at zero frequency for $F_n = 0.05$

Added Mass	EULER	BEM
A_{11}	0.03	0.03
A_{22}	0.70	0.67
A_{26}	0.34	0.43
A_{62}	0.35	0.27
A_{66}	0.67	0.88

4.3.4 Shallow water effects on added mass

Figure 4.9 shows the dimensionless added mass coefficients of the DTC containership and the RIW ship. The general effect of decreasing water depth is to increase the magnitude of the added mass coefficients. For instance, in deep water the DTC containership sway added mass is about 70% of the ship's mass, but at the $h/T = 1.2$ this value increases to 240% of the ship's mass.

The difference in hull geometry is also reflected in the added mass coefficients. The DTC containership has a block coefficient of $C_b = 0.66$ while the RIW ship has $C_b = 0.92$. Bulky ships with high block coefficients have a higher moment of inertia about the z-axis and therefore a higher added mass moment of inertia than their counterparts with low coefficients. The midsection area of the RIW ship is extended over almost 80% of the ship's length, so the geometrical differences are only at the bow and stern, covering the remaining 20%. This is the reason why the coupled added mass $N_{\dot{v}}$ is small for the RIW ship. For hull geometries with bow and stern symmetry this coefficient will be zero.

4.4 Efficient direct system identification

Currently, RANS-based simulations are widely used to reproduce captive model tests and to obtain hydrodynamic manoeuvring coefficients. However, their use for inland waterway ships in shallow water condition presents some difficulties. First, due to the complexity of their stern geometry, which usually includes a ducted propeller with twin-rudders.

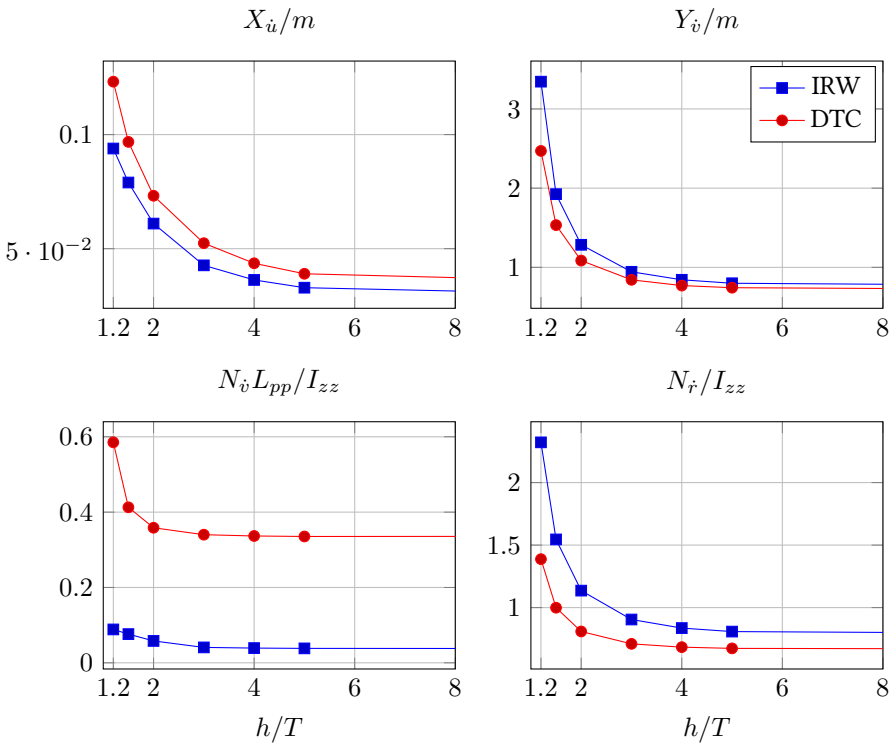

Figure 4.9: Added mass coefficients of the IRW and DTC ships dependency on water depth h/T

Second, due to the shallow water constraints that affect the ship modelling motions. Here, I present a method to accurately compute the manoeuvring captive tests of fully-appended ships in shallow water conditions. The procedure is general and can be applied to any type of ship.

The method was validated step by step. First, the forces on the bare hull DTC containership were calculated at two water depths: $h/T = 1.2$ and $h/T = 2.0$ and compared with model test measurements. Then, the forces on the RIW ship, fully appended, were compared with the available measurements.

4.4.1 Numerical domain and grid

Figure 4.10 shows a top view of one-half of the specified numerical fluid domain. As seen, the side boundaries are placed $2.5L_{pp}$ away from the ship's symmetry plane; the inlet boundary, $2.5L_{pp}$ from amidship; and the outlet boundary, $3.0L_{pp}$ from amidship. The top boundary was placed $0.5L_{pp}$ away from the free surface and the bottom of the domain corresponded to the desired water depth. For validation with captive model tests, the sides of the numerical domain were reduced to match the width of the towing tank.

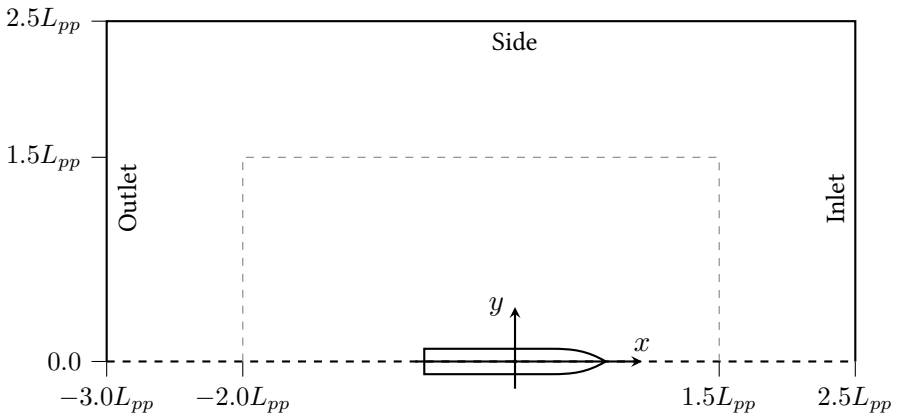

Figure 4.10: Top view of one-half of the numerical fluid domain.

The numerical domain was divided in two regions that are connected by a sliding interface. One region contains the propeller and the other contains all remaining surfaces, such as the hull, rudder, duct, and other fixed appendages to the hull. For ships with two propellers, an additional region enclosing the second propeller was added.

Small control volumes discretized the numerical domain. For the propeller-regions an unstructured grid was generated using polyhedral control volumes. The volume of the cells grow smoothly from the propeller surface to the boundaries of the propeller region, see Figure 4.11. Locally, the grid was refined at the leading edge, trailing edge, and hub of the propeller. For the hull-region an unstructured grid was generated using hexahedral control volumes, see Figure 4.12. The grid was locally refined near the bow, near the stern, and between the hull underside and the domain's bottom boundary to properly capture the complex flow features around the ship's hull. The grid was also refined at the free surface and in the ship's wake. Figure 4.13 shows an example of grid refinement in the region of the ducted propeller.

To model the inner region of the boundary layer, I used the so-called all y^+ wall treatment, which emulates the low or the high y^+ value treatment depending on the size of the cells near the wall. Therefore, the grid typically contained eight or more prism layers near the hull to model the boundary layer, and a y^+ around the unity was aimed for.

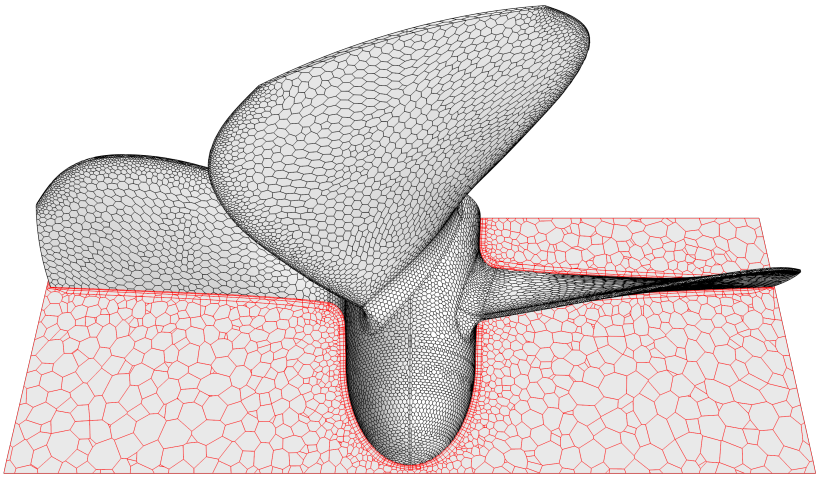

Figure 4.11: Numerical discretization example of the propeller

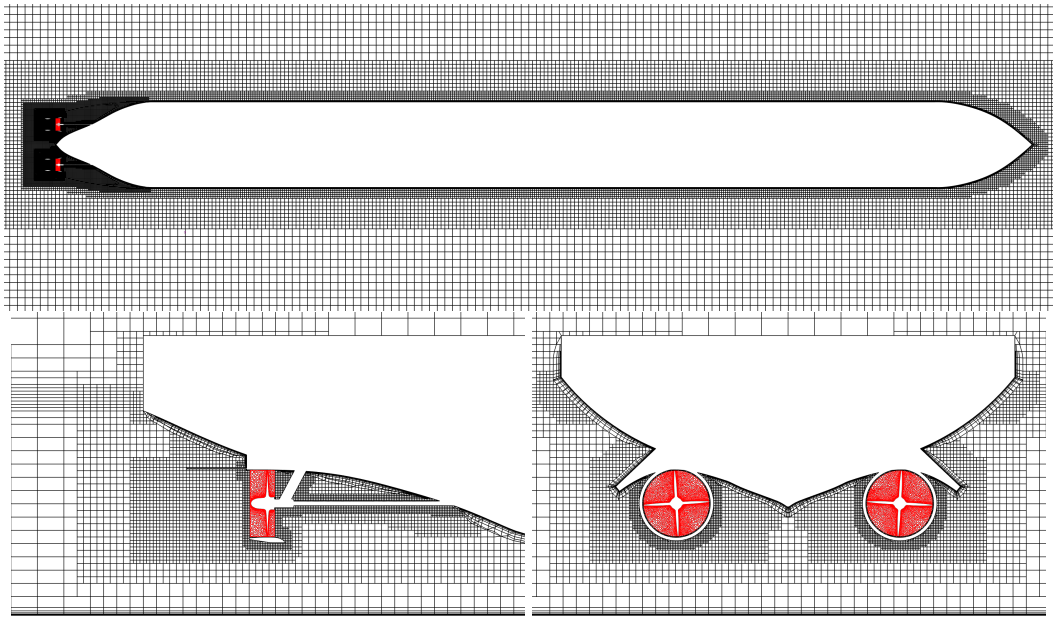

Figure 4.12: Numerical discretization example of the hull-region (black lines) and propeller regions (red lines)

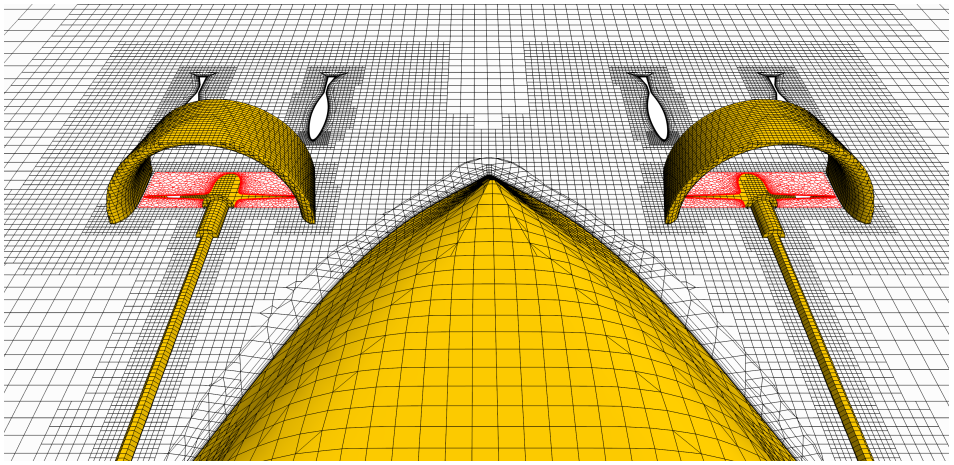

Figure 4.13: Grid refinement in the region of the ducted propeller and the twin-rudders

4.4.2 Numerical setup

The captive tests were solved in the auxiliary coordinate system, which is fixed to the ship but does not heave or pitch. This coordinate system coincides with the body-fixed coordinate system at the start of the simulation and is the same when the ship's heave and pitch are zero. The use of the auxiliary coordinate system allows to fix the ship horizontally and to consider the fluid as moving at the relative velocity between the ship and the fluid. Therefore, all flow properties, including boundary conditions, were defined with respect to the auxiliary coordinate system.

1. Boundary conditions

   The sides of the computational domain were considered as slip-walls. The relative velocity was prescribed at the inlet boundary. The hydrostatic pressure determined the pressure at the outlet boundary. At the top of the domain, the inlet condition was specified and, thus, the relative velocity was prescribed. The bottom of the domain was considered as a non-slip wall moving with the relative velocity. Finally, the hull surface was considered as a non-slip wall. To prevent wave reflection from boundaries, the volume of fluid wave-damping method dampened the waves in areas approaching the inlet, outlet, and side boundaries. The areas between the dashed lines and the numerical domain boundaries in Fig. 4.10 mark these areas, extending a length over $1.0L_{pp}$ beyond their boundaries.

   When considering the wall of the towing tank in the simulation, the wall was treated as a non-slip wall moving with the relative velocity, similar to the bottom. In addition, wave damping was disable at these boundaries.

2. Motions

   The dynamic motion of the ship, sinkage and trim, and the rotation of the propeller are all taken into account during the simulation. A mesh morphing algorithm with a rigid motion solver deforms the numerical grid to allow the ship to heave and pitch. Propeller rotation is modelled using the moving reference frame (MRF) approach. This modelling approach does not change the position of the control volumes, but rather converts the transient problem to a steady state problem in a moving reference frame that rotates at the same rate as the propeller. The solution produces a time-averaged flow characteristic. The use of this approach is justified, first, because the desired solution is steady state. Second, it allows to use a relatively large time step compared to a simulation including geometric rotation of the propeller. Note that when simulating propeller rotation, the recommended time step is chosen so that the propeller does not rotate more than 5° per time step. For example, if a propeller rotates at 10.5 revolutions per second, then a time step of two milliseconds should be used, but using the reference frame approach a time step five times higher can be used.

3. Solver setup

   The numerical calculations involving the free surface were solved using the unsteady RANS solver for 200 s with a time step of $\Delta t = 0.01$ s. The equations were solved sequentially using the segregated flow approach with 8 inner iterations for each time step. Second order temporal and spatial discretization were used. For the steady RANS solver, a total of 4000 iterations were used to ensure convergence of the double-body calculations. If the steady-state simulation fails to convergence, forces show oscillatory behaviour. The steady-state simulation is then switched to unsteady simulation with a time step of $\Delta t = 0.01$ s. To speed up convergence, the steady solution is used as the initial condition of the unsteady simulation.

4.4.3 Numerical techniques to improve computation efficiency

Two numerical techniques are proposed to improve the convergence of the calculations and increase their efficiency, while maintaining the same accuracy. The first technique aims at improving the initial condition, and shows its effectiveness particularly in small confined spaces. The second technique takes advantage of the fact that many manoeuvres in shallow water are performed at low speed, then simplifications are proposed in the treatment of the free surface and sinkage.

1. Improving initial condition

When using RANS to reproduce towing tank captive model tests, a common approach is to solve the problem in the body-fixed coordinate system. This means that the ship does not move and the fluid far from the ship flows at the relative velocity—equal to the towing velocity but in the opposite direction. The numerical domain is then initialized with the relative velocity and hydrostatic pressure. At the start of the simulation, large waves are generated in the bow and stern regions and propagate through the numerical domain. These waves are caused by the incorrect initialization conditions, but with a sufficiently large numerical domain and damping methods their effects are reduced in the first quarter of the simulation time. However, when the walls of the towing tank are included in the simulation, these waves can remain in the simulation for a long time due to wave reflecting on the walls, making it difficult to achieve convergence.

To avoid the initial creation of large waves, I set the initial inflow velocity to zero and apply a horizontal gravitational acceleration in the direction of the flow within the first 20 seconds. This horizontal gravitational acceleration smoothly accelerates the flow from zero up to the desired speed U_0. Figure 4.14 shows the mathematical expression of the artificial horizontal gravity g_x and the inflow velocity v_x during the ramp time period. As seen, the acceleration is constant during the ramp time period (20 s), and becomes zero when the desired velocity is reached.

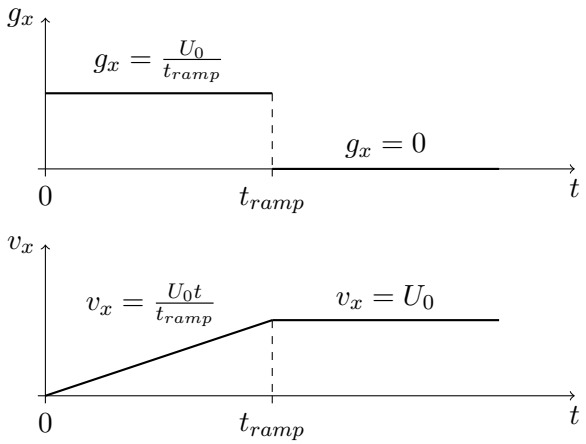

Figure 4.14: Artificial horizontal gravity and inflow velocity

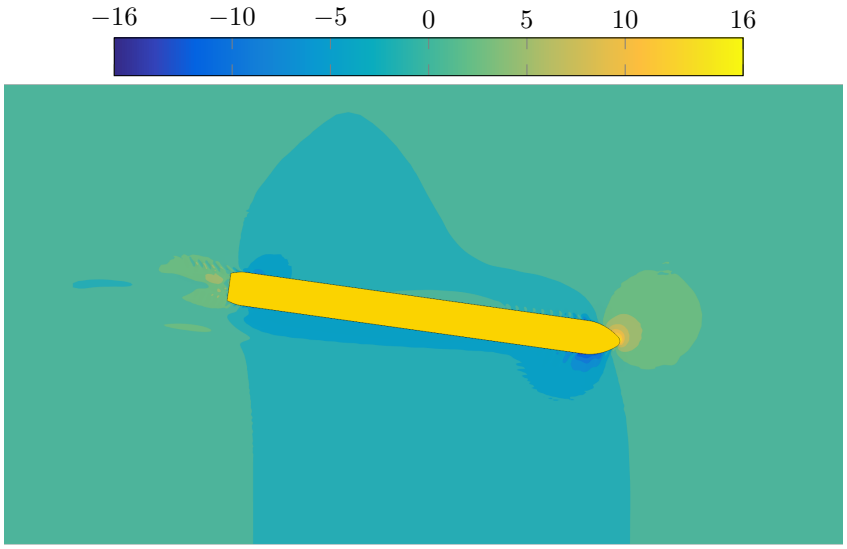

(a) $\beta = 8^{\circ}$

(b) $\beta = 12^{\circ}$

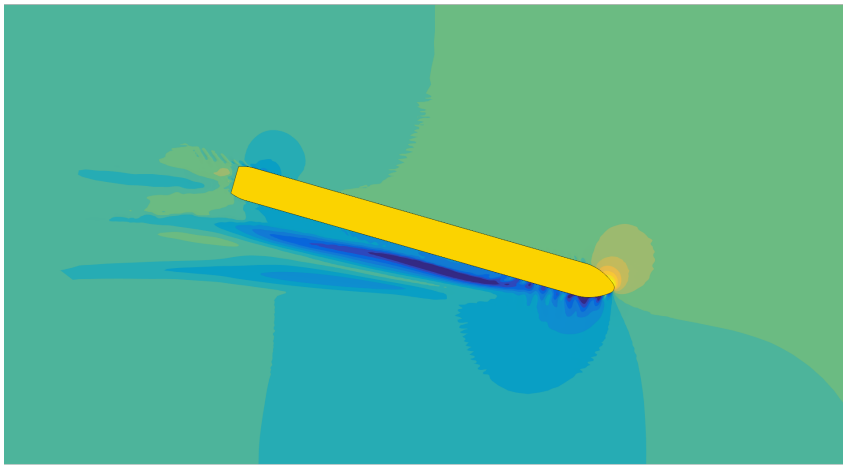

(c) $\beta = 16^{\circ}$

Figure 4.15: Wave elevation (mm) of the RIW ship in captive drift test

The method was tested on captive drift tests of the RIW ship at $h/T = 1.5$. The numerical domain has the same width as the towing tank. Figure 4.15 shows the free surface elevation at the end of the simulation for three drift angles. The lateral sides of the figures coincide with the walls of the towing tank. As seen, the free surface elevation has been correctly resolved. Figure 4.16 shows the evolution of the sway force during the captive drift test $\beta = 16°$. During the first 20 s when the horizontal gravity was active, the magnitude of the force increased almost linearly. By the 80 s simulation time point, the sinkage had converged and the sway force also began to converge.

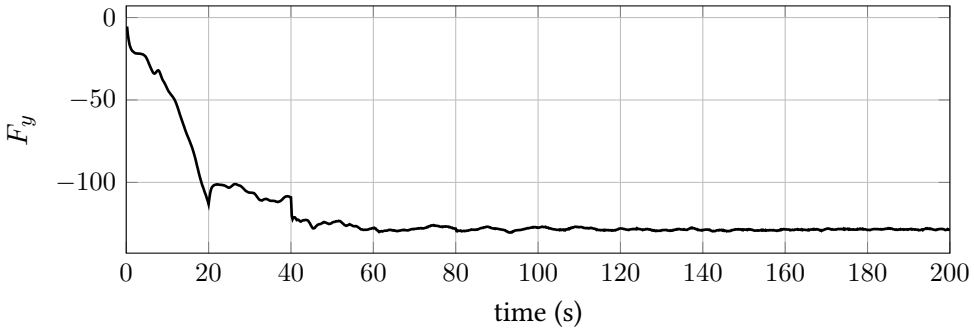

Figure 4.16: RIW ship sway force time record during captive drift test $\beta = 16°$

2. Double-body with sinkage for low speed

Manoeuvres in realistic environmental conditions are usually conducted at slow forward speeds. For instance, ships on the Rhine have an average speed below the Froude number $F_n < 0.1$. For low speed manoeuvres, the influence of the free surface is negligible, thus the numerical calculation can be performed by modelling only the water and considering the free surface as a symmetry plane. This approach is called double-body and it is regularly used for deep water, low speed manoeuvres. Its use in shallow water is questionable as it does not take into account the dynamic vertical motion of the ship. For inland waterway ships at low speeds, it has been found that the heave motion of the ship is more important than the trim, which is around 0.1° and can therefore be neglected. In order to account for sinkage in the double-body approach, I have developed an iterative re-meshing process algorithm. First, the simulation is run for about 500 iterations to obtain the vertical hydrodynamic force F_z acting on the ship. This force is used to solve equation (4.17), derived from the equilibrium heave equation, which gives the next vertical displacement. The ship is moved accordingly, re-meshed and run for another 500 iterations. The

process continues until the vertical displacement is less than a threshold value. For instance, a threshold of 0.5 mm was used for model scale calculations. This method speeds up the calculation by a factor of 20-25 times compared to the free surface method with the deforming mesh algorithm, which solves for sinkage and trim.

$$z_{n+1} = z_n + f_k \frac{F_z - Mg}{\rho g B L_{pp}} \tag{4.17}$$

where z_n is the heave motion in the current iteration, z_{n+1} is the heave motion in next iteration, the symbol f_k is an under-relaxation factor, the value of 0.8 gives a smooth convergence. F_z is the vertical hydrodynamic force acting on the ship, M is the mass of the ship, and g the acceleration of gravity.

Figure 4.17 shows a comparison of the surge force, sway force and yaw moment of the RIW ship during a captive rudder test at $h/T = 3.0$, carried out using the free surface approach (blue squares) and the double-body re-meshing approach (red circles). For this water depth the sinkage is small, less than 1 mm at model scale, and has no influence on the forces. Therefore, the forces are compared to show that the free surface can be simplified as a slip wall. As seen in Fig. 4.17, the values calculated with the double-body re-meshing approach are almost the same as those calculated with the free surface approach for all rudder angles δ.

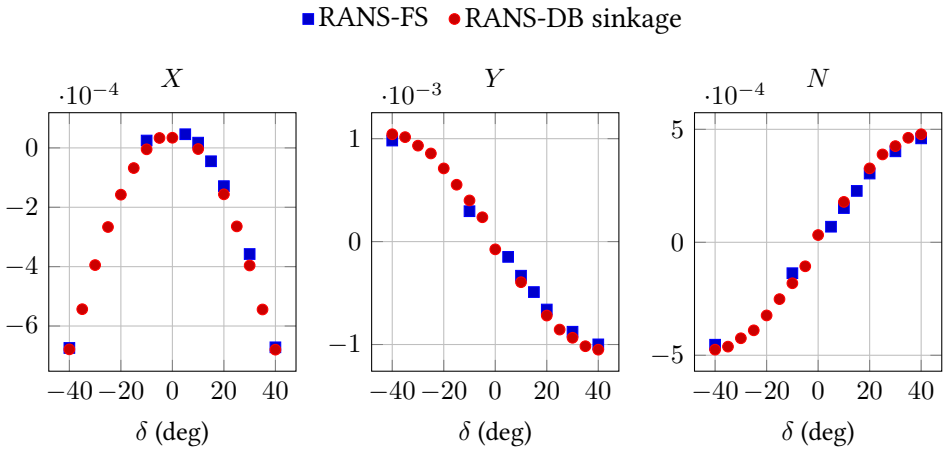

Figure 4.17: Captive rudder test of the RIW ship at $h/T = 3.0$ with two methods: free surface (FS) and double-body with sinkage (DB sinkage)

Figure 4.18 shows a comparison of the sway force, yaw moment and amidships sinkage of the RIW ship during a drift captive test at $h/T = 1.5$, performed using the double-body re-meshing and free surface approaches. For this water depth, the

sinkage is large enough to change the magnitude of the forces. As seen, the forces and moments are accurately calculated by the double-body re-meshing approach. For drift angles below 12°, there is a difference in amidship sinkage z_m of 0.3 mm, which is a value below the stopping criteria. For the largest drift angle of 20°, the double-body simulation predicts a sinkage only 0.7 mm higher than the free surface. This demonstrates the accuracy of the double-body re-meshing approach. Figure 4.19 shows an example of the flow velocity at the stern of the RIW ship during the simulation of a captive test.

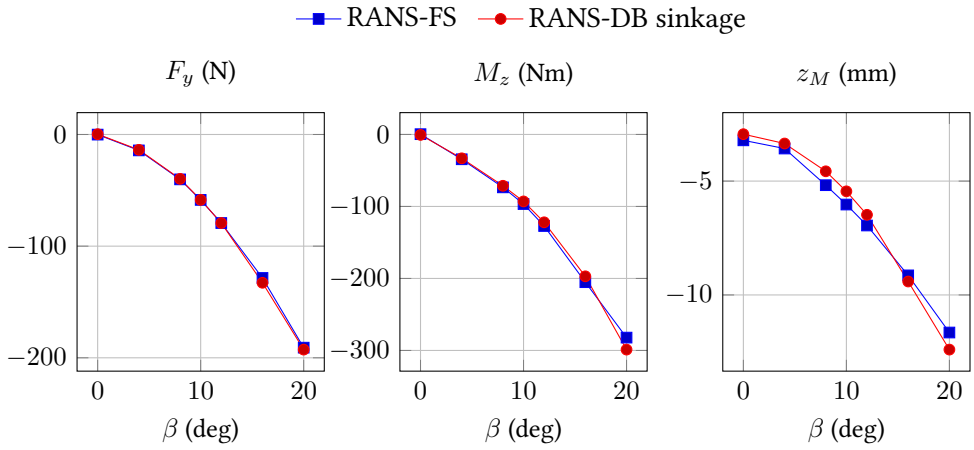

Figure 4.18: Captive drift test of the RIW ship at $h/T = 1.5$ with two methods: free surface (FS) and double-body with sinkage (DB sinkage)

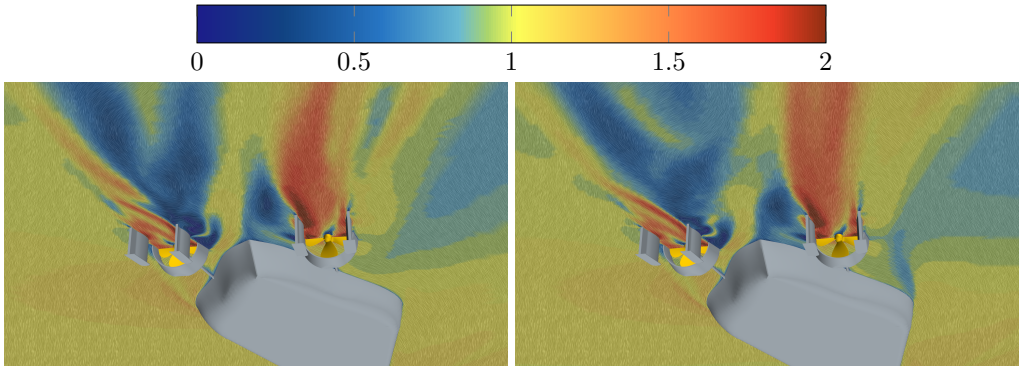

(a) Free Surface (b) Double-body sinkage

Figure 4.19: Nondimensional flow velocity magnitude $\mathbf{v}/U_0$ at the stern of the RIW ship during captive drift test with $\beta = 12°$

4.4.4 Validation of DTC containership forces

Experimental captive drift tests of the DTC containership in shallow water were carried out by Flanders Hydraulics (Zwijnsvoorde et al. 2015). These drift tests were performed at two water depths, $h/T = 2.0$ and $h/T = 1.2$, with a Froude number of $F_n = 0.05$, corresponding to a speed of 6 knots at full scale. The ship model was bare hull, hence only forces on the hull were measured. The validation of the RANS method was carried out by a direct comparison of the forces between the calculated and measured values.

1. Discretization study

   The discretization study of the DTC containership was performed at extreme shallow water, $h/T = 1.2$, and drift angle $\beta = 10°$. The calculations of the DTC containership were performed using steady RANS and following the approach of Oberhagemann and el Moctar (el Moctar, Schellin, et al. 2021) described in Section 3.1.6.

Table 4.6: Grid base size, number of control volumes (Ncells), refinement ratio (Υ), surge force (F_x), sway force (F_y) and yaw moment (M_z) obtained on the coarse, the medium, and the fine grid.

	base size (mm)	Ncells (10^6)	Υ (-)	F_x (N)	F_y (N)	M_z (N)
Coarse	180	1.24	1.0	-0.5736	14.4738	14.1341
Medium	90	6.03	0.5	-0.6290	13.7981	14.4489
Fine	45	40.85	0.25	-0.6708	13.686	14.6782
Extrapolated	-	-	0.0	-0.7220	13.7313	14.9553
EFD mean	-	-	0.0	-0.6341	14.6627	14.3564
EFD std	-	-	0.0	0.7318	0.7211	0.5697

Following the procedure of Oberhagemann and el Moctar (el Moctar, Schellin, et al. 2021), I performed simulation on three successively finer grids. Starting with the coarse grid, I selected the refinement factor of $r_x = 2.0$ to obtain a medium and fine grid. Table 4.6 lists the number of cells in each grid and the associated grid base size. It also lists the grid refinement ratio, Υ, determined from equation (3.26). A value of one represents the coarsest grid and a value of zero represents the grid independent solution. Table 4.6 also lists the surge force, sway force and yaw moment obtained for these three grids.

Figure 4.20 plots the forces and moments obtained during the grid discretization study. At $\Upsilon = 0$, the mean measured values are plotted with uncertainty bars corresponding to the standard deviation. The black squared symbol represent the extrapolated values obtained from the discretazation study. Each of the parameter

analysed present a monotonic convergence. As seen, the extrapolated surge forces almost match the mean measured value. The extrapolated sway force differs from the measured mean value in about 0.6 N. Similarly, the extrapolated yaw moment value differs in about 0.6 Nm.

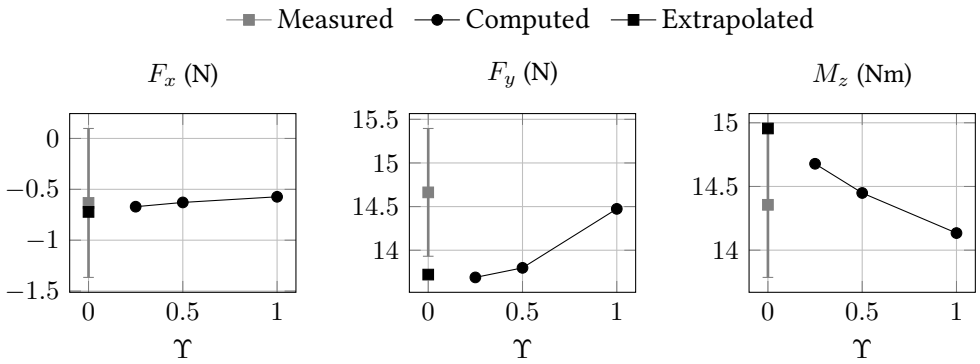

Figure 4.20: Forces and moments obtained during the grid discretization analysis

2. Force validation

Figure 4.21 plots the non-dimensional measured and computed surge force, sway force and yaw moment during the drift captive test at $h/T = 2.0$. The grey lines represent the measured values and the blue lines represent the computed values. The measured values were extracted from the force measurement time records. As these time records shows an unsteady oscillatory behaviour, two quantities were extracted, their mean value and their standard deviation. In Fig. 4.21, the squared symbols represent the mean values and the uncertainty bars represent the standard deviation of the experimental values. The RANS simulations were carried out with the double-body approach including sinkage and using the k-ω SST turbulence modelling. As seen, the computed forces and moments are in good correlation with the measured values.

Similar to Fig. 4.21, Figure 4.22 plots the forces and moments of the captive drift tests at water depth $h/T = 1.2$. Again, the computed forces and moments correlate well with the measured ones. This indicates the reliability of the method even in extreme shallow water conditions.

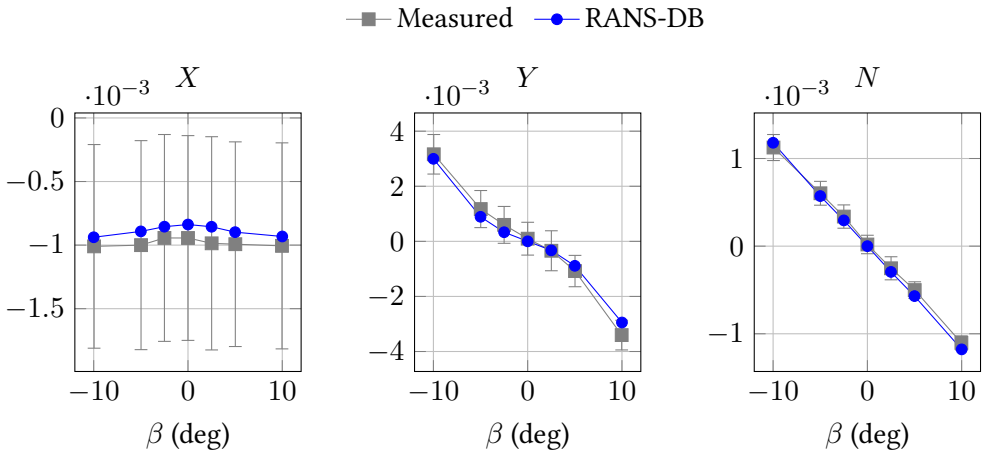

Figure 4.21: DTC containership surge force, sway force, and yaw moment during captive drift test at water depth ratio $h/T = 2$

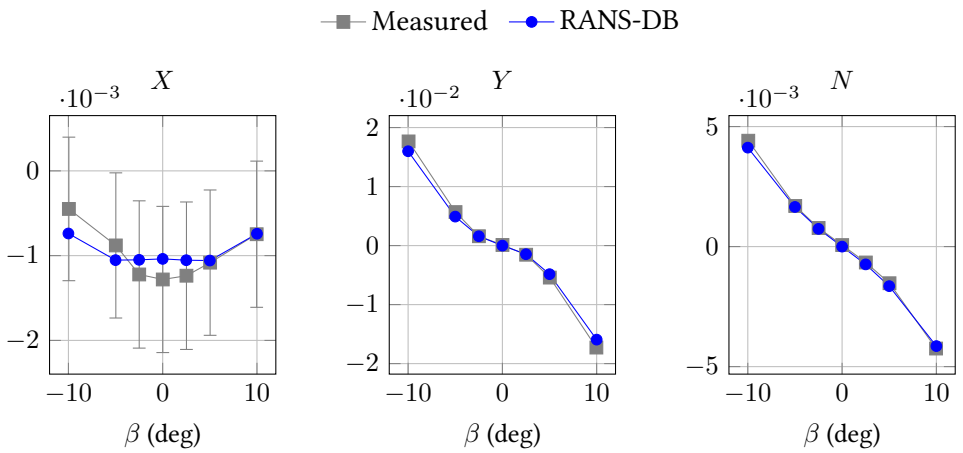

Figure 4.22: DTC containership surge force, sway force, and yaw moment during captive drift test at water depth ratio $h/T = 1.2$

During the captive drift tests, the longitudinal forces are small. Usually, the surge force is one magnitude smaller than the sway force, because ships are optimized to ensure a minimum resistance. This creates a disparity in the magnitudes to be measured during model test. Despite the impression of large standard deviation of the surge force, the dimensional values are around 0.7 N. Sway forces have similar standard deviation values.

4.4.5 Validation of RIW ship forces

1. Discretization study

   The discretization of the RIW ship was performed at extreme shallow water, $h/T = 1.2$, and drift angle $\beta = 10°$. This condition is rather extreme, as smaller drift angles are expected for this water depth. The calculations were performed with the ship fully appended, including propeller and rudders. Following the procedure of Oberhagemann and el Moctar (el Moctar, Schellin, et al. 2021), I performed simulations on three successively finer grids. Starting with the coarse grid, I chose a refinement factor of $r_x = 1.6$ to obtain a medium and fine grid. Table 4.7 lists the number of cells of each grid, the associated grid refinement ratio Υ, the ship forces and the sinkage obtained from the three different grids. It also lists the linear and quadratic extrapolation values.

Table 4.7: Number of control volumes (Ncells), refinement ratio (Υ), surge force (F_x), sway force (F_y) and sinkage (z_M) obtained on the coarse, the medium, and the fine grid.

	Ncells (10^6)	Υ (-)	F_x (N)	F_y (N)	z_M (mm)
Coarse	1.78	1.0	-1.965	-157.080	-6.8
Medium	5.67	0.625	1.846	-147.348	-7.3
Fine	14.76	0.391	3.855	-148.369	-7.9
Extrapolated Linear	-	0	7.701	-140.600	-8.5
Extrapolated Quadratic	-	0	6.565	-145.25	-9.5

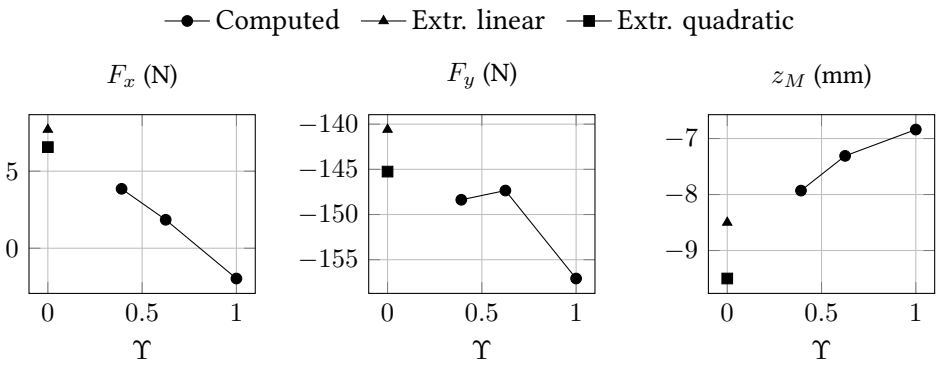

Figure 4.23: Surge force, sway force and amidship sinkage obtained during the grid discretization analysis of the RIW ship at $h/T = 1.2$ and drift angle $\beta = 10°$

Figure 4.23 shows the ship forces and amidships sinkage obtained during the grid discretization study. The longitudinal force and the sinkage show a monotonic con-

vergence. The transversal force shows an oscillatory convergence. The linear and quadratic extrapolation are plotted at $\Upsilon = 0$. As no experimental values are available, it is not possible to validate the calculations. However, the obtained forces and sinkage show a consistent convergence as the number of control volumes is increased.

2. Captive drift

   The Development Centre for Ship Technology and Transport System (DST) performed captive drift tests with a fully appended model of the RIW ship at a water depth ratio of $h/T = 1.5$. Only the mean values were available, without standard deviation or uncertainty. Figure 4.24 shows the comparison of the measured and computed nondimensional hydrodynamic sway force Y, yaw moment N and amidships sinkage z_M, during the drift tests. Two computational methods are shown, the free surface (RANS-FS) and the double-body with sinkage (RANS-DB). Both RANS calculations include all the appendages used during the model test, including the propeller and twin-rudders, the only difference being the treatment of the free surface. The propeller rotation was modelled using the moving reference frame technique.

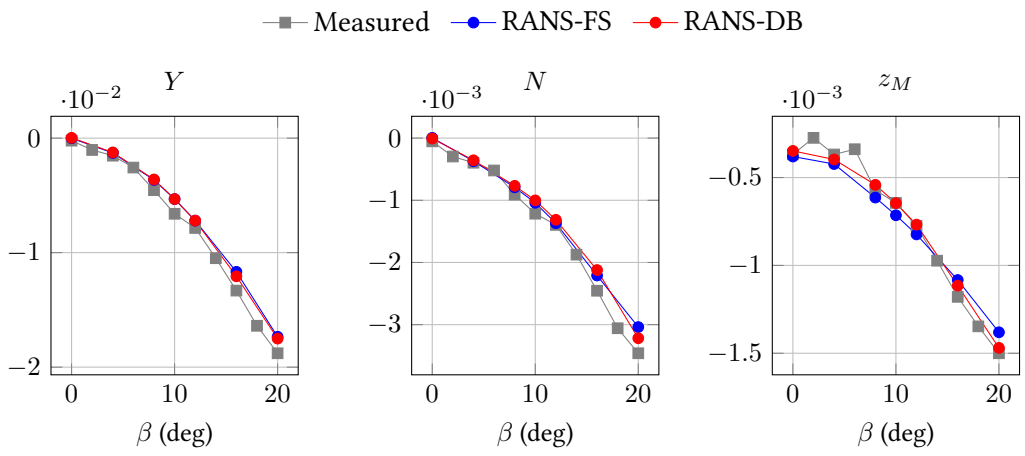

Figure 4.24: Comparison of nondimensional sway force Y, yaw moment N and amidship sinkage z_M of the RIW ship during drift captive tests at $h/T = 1.5$.

As can be seen in Fig. 4.24, the computed forces and sinkage correlates well with the experiments. For the largest drift angles, deviations of around 7% are observed for the sway force and yaw moment. Note that realistic rudder manoeuvres show that the smaller the water depth, the smaller the drift angle. For a water depth

ratio of $h/T = 1.5$, drift angles of less than 10° are expected for normal rudder manoeuvres. However, higher drift angles were calculated to test the capabilities of the numerical method.

3. Captive circular motion

   The Hamburg Ship Model Basin (HSVA) performed arc motions with their computerized planar motion carriage and obtained the forces and moments induced by a pure yaw rotation in deep water conditions. Only the mean values were available, without standard deviation or uncertainty. The propeller rotation rate was chosen to give the same propeller load as full-scale—the same number of revolutions per ship length travelled. RANS based rotating-arm captive tests were performed using the double-body with sinkage re-meshing approach. Figure 4.25 shows the comparison of measured and computed surge force, sway force and yaw moment for different yaw rotation rates. In general, the computed forces correlate fairly well with the measured forces.

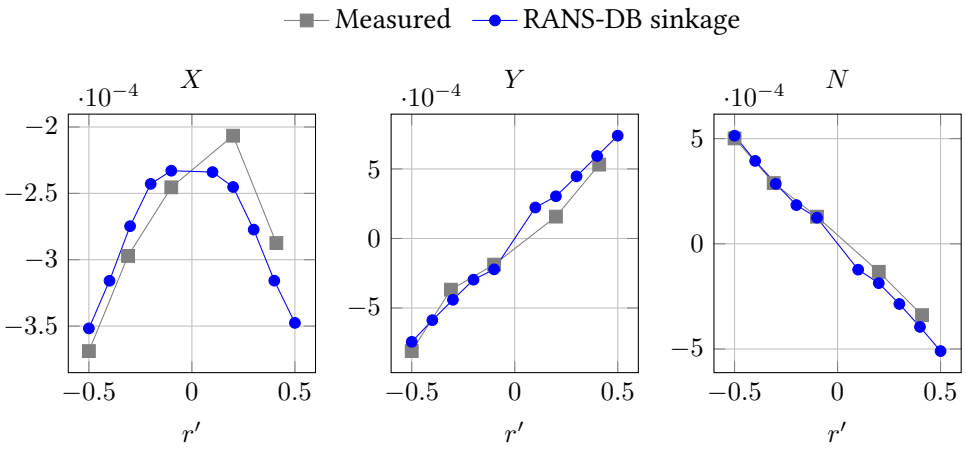

Figure 4.25: Comparison of nondimensional surge force X, sway force Y and yaw moment N during circular motion test in deep water. Measured data from HSVA and computed values using double-body approach including sinkage.

4.4.6 Turbulence modelling

Previous studies have highlighted the importance of turbulence modelling for shallow water hydrodynamics. Reports by Zentari, Tödter, et al. (2023) suggests that the standard k-ω SST fails to capture the complexity of the flow around for inland waterway ships in very shallow waters. Two turbulence models were therefore tested, the k-ω SST and the Reynolds stress model (RSM).

Figure 4.26 plots the comparison of the surge force, sway force, yaw moment, port side propeller thrust, starboard propeller thrust and amidship sinkage. The results show that there are differences in the longitudinal force. The surge force calculated with the RSM turbulence model appears to be shifted vertically. For the highest drift angles, $\beta = \pm 10°$, the RSM turbulence model predicts 30% less force than the k-ω SST. For the sway force and yaw moment the difference is about 2% and 3% respectively.

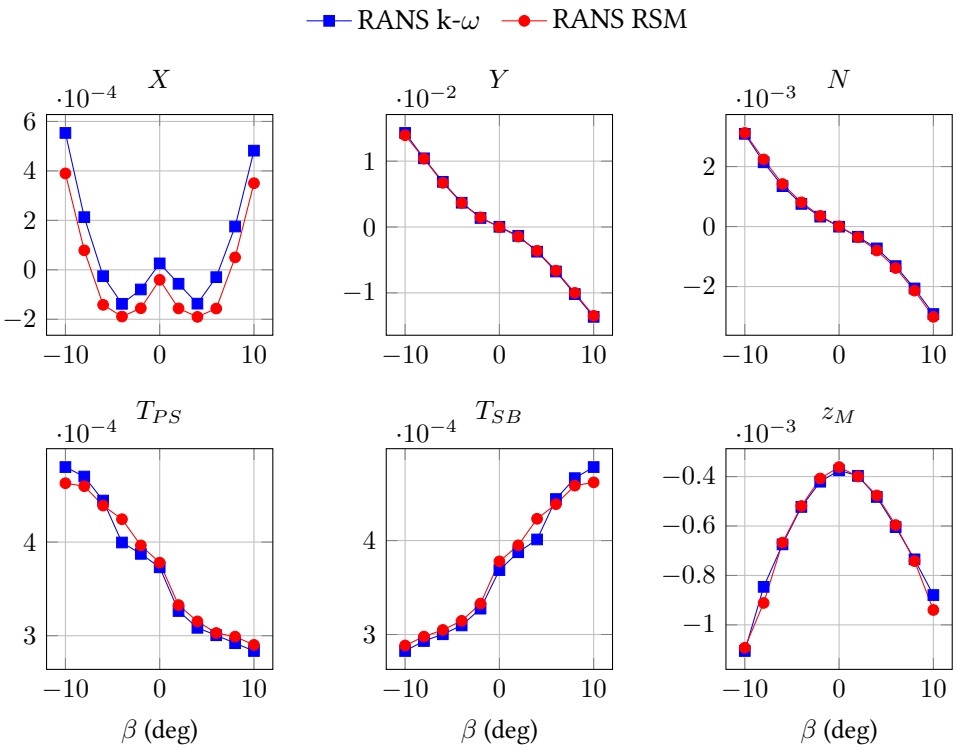

Figure 4.26: Comparison of nondimensional surge force X, sway force Y, yaw moment N, port side propeller thrust T_{PS}, starboard propeller thrust T_{SB} and sinkage z_M of the RIW ship during drift captive tests at $h/T = 1.5$

Similar to Fig. 4.26, Figure 4.27 plots the forces and moments of the rotating arm captive test. Again, the turbulence modelling has the greatest effect on the surge force. There is also a clear difference in the thrust of the propellers, particularly for the starboard propeller. For the highest rotation rate $r' = 0.5$, the surge force calculated with the RSM turbulence modelling is 50% higher than the surge force calculated with k-ω SST. For the same rotation rate, the differences in sway force and yaw moment are less than 1%.

The lack of experimental data makes it difficult to judge which of the models is closer to the real forces. On the one hand, the RSM is able to model asymmetric turbulence, which

seems to occur in shallow water hydrodynamics. On the other hand, the change in the turbulence model mainly affects the surge force, which is a small quantity compared to the sway force, and therefore its effects are limited to the longitudinal equation of motion and the loss of speed during rudder manoeuvres.

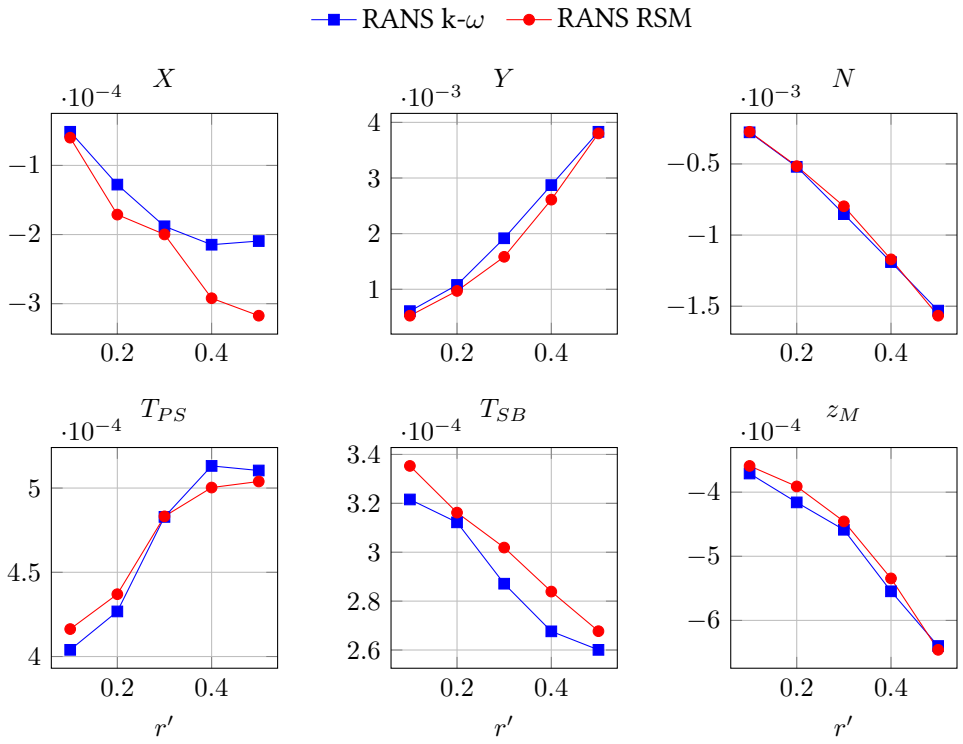

Figure 4.27: Comparison of nondimensional surge force X, sway force Y, yaw moment N, port side propeller thrust T_{PS}, starboard propeller thrust T_{SB} and sinkage z_M of the RIW ship during captive rotating arm tests at $h/T = 1.5$

4.5 Data-driven indirect system identification

I developed an alternative method to obtain the manoeuvring hydrodynamic coefficients using measurements from free running model tests or full-scale trials—indirect system identification method. The method uses an Abkowitz-type model and assumes that the mathematical expressions of hydrodynamic forces are available. This assumption was important because different models exist for various kinds of ships. Thus, here I reduced the problem to the identification of the hydrodynamic coefficients of a well known manoeuvring model.

The method was formulated as a data-driven approach by solving the ship's equations of motion directly. Each data point in the measurement record provided an equation that had to satisfy the equations of motion. In this way, the complexity of the equations used in system identification was reduced to a linear system of equations for each degree of freedom. In addition to minimizing the error, I focused more on obtaining a physically realistic solution, for which I applied constraints on the hydrodynamic coefficients during the minimization problem.

4.5.1 Methodology

The ship is considered to be moving in the horizontal plane in three degrees of freedom, namely the two translational motions, surge and sway, and the one rotational motion, yaw. For this reason, the equations of motion of the ship presented in Section 2.3.4 are reduced to the 3DoF, which reads as follows:

$$m\dot{u} - m(vr + x_G r^2) = X(\dot{u}, u, v, r, \delta) \tag{4.18}$$

$$m\dot{v} + mx_G\dot{r} + mur = Y(\dot{v}, \dot{r}, u, v, r, \delta) \tag{4.19}$$

$$mx_G\dot{v} + I_{zz}\dot{r} + mx_G ur = N(\dot{v}, \dot{r}, u, v, r, \delta) \tag{4.20}$$

Solving the ship motion equations (4.18) to (4.20) relied on measured input data obtained from free running model tests. In principle, ship velocities and accelerations can be measured directly during these tests. If these are not available, they can be derived from the ship's trajectory measurements.

1. Data

   Table 4.8 lists the two data sets needed to carry out the indirect system identification. The first set comprises ship parameters mass m, moment of inertia I_{zz}, longitudinal centre of gravity x_G, and reference speed U_0. The second set, obtained from free running model tests, consists of time records of the ship's position (ξ, η), its heading angle ψ, its velocities (u, v, r), its accelerations $(\dot{u}, \dot{v}, \dot{r})$, and its rudder deflection δ. From these time records, the method only uses the velocities and accelerations. The ship position and heading are used only in case the velocities or acceleration were not measured.

   I identified three scenarios of available measurement data to facilitate the generation of input data for system identification. In the first scenario, consisting only of the ship's trajectory and heading, the translational velocities must be derived from

Table 4.8: Data sets for indirect system identification

Description	Symbols	Units
Reference forward speed	U_0	$\mathrm{m\,s^{-1}}$
Ship mass	m	kg
Long. centre of gravity	x_G	m
Moment of inertia about z-axis	I_{zz}	$\mathrm{kg\,m^2}$
Time	t	s
Ship position	ξ, η	m
Ship heading	ψ	$^\circ$
Ship body velocity	u, v	$\mathrm{m\,s^{-1}}$
Ship body yaw velocity	r	$^\circ\,\mathrm{s^{-1}}$
Ship body accelerations	$\dot{u}, \dot{v}$	$\mathrm{m\,s^{-2}}$
Ship body yaw acceleration	$\dot{r}$	$^\circ\,\mathrm{s^{-2}}$
Rudder deflection	δ	$^\circ$

the ship's trajectory measurements and the yaw rate from the heading measurements. The accelerations are derived from last calculated velocities. In the second scenario, consisting of additional measured velocities and yaw rate, only the accelerations have to be derived from the measured velocities. In the third scenario, comprising measured velocities and accelerations, they can be used directly as input data. In all cases, the rudder measurement is expected to be available. Figure 4.28 shows schematically these three scenarios of available measurement data, where grey boxes indicate measured data and white boxes indicate calculated data.

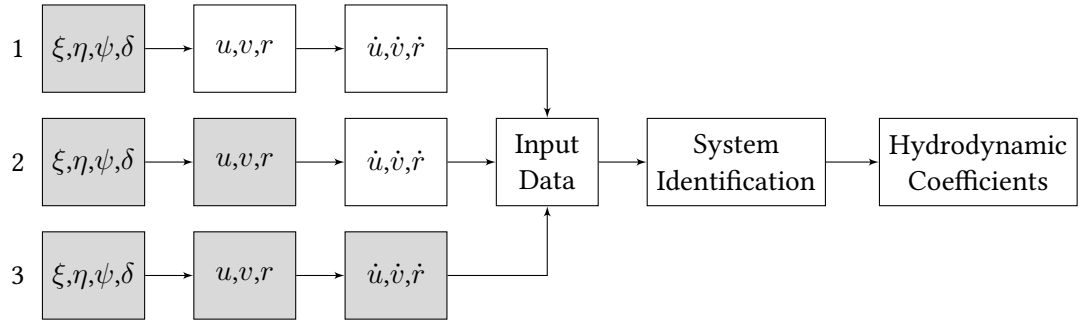

Figure 4.28: Schematic representation of three system identification scenarios using measured data (grey boxes) and/or computed data (white boxes), provided that ship's path and its heading are available

The numerical calculations of velocities and accelerations were performed using the Savitzky-Golay numerical differentiation method (Ahnert and Abel 2007). This method first fits a given number of points to a second order polynomial. The time

derivative is then calculated using the polynomial coefficients, given the ship's velocity in the inertial coordinate system. Its projection onto the body-fixed coordinate system is then obtained via the well known kinematic equation.

2. The method

I demonstrate the procedure of the method with the surge equation of motion using Mucha's mathematical model (see Section 2.5.1). First, the surge equation of motion (4.18) is expressed such that all known terms appear on the right hand side as shown in equation (4.21). This includes the ship's mass, its centre of gravity, and the measured velocities and accelerations:

$$X(\dot{u}, u, v, r, \delta) = m\dot{u} - m(vr + x_G r^2) \tag{4.21}$$

Force $X(u, v, r, \delta)$ on its left hand side is replaced by the expression of the mathematical model:

$$X_{\dot{u}}\dot{u} + X_u \Delta u + X_{uu}\Delta u^2 + X_{vv}v^2 + X_{rr}r^2 + X_{vr}vr + X_{\delta\delta}\delta^2 = m\dot{u} - m(vr + x_G r^2) \tag{4.22}$$

According to Luo (2016), the indirect system identification technique is unable to determine the added masses $X_{\dot{u}}$, $Y_{\dot{v}}$, $Y_{\dot{r}}$, $N_{\dot{r}}$, and $N_{\dot{v}}$. Therefore, I computed all added mass coefficients using the Euler equations based technique presented in Section 4.3. As these added masses are now considered known, they can be moved to the right hand side of equation (4.22) to yield the following equation:

$$X_u \Delta u + X_{uu}\Delta u^2 + X_{vv}v^2 + X_{rr}r^2 + X_{vr}vr + X_{\delta\delta}\delta^2 = (m - X_{\dot{u}})\dot{u} - m(vr + x_G r^2) \tag{4.23}$$

The left hand side contains only unknown coefficients. The equation (4.23) is valid for every manoeuvring state of the ship and should therefore satisfy every measurement point during the free running model tests. Applying the equation to each measured point of the time record results in a system of equations consisting of

vector and matrices, where each row corresponds to a measured point of a manoeuvring state:

$$\begin{bmatrix} \Delta u & \Delta u^2 & v^2 & r^2 & \delta^2 & vr \\ | & | & | & | & | & | \\ \vdots & \vdots & \vdots & \vdots & \vdots & \vdots \\ | & | & | & | & | & | \end{bmatrix} \begin{bmatrix} X_u \\ X_{uu} \\ X_{vv} \\ X_{rr} \\ X_{\delta\delta} \\ X_{vr} \end{bmatrix} = \begin{bmatrix} (m - X_{\dot{u}})\dot{u} - m(vr + x_G r^2) \\ | \\ \vdots \\ | \end{bmatrix} \tag{4.24}$$

Following the procedure for the sway and yaw equations, the following expressions were obtained:

$$\begin{bmatrix} 1 & v & r & \delta & v^3 & r^3 & v^2 r & vr^2 & \delta^3 & \Delta u\delta \\ | & | & | & | & | & | & | & | & | & | \\ \vdots & \vdots & \vdots & \vdots & \vdots & \vdots & \vdots & \vdots & \vdots & \vdots \\ | & | & | & | & | & | & | & | & | & | \end{bmatrix} \begin{bmatrix} Y_0 \\ Y_v \\ Y_r \\ Y_\delta \\ Y_{vvv} \\ Y_{rrr} \\ Y_{vvr} \\ Y_{vrr} \\ Y_{\delta\delta\delta} \\ Y_{u\delta} \end{bmatrix} = \begin{bmatrix} Y_{RHS} \\ | \\ \vdots \\ | \end{bmatrix} \tag{4.25}$$

$$\begin{bmatrix} 1 & v & r & \delta & v^3 & r^3 & v^2 r & vr^2 & \delta^3 & \Delta u\delta \\ | & | & | & | & | & | & | & | & | & | \\ \vdots & \vdots & \vdots & \vdots & \vdots & \vdots & \vdots & \vdots & \vdots & \vdots \\ | & | & | & | & | & | & | & | & | & | \end{bmatrix} \begin{bmatrix} N_0 \\ N_v \\ N_r \\ N_\delta \\ N_{vvv} \\ N_{rrr} \\ N_{vvr} \\ N_{vrr} \\ N_{\delta\delta\delta} \\ N_{u\delta} \end{bmatrix} = \begin{bmatrix} N_{RHS} \\ | \\ \vdots \\ | \end{bmatrix} \tag{4.26}$$

Each equation is reduced to a linear system of equations, now expressed as follows:

$$\mathbf{Ax} = \mathbf{b} \tag{4.27}$$

were $\mathbf{A}$ is the velocity matrix, $\mathbf{x}$ is the hydrodynamic coefficient vector, and $\mathbf{b}$ is the force vector. Several options are available to solve this system of equations (4.27). Depending on the method chosen, the principle idea is to solve for vector $\mathbf{x}$ by minimizing a loss function $L(\mathbf{x})$:

$$\underset{\mathbf{x}}{\operatorname{argmin}}\, L(\mathbf{x}) \tag{4.28}$$

Some standard methods and their loss functions are:

a) Least squares : $L = \|\mathbf{Ax} - \mathbf{b}\|_2$

b) Ridge : $L = \|\mathbf{Ax} - \mathbf{b}\|_2 + \alpha\|\mathbf{x}\|_2$

c) Lasso : $L = \|\mathbf{Ax} - \mathbf{b}\|_2 + \lambda\|\mathbf{x}\|_1$

d) Elastic-Net : $L = \|\mathbf{Ax} - \mathbf{b}\|_2 + \lambda\|\mathbf{x}\|_1 + \alpha\|\mathbf{x}\|_2$

where α and λ are regulating factors that penalize the large variation of coefficients. Symbols $\|\cdot\|_1$ and $\|\cdot\|_2$ represent the L1-norm and L-2 norm respectively.

The least squares method is a simple and appropriate technique to solve this system of equations as it minimizes the function $L(\mathbf{x}) = \|\mathbf{Ax} - \mathbf{b}\|_2$. In the absence of noise and uncertainties, which is the case for simulated data, the least squares method yields satisfactory results. However, when noise and measurement uncertainties are present, the least squares method performs poorly. Advanced methods such as Ridge regression or Elastic-Net deal better with noise data, but do not guarantee a physical coefficients.

To enforce obtaining physically realistic coefficients in the regression, I relied on knowing the physical characteristics of some of the hydrodynamic coefficients. For instance, knowing that X_u, Y_v, and N_r are terms with a negative sign allow to conveniently apply this constraint to the minimization problem as follows:

$$\underset{\mathbf{x}}{\operatorname{argmin}} \|\mathbf{Ax} - \mathbf{b}\|_2, \quad \text{subject to:} \quad \mathbf{x}_{min} < \mathbf{x} < \mathbf{x}_{max} \tag{4.29}$$

where $\mathbf{x}_{min}$ and $\mathbf{x}_{max}$ are the lower and upper bounds of $\mathbf{x}$, respectively. Table 4.9 lists the coefficients for which the sign is known. For coefficients with a negative

sign, such as X_u, the lower and upper bounds are -1 and 0, i.e., $-1 < X_u < 0$. For coefficients of unknown sign, the lower and upper bounds vary between -1 and $+1$. Recall that the system identification is performed with non-dimensional coefficients. Therefore, these limits are appropriate. To solve equation (4.29), I use the constrained least-squares algorithm available in the open source SciPy optimization package. The algorithm first computes the unconstrained least-squares and returns its solution as optimal if the coefficients are within the bounds. If not, the algorithm starts an iterative process to find the solution based on the Trust Region Reflective algorithm (Branch et al. 1999).

Table 4.9: Sign of coefficients based on physical knowledge of the hydrodynamic forces and based on the definition of the body-fixed coordinate system

X-coefficient	sign	Y-coefficient	Sign	N-coefficients	Sign
X_u	$-$	Y_v	$-$	N_r	$-$
X_{vv}	$-$	Y_δ	$-$	N_δ	$+$
$X_{\delta\delta}$	$-$	Y_{vvv}	$-$	N_{rrr}	$-$
		$Y_{\delta\delta\delta}$	$+$	$N_{\delta\delta\delta}$	$-$

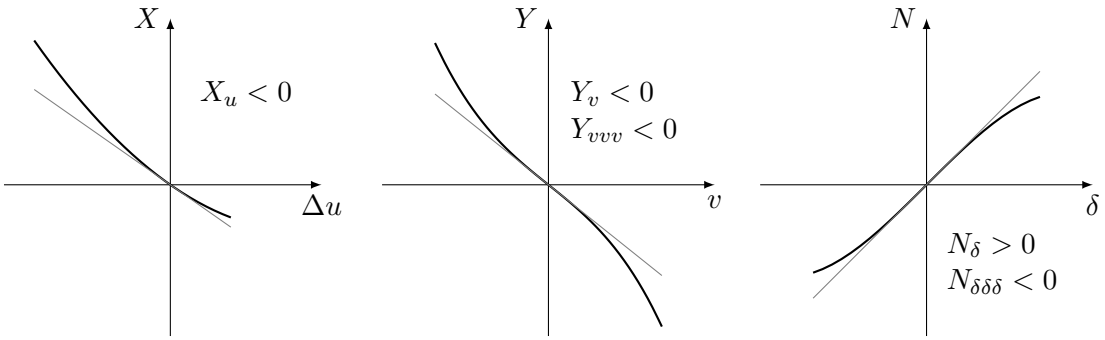

Figure 4.29: Characteristic behaviour of the forces and moment observed in conventional ships with respect the body-fixed coordinate system.

The signs of the coefficients presented in Table 4.9 were inferred from the patterns found in the captive model tests (Wolff 1981). Some coefficients such as X_{rr} or Y_r depend on the characteristics of the hull geometry and may be positive or negative. The sign of the nonlinear coefficients was observed for conventional ships such as tankers, containers and bulky cargo inland waterway ships. However, care should be taken when applying the signs of Table 4.9 to new types of ships. Figure 4.29 shows an example of how the signs of the coefficients were deduced from the characteristic behaviour of the forces and moments. Specifically, Fig. 4.29 plots the surge force X against the surge speed variation Δu, the sway force Y against the

sway speed v, yaw moment N against rudder deflection δ. For the rudder angle I use the convention that a positive rudder angle produces a positive rotation rate. The signs of the rudder coefficients therefore follow this convention.

4.5.2 Verification and validation

The verification and validation of the method was carried out with the KVLCC2 tanker. Table 4.10 lists its principal particulars. The associated model scale ratio λ corresponded to the model tests carried out at MARIN (Quadvlieg and Brouwer 2011).

Table 4.10: Principal particulars of the KVLCC2 tanker

Principal particulars	Symbol	Unit	Full-scale	λ=45.7
Length between perp.	L_{pp}	m	320.0	7.0
Length at waterline	L_{wl}	m	325.5	7.1204
Breadth at waterline	B	m	58.0	1.1688
Draft	T	m	20.8	0.455
Displacement	Δ	m^3	312622	3.2724
Wetted surface	S_w	m^2	27194.0	13.0129
Block coefficient	C_b	-	0.81	0.81
Long. COG	LCG	m	11.1	0.24
Metacentric height	GM	m	5.71	0.125
Inertia radius x	r_{xx}	m	23.2	0.467
Inertia radius y	r_{yy}	m	80.0	1.75
Inertia radius z	r_{zz}	m	80.0	1.75

The verification of the method is first performed with a simulated zig-zag 35°/35° manoeuvre of the KVLCC2 tanker. Then, the validation is carried out using measured data from the KVLCC2 tanker's free running tests. The experimental data provided include trajectories and velocities, but not accelerations. They therefore correspond to the second scenario in Fig. 4.28.

1. Verification with simulated data

   Mucha (2017) made available the hydrodynamic coefficients of the KVLCC2 tanker listed in Table 4.11. These coefficients were obtained from numerical captive tests performed using Reynolds-averaged Navier-Stokes (RANS) equations. The aim here is to demonstrate the validity of the method. Using these coefficients, I simulated a zig-zag 35°/35° manoeuvre, as shown in Figure 4.30. The kinematic parameters and rudder deflections of the simulated manoeuvre were used as input data to perform the indirect system identification. These coefficients are listed in Table

4.11. For this simple case, where the mathematical model is known exactly and there is no uncertainty, the constrained least squares algorithm did not activate the iterative process. The simple least squares regression already provided a solution within the bounds.

Table 4.11: KVLCC2 hydrodynamic manoeuvring coefficients (multiplied by 10^3) from RANS captive tests of Mucha (2017) and from the current indirect system identfication

	Mucha	Current method	% difference
Xu	-1.97	-2.00	1.5
Xuu	0.99	1.02	3.0
Xvv	-5.00	-5.53	10.6
Xrr	0.48	0.54	12.5
Xvr	7.54	7.71	2.3
Xdd	-1.82	-1.84	1.1
Y0	-0.15	-0.15	0.0
Yv	-24.90	-25.44	2.2
Yr	4.76	4.94	3.8
Yd	-3.77	-3.82	1.3
Yvvv	-30.20	-30.92	2.4
Yrrr	-1.22	-1.14	-6.6
Yvvr	-9.90	-9.55	-3.5
Yvrr	-40.30	-40.04	-0.6
Yddd	3.33	3.46	3.9
Ydu	4.56	4.58	0.4
N0	0.07	0.07	0.0
Nv	-8.80	-8.86	0.7
Nr	-3.25	-3.27	0.6
Nd	1.79	1.85	3.4
Nvvv	8.00	8.67	8.4
Nrrr	-0.92	-0.93	1.1
Nvvr	-7.10	-6.61	-6.9
Nvrr	7.00	7.27	3.9
Nddd	-1.62	-1.72	6.2
Ndu	-2.32	-2.36	1.7

The coefficients obtained by indirect system identification compared favourably with Mucha's coefficients, i.e., all coefficients were accurately predicted. Figure 4.31 plots the comparative trajectories of the KVLCC2 tanker performing a turning circle manoeuvre for a rudder angle 35° to port. This almost identical turning circle trajectories presented in Figure 4.31 demonstrated that any kind of manoeuvre

using our system identified coefficients were expected to closely match the manoeuvres performed using Mucha's coefficients.

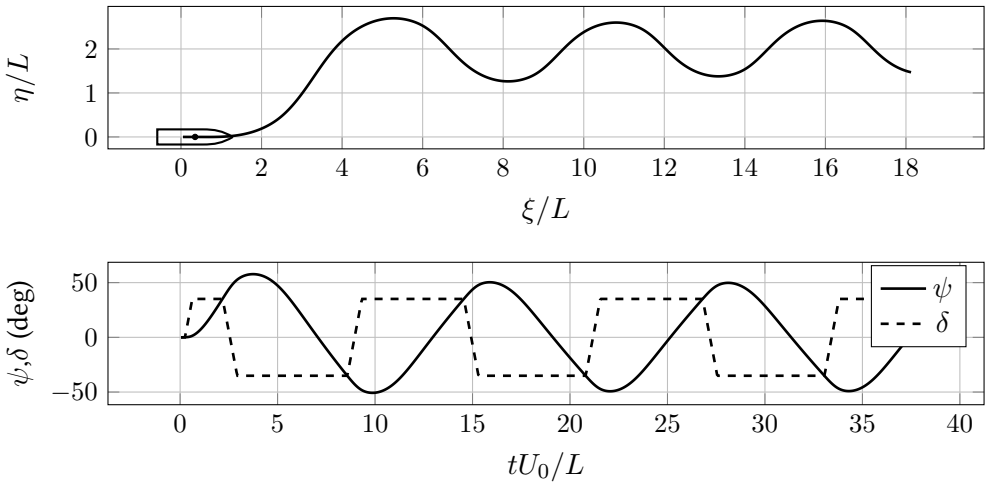

Figure 4.30: Ship trajectory (top), heading and rudder angle (bottom) of the KVLCC2 tanker during zig-zag 35°/35° manoeuvre

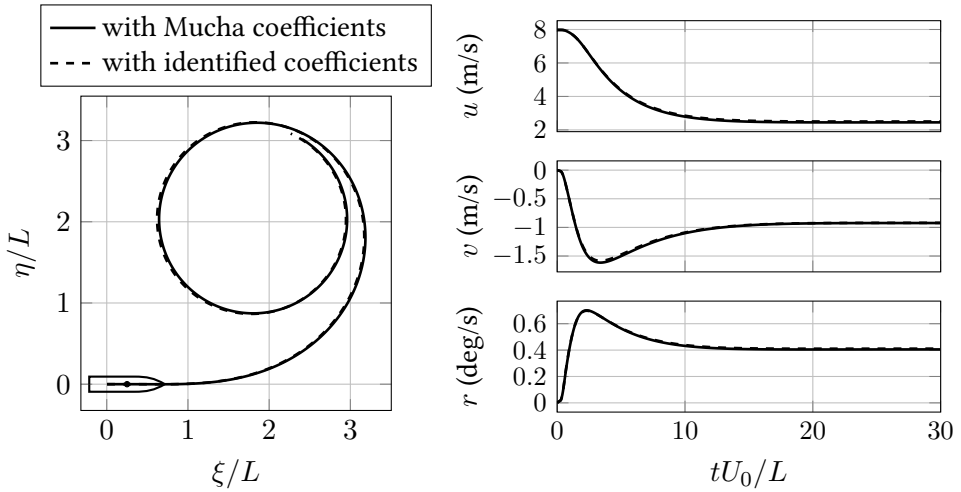

Figure 4.31: Comparative trajectories and velocities of the KVLCC2 tanker performing a turning circle manoeuvre with rudder angle $\delta = 35°$ to port side.

The least-squares regression method performed well because, first, these coefficients are linear, i.e. they do not contain higher order terms, nor are they multiplied by each other. Second, the data used were obtained from numerical simulations; this is different when dealing with measurement data, that usually are noise and contains instrumental uncertainties.

2. Validation with free running model tests

The validation of the method is performed with free running manoeuvring data of the KVLCC2 ship provided by the Maritime Research Institute Netherlands (MARIN) (Quadvlieg and Brouwer 2011). These model tests were performed during the SIMMAN 2008 workshop. The Hamburg Ship Model Basin (HSVA) also carried out free running tests with the KVLCC2 tanker (Stern et al. 2011). Table 4.12 lists the free running tests. The first three tests were carried out at MARIN and the last two at HSVA. I selected the tests from MARIN for system identification: the zig-zag 10°/10° SB, the zig-zag 20°/20° PS, and the turning circle 35° to starboard. Quadvlieg and Brouwer (2011) also documented the uncertainty of the measurements carried out at MARIN. For example, the first overshoot angle has an uncertainty of 1.6°, while the time of the first overshoot angle has an uncertainty of 12 s. Figure 4.32 plots their measured trajectories and associated velocities and rudder angles. The free running tests carried out at the HSVA were used exclusively to validate the coefficients obtained by indirect system identification.

Table 4.12: Free running manoeuvres of the KVLCC2 at MARIN and HSVA.

	Name	Manoeuvre	δ	ψ	Rudder start to
1	ZZ-10/10-SB	zig-zag	10°	10°	starboard
2	ZZ-20/20-PS	zig-zag	20°	20°	port
3	TC-35-SB	turning circle	35°	-	starboard
4	ZZ-15/5	zig-zag	15°	5°	starboard
5	ZZ-20/10	zig-zag	20°	10°	starboard

The use of different free running tests allowed a wider range of variation in kinematic parameters and rudder deflections. The turning circle, for example, provided the greatest variation in surge speed and acceleration. The coefficients obtained from the indirect system identification were used to simulate the HSVA zig-zag manoeuvres. Figure 4.33 plots the comparative computed and measured trajectories, rudder angles δ, heading angles ψ, surge speeds u, and sway speeds v, during the zig-zag 15°/5° manoeuvre starting to starboard. Despite the small difference between computed and measured values, good correlation is found. The computed first and second overshoot angles are 5.5° and 11.2°, respectively, while the measured ones are 6.6° and 12.8°, which represent a maximum under prediction of 1.6°.

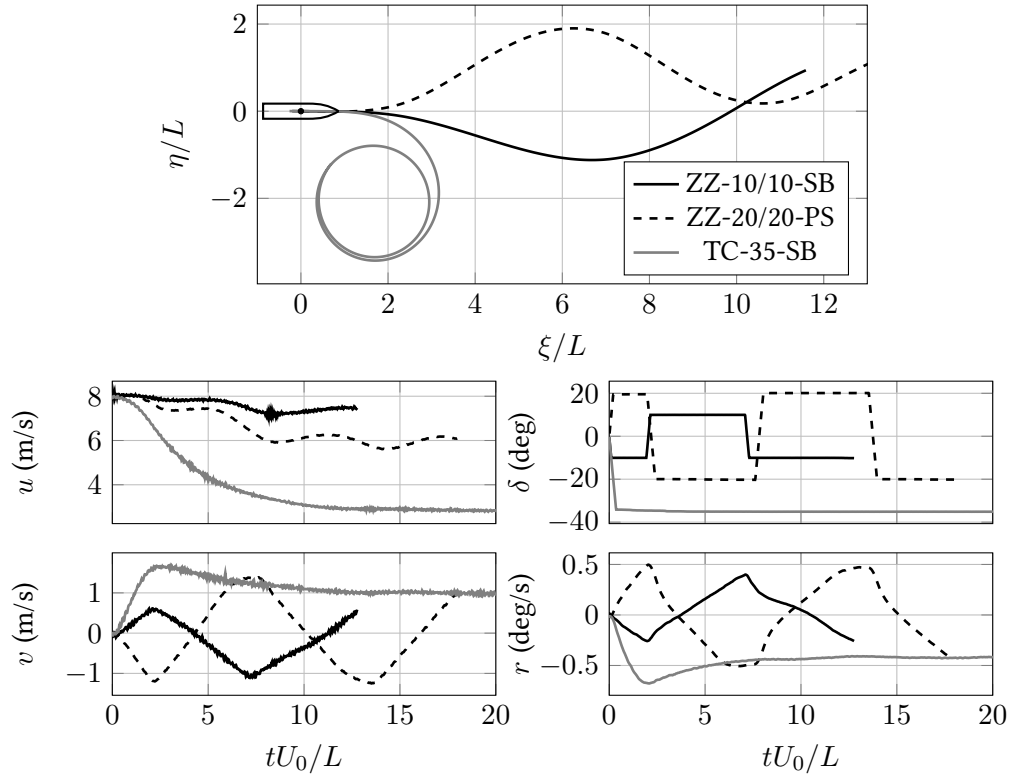

Figure 4.32: Measured trajectories, surge speed, sway speed, rudder angle, and yaw rotation rate of the KVLCC2 ship during zig-zag 10°/10° SB, zig-zag 20°/20° PS, and turning circle manoeuvre with 35° rudder deflection to starboard of MARIN

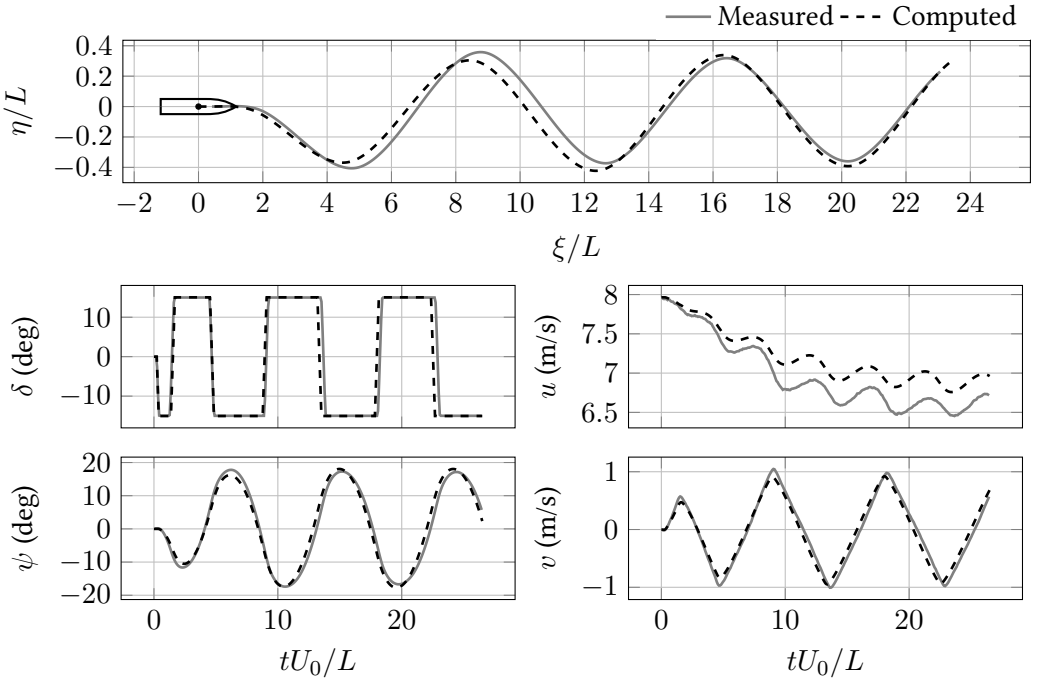

Figure 4.33: Measured and computed trajectories, rudder angle, heading, and velocities of the KVLCC2 tanker during zig-zag 15°/5° manoeuvre starting to starboard

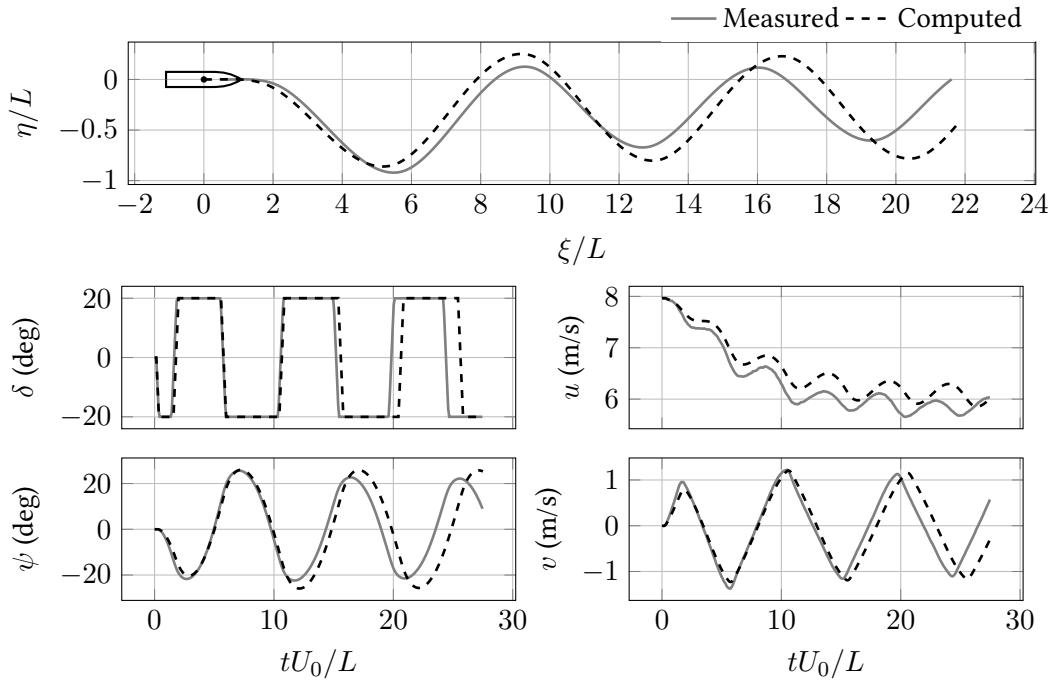

Figure 4.34: Measured and computed trajectories, rudder angle, heading, and velocities of the KVLCC2 tanker during zig-zag 20°/10° manoeuvre starting to starboard

Similar to Fig. 4.33, Figure 4.34 plots the comparative computed and measured trajectory and kinematic parameters during the zig-zag manoeuvre 15°/5°. The computed accuracy appears to be good for the non-dimensional time less than ten, where the first and second overshoot angles are captured with good accuracy.

Table 4.13 provides a quantitative comparison of the measured and computed zig-zag manoeuvres. The computed values in Fig. 4.34 were obtained using the hydrodynamic coefficients based on the measured velocities (scenario 2). As seen, the computed first overshoot angle is 10.3°, which is only 1.4° less than the measured overshoot angle. The computed first overshoot time is 51.7 s, which is only 3.7 s less than the measured time. Even smaller comparative errors were obtained for the computed second overshoot angle and the overshot time.

For the non-dimensional time greater than ten, the errors start to grow and the computed values deviate from the measured ones. Recall that only three manoeuvres with short time records were used for the system identification. The more data is available for system identification, the better is the prediction of the hydrodynamic coefficients. For this reason, it is recommended to use different types of

Table 4.13: KVLCC2 zig-zag 20°/10° results from experiments and computations based on trajectories (scenario 1) and based on velocities (scenario 2)

Description	Unit	Experiment	Comp. scenario 1	Comp. scenario 2
Reach	s	192.5	195.4	195.0
Period	s	384.1	393.0	390.3
1st overshoot angle	deg	11.7	10.0	10.3
2nd overshoot angle	deg	15.6	16.4	16.0
1st overshoot time	s	55.4	50.9	51.7
2nd overshoot time	s	68.0	67.4	66.6

manoeuvres with a wide range of variation of the kinematic parameters and the rudder deflection.

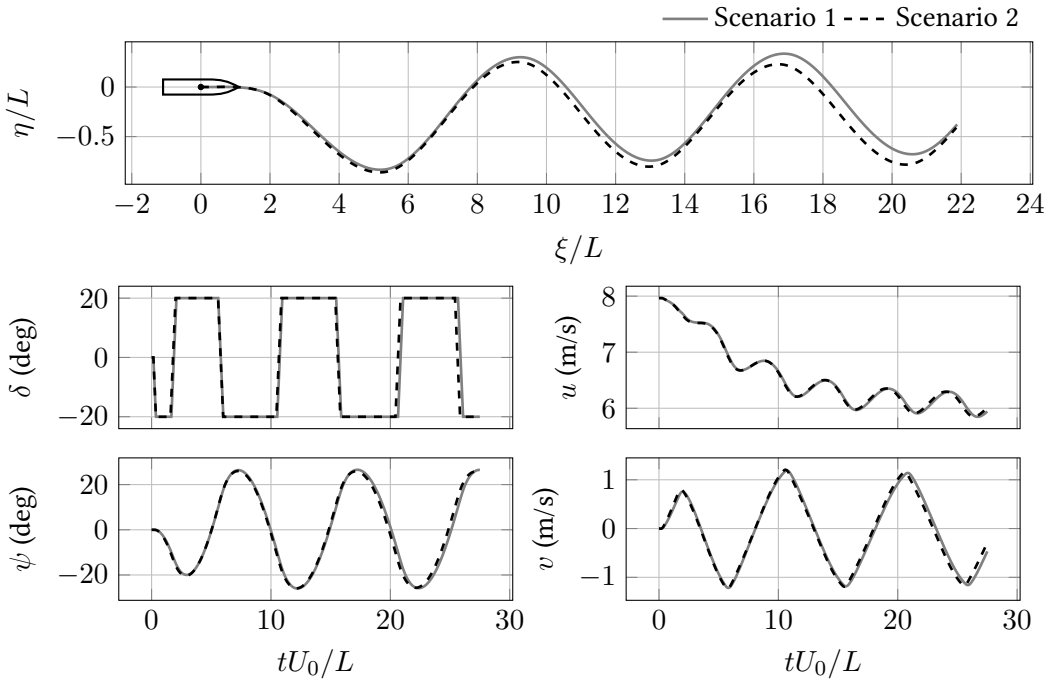

Figure 4.35: Trajectories, rudder angle, heading, and velocities of the KVLCC2 tanker during zig-zag 20°/20° manoeuvre starting to starboard. Scenarios 1 and 2 as described in Fig. 4.28

To asses the quality of the identification when only trajectories were available, we emulate the scenario 1 from Fig. 4.28 by using only the trajectories of the measurement data, i.e., velocities and accelerations were computed by numerical differentiation. Figure 4.35 plots the zig-zag 20°/10° manoeuvre using hydrodynamic coefficients obtained from trajectories (scenario 1) and velocities (scenario 2). As

seen, rudder deflections, heading angles and velocities were nearly identical, i.e., differences between the ship's trajectories were minor (see Table 4.13). This indicates that the method was able to obtain reliable hydrodynamic coefficients based on trajectories.

4.6 Ship trajectory validation

The mathematical model was validated using the RIW ship. Free running zig-zag manoeuvres were carried out in MARIN and provided by Mucha, Dettmann, et al. (2019). The zig-zag manoeuvres were performed for two water depths: a moderate water depth with $h/T = 3.0$ and an extreme shallow water depth with $h/T = 1.2$. For each water depth zig-zag 35°/5° manoeuvres were performed, one starting to starboard and one starting to port. Each manoeuvre was repeated three times to assess its reliability. The hydrodynamic coefficients of the mathematical model were determined using the methods presented in Sections 4.3 and 4.4.

Figure 4.36 plots the comparative computed and measured trajectories of the ship's free running manoeuvres for the moderate water depth condition $h/T = 3.0$. It also shows plots the associated measured and computed rudder deflection δ, heading angle ψ, surge speed u, sway speed v, and yaw rotation r. The grey coloured lines represent the three repeated test runs, the red lines identify the computed values. The kinematic parameters and the heading angle were captured with good accuracy. Deviations occur in the prediction of the trajectory, first because the computed rudder deflection does not exactly match the measured one. Second, due to the different initial conditions. Despite this deviation, the maximum and minimum values of the kinematic parameters are well captured, indicating that the manoeuvring forces have been modelled with good accuracy.

Similar to Fig. 4.36, Figure 4.37 plots the comparative computed and measured trajectories and associated kinematic parameters of the free running manoeuvres for the extreme shallow water condition $h/T = 1.2$. Again, the grey coloured lines represent the three repeated test runs and the red lines identifies the computed values. For this extreme condition the experimental values are more scattered. The three measured repetitions have slightly different initial conditions, each producing a different dynamic evolution. The computed kinematic parameters and the heading angle are within the scatter range of the measured data. In this case, the rudder angles are closer to one of the tests, which also improves the prediction of the trajectory.

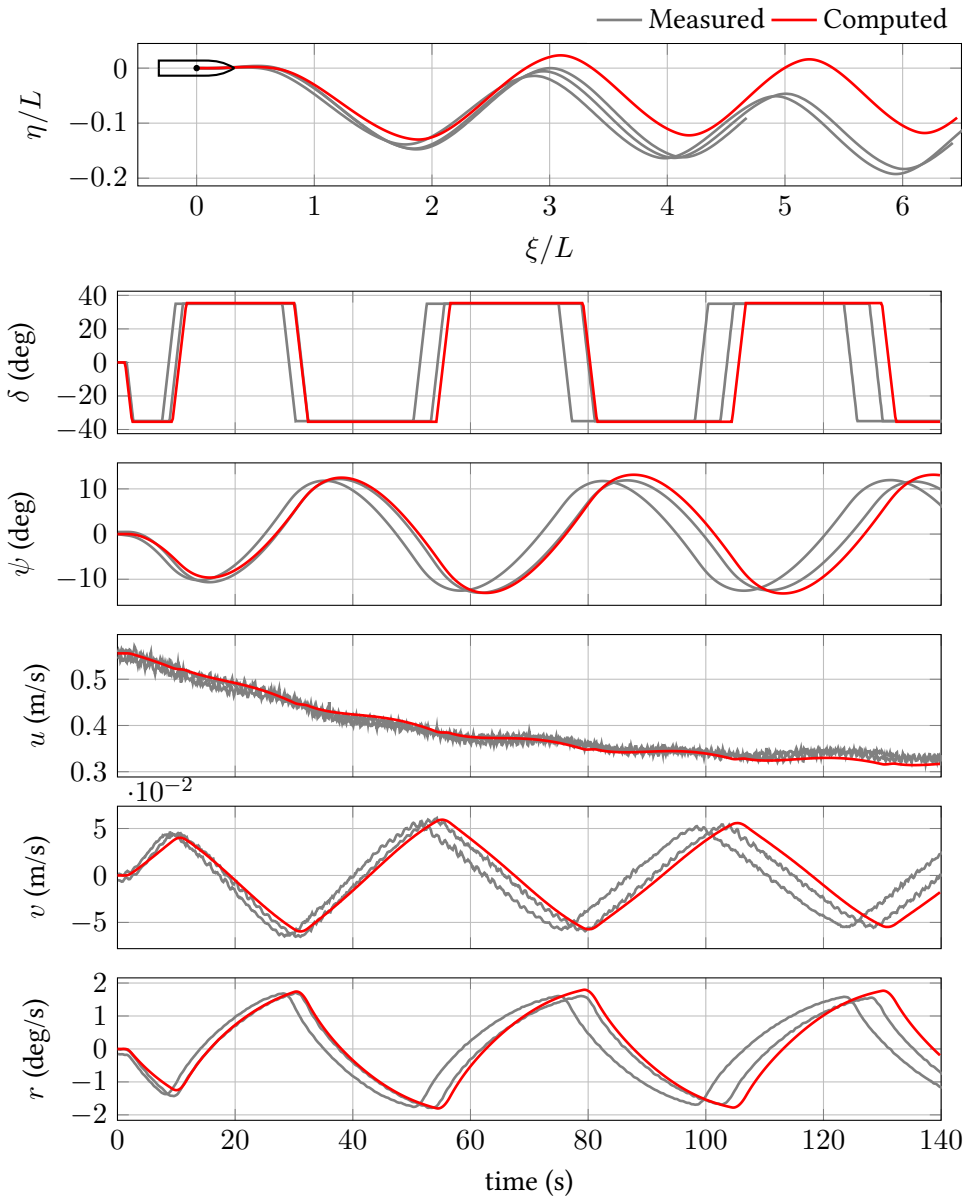

Figure 4.36: Measured and computed trajectories, rudder angle, heading, and velocities of the Reference inland waterway ship during zig-zag manoeuvre with 35°/5° starting to starboard at $h/T = 3.0$

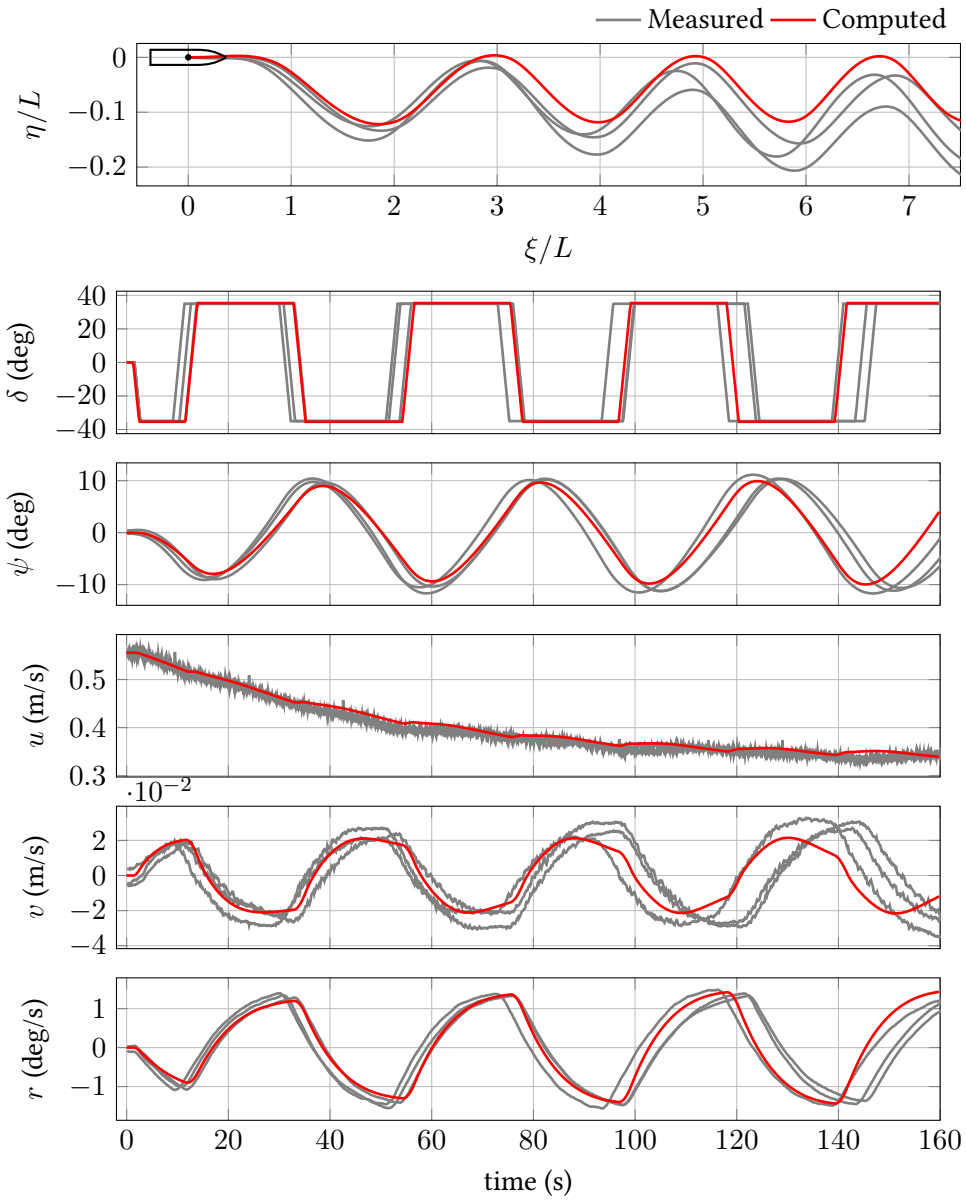

Figure 4.37: Measured and computed trajectories, rudder angle, heading, and velocities of the Reference inland waterway ship during zig-zag manoeuvre with 35°/5° starting to starboard at $h/T = 1.2$

5 Manoeuvring in waves

This chapter presents my contribution to the field of manoeuvring in waves. A numerical method for manoeuvring in regular waves is presented. The method uses the nonlinear 6DoF equations of motion described in the inertial coordinate system. Thus, all nonlinearities associated with the inertial rigid body motion are taken into account. It is assumed that the forces can be separated into calm water manoeuvring forces and wave-induced forces, allowing both forces to be calculated separately. Validation of the method was performed using the DTC containership, for which experimental measurements of turning circle manoeuvres in regular waves with different wave propagation directions are available.

5.1 Superposition of forces

The main assumption of the method is the superposition of forces. The hydrodynamic force $\mathbf{F}_h$ in equation (5.1) is split into the calm water manoeuvring force $\mathbf{F}_M$ and the wave-induced force $\mathbf{F}_W$. This division implies that the manoeuvring forces and the wave forces do not interact.

$$\mathbf{F}_h = \mathbf{F}_M + \mathbf{F}_W \tag{5.1}$$

The calm water manoeuvring force is calculated using the Abkowitz-type model. The forces are first calculated in the body-fixed coordinate system and then transformed to the inertial coordinate system. The wave-induced force is modelled by considering only the second order wave forces (time-averaged wave-induced forces). This assumption is based on the fact that first order wave forces have an average value of zero. Therefore, they do not contribute to the ship's drifting. In reality, wave-induced motion can alter the wetted surface, the hydrodynamic characteristics or induce the emergence of propeller and rudder. However, it is assumed that manoeuvring in waves takes place in coastal areas where only moderate sea conditions are observed and therefore the interaction of the manoeuvring and seakeeping forces may be neglected.

5.2 Wave forces

Several numerical methods exist to calculate second order wave forces. The most accurate and reliable solvers in the whole wave length range seem to be those based on RANS. The longitudinal drift force, which is called “added resistance”, was calculated by Sigmund and el Moctar (2018) for different ship geometries and different waves lengths in head waves. The authors showed that for short waves, $\lambda/L_{pp} < 0.36$, frictional forces have an important impact on the added resistance, which may be higher than 20%. However, this effect is less pronounced for full scale ships calculations.

Figure 5.1 shows the added resistance of the DTC containership for two speeds 6 kn and 16 kn presented in Sigmund and el Moctar (2018). In this thesis, the Rankine source boundary element method—GLRankine—was used to calculate the second order wave forces. The BEM calculations were performed using two different approaches. In the case of 6 kn ship speed ($Fn = 0.052$), a double body approach was used for the steady potential, while in the case of 16 kn ($Fn = 0.139$), the nonlinear steady potential due to ship speed was considered. For the 16 kn case, the wave forces calculated with the BEM correlate better with the experimental forces and the computed RANS forces. For the 6 kn speed, a consistent underestimation of added resistance around 9% was observed for wave lengths $\lambda/L_{pp} > 0.4$. Therefore, to avoid inaccuracies, a correction of 9% is applied in the BEM calculation of the second order wave forces is taken into account when using the double-body steady potential approach. A validation study of the GLRankine for second order forces and moments can be found in Lyu and el Moctar (2017) and Sigmund and el Moctar (2018).

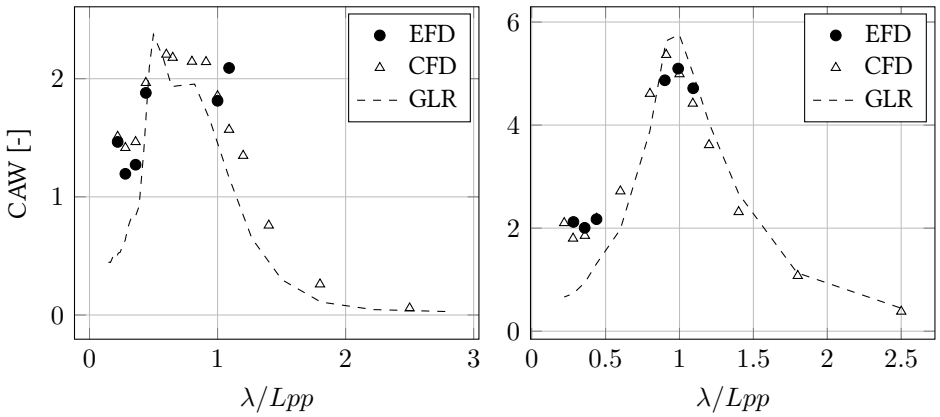

Figure 5.1: DTC added resistance coefficient for speeds 6 kn (left) and 16 kn (right) in head waves $\beta = 180°$. CFD data taken from Sigmund and el Moctar (2018)

Figure 5.2 shows the coordinate system and angles involved in the calculation of the second order wave forces. The wave propagation direction is described with the angle β_{wave} in the inertial coordinate system and is assumed to be constant during the simulation time. The angle β^* is the relative wave heading angle and is calculated as the difference between the wave propagation direction β_{wave} and ship heading angle ψ.

$$\beta^* = \beta_{wave} - \psi \tag{5.2}$$

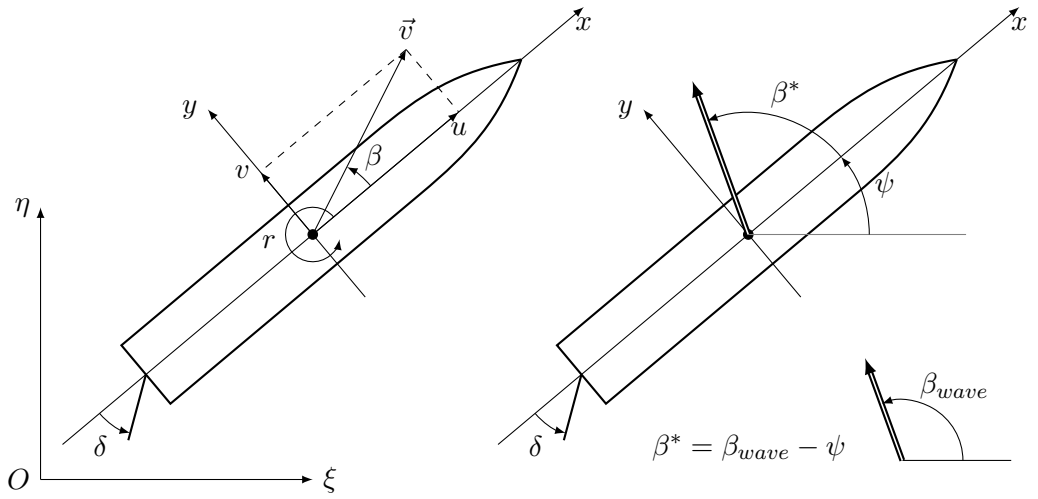

Figure 5.2: Coordinate system and planar angles involved in the second order wave calculation.

The second order wave forces for a given wave length can be expressed as a function of ship's velocity U, relative wave heading angle β^*, wave amplitude ζ_w and time t. Linear wave theory is assumed, thus, the calculated forces are valid for small wave steepness. The second order wave forces can be written as follows:

$$F_{2ORD} = f(U, \beta^*, \zeta_w; t) \tag{5.3}$$

The second order wave forces can be approximated as a continuous function. Furthermore, the ship velocity U can be approximated by the surge velocity u. This is done to simplify the simulation variables and in order to use potential flow solvers, solutions of which depend on the mean forward speed. On the other hand, the sway velocity v tends to be small and then such approximation is acceptable. Thus, the second order wave force reads:

$$F_{2ORD}(t) = \rho g L_{pp} \zeta_w^2 \hat{F}_{2ORD}(u(t), \beta^*(t)) \tag{5.4}$$

where $\hat{F}_{2ORD}$ represents the non-dimensional second order wave force, which can be obtained from any solver. The variables $u(t)$ and $\beta^*(t)$ are time dependent, because during a manoeuvre changes in surge velocity and relative wave heading are expected. In order to cover all possible encountered angles between the ship and a wave, the angle β^* must vary between 0° and 180°. The surge velocity u should cover the range in which the velocity is expected to vary. Initial values are recommended between $u = 0$ and u_{max}, with u_{max} equal to the initial velocity before the start of the manoeuvre. An example of second order wave force in longitudinal direction and moment around z-axis is shown in Figure 5.3 for a wave length $\lambda = 0.5L_{pp}$.

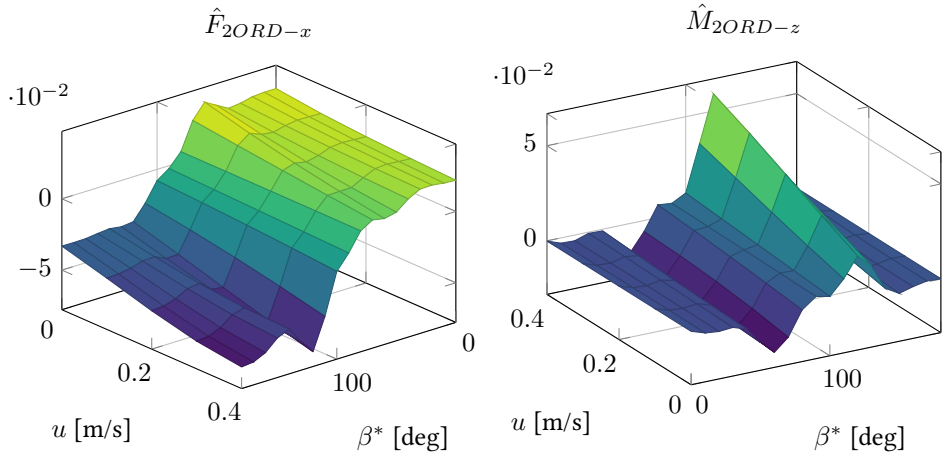

Figure 5.3: Example of second order wave forces for wave lenth $\lambda/L_{pp} = 0.5$. The added resistance $\hat{F}_{2ORD-x}$ (left) and moment $\hat{M}_{2ORD-z}$ (right)

5.3 Validation of manoeuvring in regular waves model

Free running manoeuvring tests in calm water and waves were carried out in the MARINTEK ocean basin to collect data for a benchmark study. The DTC containership model was constructed with a scale of $\lambda = 63.65$, see model's main particulars in Table 4.3. The tests were carried out at the design draft ($T = 14.5$ m at full scale) and with an initial forward speed of 0.387 m/s (6 knots at full scale). The DTC model was equipped with single screw propeller and twisted rudder. Details of the model tests can be found in Sprenger et al. (2017). A subset of the experiments was used here to validate the manoeuvring in waves model. Turning circle manoeuvres in calm water and regular waves with different wave propagation directions were simulated and compared with experimental data.

Figure 5.4 plots the comparative computed and measured ship's trajectory, surge velocity, and sway velocity of the turning circle manoeuvre with 35° rudder deflection set to starboard. In the transient part of the turning circle manoeuvre, the computed and measured trajectories correlate favourably. However, in the steady part, computations and measurements deviate. Theoretically, in the steady part, all forces are in equilibrium and the acceleration is zero. Thus, surge u and sway v velocities are constant. Nevertheless, experimental data of these values are varying. Thus, small accelerations are still occurring and forces are not in equilibrium. These forces induce the deviation from the theoretical trajectory.

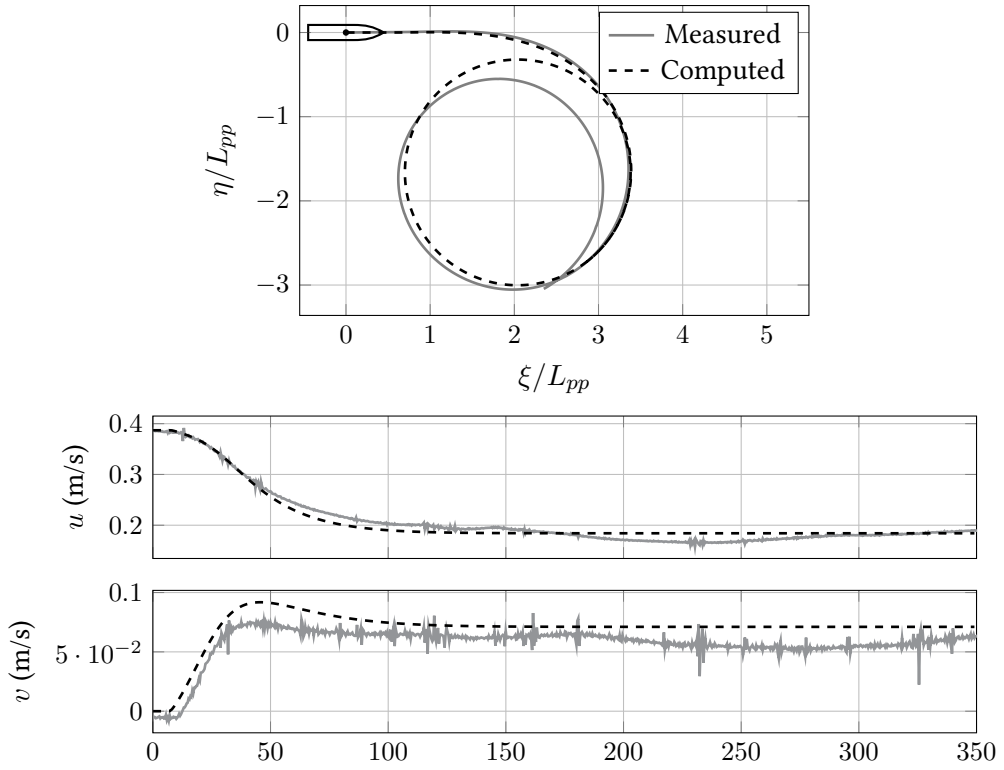

Figure 5.4: DTC turning circle manoeuvre in calm water with rudder angle of 35° set to starboard

Figure 5.5 plots the trajectories of the turning circle manoeuvres in regular waves of $\lambda/L_{pp} = 0.5$ with wave headings of 0°, 90° and 180°. The numerical simulation follows the experimental data at the beginning of the simulation and differences grow with time. At the end of the simulation the difference between numerical and experimental data is large. Nevertheless, the orientation of the drift is still captured.

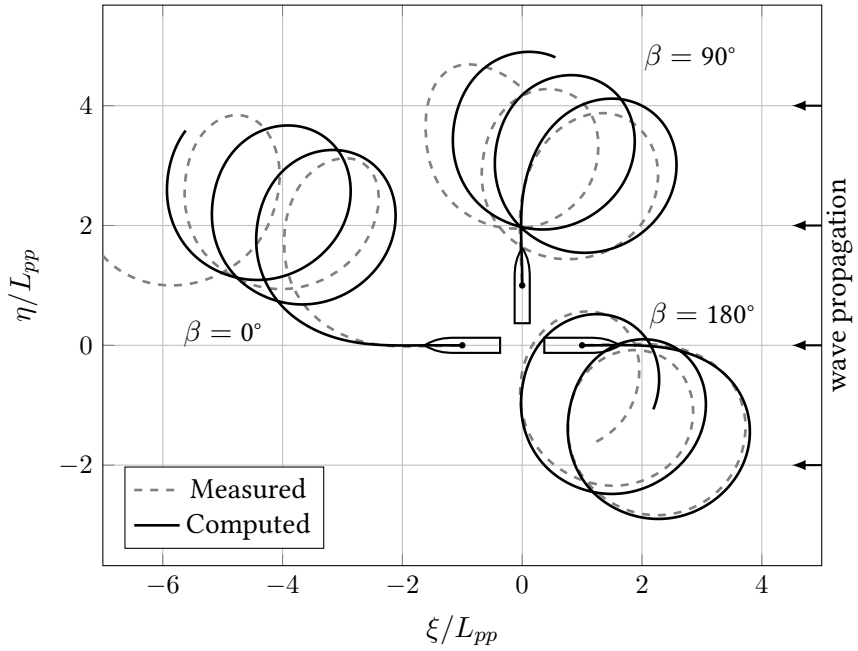

Figure 5.5: DTC turning circle manoeuvre in regular waves, $\lambda/L_{pp} = 0.5$ and $H = 2\,\text{m}$, for wave heading angles of 0°, 90° and 180° with initial forward speed corresponding to 6 kn full scale

The drift motion for the case of $\beta_{wave} = 180°$ correlates better with the experiments than for the cases of $\beta_{wave} = 0°$ and $\beta_{wave} = 90°$. This may be due to the lack of a propulsion model in the numerical simulations. The thrust was assumed to be constant for all wave headings (β_{wave}), which was not the case in the experiments. This assumption of constant thrust in the simulations seems acceptable for calm water manoeuvres. However, in waves, the added resistance affects the ship's speed and therefore the thrust of the propeller varies with the wave heading.

Let's analyse the case of $\beta_{wave} = 0°$. At the initial condition the relative heading angle was $\beta^* = 0°$. Thus, the added resistance force is positive and acts like an additional propulsion force (pushing effect). In order to keep a 6 kn forward speed, the initial propeller thrust was reduced (by adjusting the initial propeller revolution) compared with the calm water manoeuvre case. When the ship is turning and approaching a relative heading of $\beta^* = 180°$, the added resistance becomes negative and acts against the forward ship motion resulting in a lower ship speed (by keeping the initial propeller revolution constant). As the propeller thrust is smaller than in calm water, the model does not have enough thrust to sail against the waves and it is expected to make a faster turn than in

calm water. Such a behaviour is confirmed in Figure 5.5, where the turning for $\beta_{wave} = 0°$ is faster than for $\beta_{wave} = 90°$, which in turn is faster than $\beta_{wave} = 180°$.

Figure 5.6 compares surge and sway velocities for the above cases. Again a good correlation can be found between computations and measurements at the beginning of the manoeuvre. However, the deviations become higher with increasing simulation time. The computed and measured average picks and troughs values correlate favourably, but there is a shift over time. In case of $\beta_{wave} = 0°$, measured and computed minimum surge velocities were around 0.1 m/s and 0.15 m/s, respectively. Such a difference indicates that a higher longitudinal force was acting on the model. Thus, it is likely that the lack of propeller dynamics in the simulation is the main reason for these deviations. At the time $t = 130$ s the ship had a relative heading of $\beta^* = 180°$. Thus, the added resistance act against the forward ship motion, and a local minimum of surge velocity was observed in both, measured and computed values.

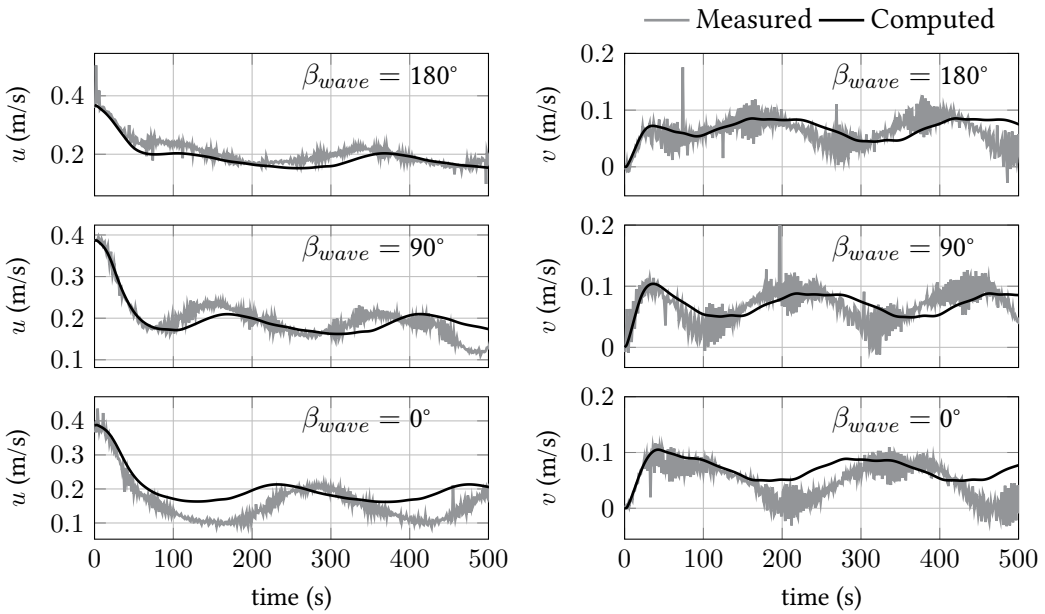

Figure 5.6: DTC velocities during turning circle manoeuvre in regular waves, $\lambda/L_{pp} = 0.5$ and $H = 2$ m. Surge velocities are presented on the left hand side and sway velocities on the right side

Figure 5.7 shows the computed and measured turning circle manoeuvres in a regular wave, $\lambda/L_{PP} = 0.68$, for two different wave heights. In both cases the direction of the wave propagation is $\beta = 180°$. The turning circle manoeuvre of the ship in a wave of $H = 2$ m is plotted on the left and of $H = 4$ m on the right side.

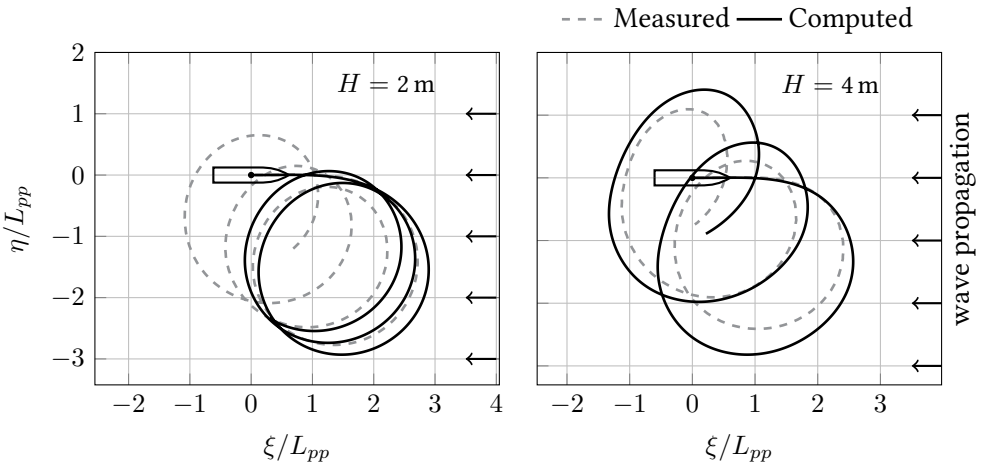

Figure 5.7: DTC turning circle manoeuvre in regular waves, $\lambda/L_{pp} = 0.68$, for wave heading angle of 180° and two wave heights 2 m (left) and 4 m (right).

It can be seen from Figures 5.5 and 5.7 that the second order wave forces determine the direction (twist) of the ship's drift. The amplitude of the drift or the position of the ship over time is determined by the accurate modelling of the forces, which allows an accurate prediction of the ship's velocities. In this sense, the modelling of the propeller and engine dynamics becomes an important task for the simulation of manoeuvring in waves, as the thrust force affects the ship differently at different relative headings. However, the modelling of propeller forces should take into account the propeller thrust deduction and the wake fraction in waves—curvilinear motion in waves.

6 Discussion and conclusions

The study presented in this thesis is situated within two major transformations in the shipping industry. On the one hand, the IMO is pushing for more efficient ships to reduce carbon emissions of the shipping industry. On the other hand, the aim of developing autonomous ships is driving the creation of new technologies and research. The former is being promoted mainly for seagoing ships and the latter for inland waterway ships. The convergence of these two transformations will create the ships of the future, which aim to be autonomous and highly energy efficient to minimize the production of harmful gases.

These two transformations require a better understanding of the behaviour of ships in realistic environments. This is the task of ship dynamics, which, due to its complexity, has been divided into the fields of seakeeping and manoeuvring. In recent years, however, efforts have been made to unify these two fields. This is not easy, because of the many complexities involved. However, with such a theory it would be possible, for example, to simultaneously study the ship's motions during manoeuvres in a seaway and in shallow water, as is the case when manoeuvring in coastal areas. The aim of this thesis was to contribute to this development by, first, developing a mathematical model for an inland waterway vessel manoeuvring in shallow water and, second, developing a mathematical model for manoeuvring in waves. What follows is the general discussion of the work done in the thesis to achieve this objective. This is followed by the conclusions and, finally, by an outlook.

6.1 General discussion

The objective of the thesis was to contribute to an accurate modelling of manoeuvring forces leading to a better numerical prediction of ship manoeuvring under realistic environmental conditions. Two realistic conditions were considered: manoeuvring in shallow water and manoeuvring in waves. However, the latter condition was limited to manoeuvring in regular waves, which, strictly speaking, is not a realistic condition, but serves as a starting point for testing new theories and numerical methods.

The thesis produced two mathematical models, one for manoeuvring in shallow water and another for manoeuvring in regular waves. These mathematical manoeuvring models depend on the accurate representation of hydrodynamic forces acting on the ship during the rudder manoeuvre. These forces are represented as mathematical expressions dependent on kinematic parameters and rudder angle. Note that such a strong simplification of the hydrodynamic forces inherently introduces errors. However, the mathematical modelling aims to capture the main features of the manoeuvring phenomena involved.

The research and developments presented in this thesis have been guided by three factors: simple methods, accurate results and computational efficiency. These guiding factors were usually expressed in terms of whether the forces could be calculated using a simple method while maintaining good accuracy, or whether the calculations could be made faster while maintaining the same accuracy.

The study started with a careful review of the literature on shallow water manoeuvring and manoeuvring in waves, both summarized in Chapter 1. This review showed that manoeuvring force calculations for inland waterway ships were behind current calculations for seagoing ships, especially when considering the interactions between hull, propeller(s) and rudder(s). For the case of manoeuvring in waves, there are two main methods available: the two-time scale method and the unified method. I believe that the unified method has more potential for generalizing the problem; however, the two-time scale method is a good practical approach. The aim here was to critically review the assumptions made in seakeeping and manoeuvring predictions, to identify incompatibilities in their unification, and to develop a mathematical model for manoeuvring in regular waves based on these findings.

Chapter 2 presents a detailed derivation of the equations of motion. Two coordinate systems were chosen to describe the equations: an inertial earth fixed coordinate system and a non-inertial body-fixed coordinate system. In manoeuvring, a representation of the equations of motion in the body-fixed coordinate system is commonly used. Seakeeping, however, uses an inertial coordinate system moving at the ship's average speed. The seakeeping coordinate system is only useful when the ship is travelling straight ahead. It is, therefore, not useful for manoeuvring in waves. The equations of motion in the body-fixed coordinate system for all degrees of freedom are presented in Section 2.3.4. Alternatively, the equations of motion derived in the earth fixed coordinate system are presented in Section 2.3.5. Both representations of the equations of motion are equivalent, and both include all inertial nonlinear terms. The equations of motion in the body-fixed coordinate system were used for the mathematical manoeuvring model in shallow water, while, the equations of motion in the earth fixed coordinate system were used for the

manoeuvring model in waves. The reasons for this choice were based on the ability to describe wave forces and environmental constraints directly in the earth fixed coordinate system.

The external forces acting on the ship were divided into three components: hydrodynamic, hydrostatic and gravitational forces. The focus was on the hydrodynamic forces, in particular, the manoeuvring hydrodynamic forces. I reviewed the available mathematical models and found that two distinct groups of models coexist: Abkowitz-type models and modular models. Due to their flexibility, modular models can simulate a wider range of manoeuvres, and they are widely used in manoeuvring simulators. Abkowitz-type models are only suitable for manoeuvres close to the equilibrium condition for which they were derived, but they tend to be more accurate than modular models because the interactions between hull, propeller, and rudder are implicitly taken into account. I have chosen an Abkowitz-type model for this study because inland waterway ships have complex propulsion systems with ducted propellers and twin-rudders, for which the flow interactions must be accurately captured. The procedure for determining the hydrodynamic coefficients of an Abkowitz-type model is well known. Experimentally, this consists of captive steady tests and planar motion mechanism tests. Numerically, the captive and the planar motion tests are reproduced using RANS-based simulations. I have followed this procedure and improved some computational aspects of the method as well as the method itself, which are discussed below. The coding of the equations of motion was done for 6DoF. However, most of the calculations were done for 3DoF ship motions.

Chapter 3 briefly describes the numerical methods used in this research. Due to the different nature of the hydrodynamic forces, it is more convenient to use simplified methods to exploit their particular characteristics. For instance, viscosity plays a negligible role in wave forces and can, therefore, be calculated faster using potential flow methods. Nevertheless, the main numerical method used was based on the numerical solution of the Reynold-Averaged Navier-Stokes equations.

Chapters 4 and 5 present the main contributions of this thesis. Two mathematical models were proposed: one for manoeuvring in shallow water (Chap. 4) and another for manoeuvring in regular waves (Chap. 5). The accuracy of the models is related to the accurate modelling of the manoeuvring forces and the wave forces. Two methods were proposed to identify the hydrodynamic coefficients: a direct system identification based on RANS captive tests and an indirect system identification based on the measured free running manoeuvring tests. The latter model has the potential to be applied to full-scale ships. In addition, a new method for calculating the added mass coefficients was

presented. This method is accurate, fast and avoids the use of planar motion mechanism tests. The main contributions presented in Chapters 4 and 5 are discussed in detail below.

6.1.1 Mathematical model for manoeuvring in shallow water

An Abkowitz-type mathematical model for shallow water manoeuvring of inland waterway ships was developed and presented in Section 4.1. The mathematical model is capable of predicting manoeuvres in moderate water depth and extreme shallow waters. Differing from previous models, the complete terms of added mass coefficients for 3DoF were considered. It was surprising that these terms were not present in the Abkowitz-type models, but they are present in the modular models. The velocity dependent hydrodynamic coefficients were based on Mucha's mathematical model. Additional nonlinear terms were added by physical observation of experimental and numerical captive tests. The model was tested with the RIW ship, which has two ducted propellers and twin-rudders behind each propeller.

The validation of the mathematical model showed that the model is able to reproduce the zig-zag manoeuvres even in extreme shallow waters of $h/T = 1.2$. The model has all the limitations of an Abkowitz-type model, i.e., that only manoeuvres close to the reference speed are accurate, and the propeller rotation rate is kept constant during the manoeuvre. This is perhaps the main limitation of the Abkowitz methods and why their use has been restricted to specific study cases. However, with new developments in autonomous ship operation and collision avoidance, where high accuracy is required, the use of this method is being revived.

6.1.2 Added mass at zero frequency

Current manoeuvring theory specifies that the added mass coefficients should be obtained at zero frequency. Numerically, the state-of-the-art methods for obtaining the added mass coefficients are based on virtually reproducing the planar motion mechanism tests with unsteady RANS. Such calculations require the use of small oscillatory frequencies, on the assumption that these added masses are close enough to the zero-frequency value—which is a valid assumption. Despite advances in high-performance computing, numerical PMM tests based on solving the unsteady Reynolds-averaged Navier-Stokes equations are time-consuming. The velocity-dependent hydrodynamic coefficients can be obtained efficiently using steady RANS. However, the calculation of the added mass coefficients is responsible for the disproportionately long computation times.

In Section 4.1 a new method for calculating the added mass coefficients at zero frequency was presented. Using Euler equations, the hull is impulsively accelerated over a single time step. As the computation is performed over only one time step, the computational time is about three orders of magnitude faster than virtual PMM approaches. Furthermore, the method proved reliable in both deep and shallow water. This is particularly important as it has been reported that these coefficients are difficult to obtain under shallow water conditions. The introduction of this method helps to avoid the computations of numerical PMM tests based on the solution of unsteady Reynolds-averaged Navier-Stokes equations. This change is huge, and in this thesis all the added mass coefficients were calculated using this approach. Furthermore, this method has been effectively used and combined with the indirect system identification method.

The validity of the method was tested on ships with low Froude numbers ($F_n \leq 0.1$), for which the free surface has a negligible effect and can, therefore, be simplified as a flat, non-deforming surface. At high Froude numbers, the free surface has an effect on the added mass coefficients. I attempted to include the free surface effect, but the volume of fluid (VOF) technique, which is a capturing method, was not able to resolve the free surface accurately. The reason may be that this method does not apply the kinetic and dynamic boundary conditions directly to the free surface. It seems that a tracking method will be more suitable for this purpose. In such a method, the dynamic and kinetic boundary conditions can be imposed directly on the free surface. Nevertheless, the use of this method is justified as ship masters perform manoeuvres at moderate speeds when navigating in shallow water as well as in waves. For instance, both benchmark cases presented have a reference speed below $F_n \leq 0.1$.

6.1.3 Viscous flow computations

The accuracy of the mathematical models relies greatly on the accurate determination of the hydrodynamic coefficients. In the previous section I discussed how accurately calculate the added mass coefficients. In this section, the discussion focuses on the accurate calculation of the coefficients that are proportional to the velocities.

The current state-of-the-art methods for calculating velocity dependent hydrodynamic coefficients are based on steady RANS of captive manoeuvring tests, such as rudder, drift or rotating arm tests. However, for inland waterway ships, the literature review showed that they are mainly obtained from captive model tests. Numerical calculations of captive tests with fully-appended inland waterway ships were not available in the literature. One reason for this may be the complex stern geometries of these ships, which accommodate

complex propulsion systems. For instance, the stern of the RIW ship has tunnels that direct the flow to ducted propellers and fish tail twin-rudders behind each propeller.

I presented a method for the computation of captive tests of inland waterway ships, including the interaction between hull, ducted propellers, and twin-rudders. The simulation setup includes a physical representation of all parts, allowing the interaction between all geometric parts of the ship to be implicitly captured. The vertical motion of the ship is accounted for by a mesh deformation algorithm known as morphing. For this type of simulation, the computational time is significantly higher, and ways to improve the convergence and reduce the computational time were investigated. First, I proposed an artificial horizontal gravity as a way to ramp up the speed in the numerical domain. This simple method allows a smooth transition from zero velocity to the desired velocity, avoiding the generation of large waves. This method proved to be particularly useful in constrained space, where an incorrect initial condition produces large waves that reflect on walls.

For ship speeds below $F_n \leq 0.1$ the effects of the free surface elevation can be neglected. Only modelling the water speeds up the calculations. However, even at low speeds in shallow water, the bottom causes the ship to sink and trim, but the trim magnitudes for inland waterway ships were negligible. An iterative re-meshing procedure for the double-body simulation was developed to account for the sinkage effect. With this procedure, the calculation of the forces of a single captive test takes less than one hour (in a 48-core cluster). This re-meshing method achieves a similar level of accuracy as a free surface modelling.

Another important aspect studied was the modelling of turbulence in shallow water. Previous studies showed that, in shallow water, the flow around the ship's hull is unsteady, swirling and contains asymmetric eddies. In current practice, the k-ω SST turbulence model is used to close the RANS system of equations. However, its validity for shallow water hydrodynamics has been questioned, particularly for the prediction of the longitudinal force, where the hull-propeller-rudder interaction appears to be more dependent on viscous forces. The Reynolds stress model (RSM) was tested, and it was found that only the longitudinal force showed a significant difference from the forces calculated with the k-ω SST model. In the absence of experimental tests, it is difficult to judge which turbulence model is closer to reality. One difficulty with the RSM is that the system of equations becomes stiff, leading to convergence difficulties. In practice this means that a high quality mesh with smooth transitions is required. For this reason, I could only use the RSM turbulence model for the double-body re-meshing approach. For the free surface simulation, the number of control volumes was excessive.

6.1.4 Data-driven system identification

An alternative method to obtain the hydrodynamic coefficients was proposed in Section 4.5. The method was formulated as a data-driven approach using the equations of motion directly. The method relies on free-running manoeuvring measurements of velocities and accelerations. If direct measurements of these parameters are not available, they can be calculated by numerical differentiation of the ship's trajectory and heading angle. The measured rudder angles are always required.

Most indirect system identification methods focused on improving the regression problem. Sophisticated algorithms were tested, but could not produce reliable, accurate hydrodynamic coefficients. My approach was different in that I wanted to introduce more physical insight into the system identification procedure. A close analysis of the equations used for the system identification showed that they were dependent on the accuracy of the added mass coefficients. Furthermore, the physical knowledge of the hydrodynamic forces was not used in the procedure. To overcome this problem, I proposed two modifications to the method. First, I calculated the added mass accurately using the new Euler based method. Second, the physical knowledge of the hydrodynamic forces was added to the regression in the form of constraints.

These two implementations ensured that the coefficients are physically plausible. The method still depends on the quality of the data. I have found that the main requirement to obtain reliable nonlinear coefficients is to have a large variation of the parameters in the measurement records. One way to obtain this large variation is to perform different kinds of manoeuvres with large rudder angles. The method was tested with free-running manoeuvring tests conducted in environmentally controlled hydrodynamic laboratories. Its validity has yet to be tested with full-scale trials, where additional environmental excitation is always present.

6.1.5 Mathematical model for manoeuvring in regular waves

A mathematical model for manoeuvring in waves was presented in Chapter 5. The hydrodynamic forces were divided into wave contributions and calm water manoeuvring contributions. The model considered only the second-order wave forces. The equations of motion were solved in the inertial coordinate system rather than in the body-fixed coordinate system as is usually done. The aim was to use a general coordinate system in which the equations of motion are valid and the wave propagation can be described directly. The model gives adequate results for some manoeuvres, in particular for the ship starting the manoeuvre in head waves. For others, the errors are large. The method only

captures the main features of the manoeuvre, such as the drifting direction. In general, the accuracy of the method seems to be similar to the state-of-the-art methods.

The inclusion of first-order forces could improve the results, but certainly not to the extent of matching the experimental results. A deeper phenomenon is missing. A thorough analysis of the validity of the equations should shed some light on the problem. For instance, the added mass coefficients for manoeuvring are calculated at zero frequency, but in seakeeping the added mass coefficients should be calculated at infinite frequency. When using the added mass coefficients at infinite-frequency, the convolution integral component should not be ignored.

The propeller thrust during ship manoeuvring in waves was found to be inconsistent with the modelling assumption that the propeller rotation rate should be constant. The experimental ship manoeuvring in waves was carried out at a constant initial speed of 6 knots, i.e., the propeller rpm was adjusted accordingly to achieve the same speed, regardless of the wave direction. It is, therefore, advisable to introduce the propeller rpm as a parameter in the mathematical model and to model the thrust separately from the hull forces. At this stage, the model for manoeuvring in regular waves provides only a qualitative analysis.

6.2 Conclusion

The current research aimed to accurately model the hydrodynamic forces during manoeuvring in shallow water and manoeuvring in regular waves.

A mathematical model for manoeuvring in shallow waters of inland waterway ships was proposed. The complete added mass coefficients for 3DoF were considered. The model was validated against experimental free running tests carried out at low speeds of $F_n \leq 0.1$. The mathematical model prediction of the ship's trajectory and the kinematic parameters correlates well with the corresponding measured values. The model was even able to predict the zig-zag manoeuvre in extreme shallow waters. As the mathematical model relies on accurate force calculation, two methods were proposed for identifying the hydrodynamic coefficients, namely, a direct system identification based on captive RANS calculations and an indirect system identification based on free running tests.

The identification of the hydrodynamic coefficients was separated into velocity and acceleration dependent coefficients. The added mass coefficients are only acceleration dependent. A new method for calculating the added masses was developed and validated. The validation showed that the added mass coefficients can be obtained accurately within 1% error with respect to the analytical solution. The method is fast and reliable in

both deep and shallow water. It is, therefore, suitable for replacing the time-consuming calculations based on the planar motion mechanism and saves time and computational resources. The method was well suited for both direct and indirect system identification methods.

RANS-based captive tests are challenging in shallow water, and even more so for ships with complex propulsion systems, such as the inland waterway ships travelling on the Rhine River. From a numerical point of view, shallow water flow calculations are computationally demanding. I have proposed two numerical techniques to reduce the computational time. First, by improving the initial condition using a horizontal artificial gravity, thereby allowing a smooth increase in velocity from zero to the desired velocity. Second, when the free surface is not deformed due to the slow speed, the sinkage and trim is mainly induced by the shallow water bottom. Thus, a double-body simulation was proposed, which iteratively solves the sinkage and re-meshes the numerical domain. This method is computationally more efficient and gives an accuracy similar to that obtained by modelling the free surface. It was also found that there is a significant difference in the longitudinal force, depending on whether the k-ω SST or the RSM turbulence model is chosen.

As an alternative to the direct system identification, an indirect system identification approach was developed to obtain the manoeuvring hydrodynamic coefficients from measured free running manoeuvring tests. Accurate hydrodynamic coefficients can be obtained using measured ship kinematic parameters and rudder angle. Physical knowledge of the hydrodynamic forces and accurate added mass coefficients are key components in obtaining reliable plausible hydrodynamic coefficients. Incorporating these two key components resulted in a simple robust method. The method requires large variations in kinematic parameters to obtain accurate nonlinear coefficients.

Finally, a mathematical model for manoeuvring in regular waves was developed. The ship dynamics were solved in the inertial coordinate system, where spatial constraints and wave elevation can be directly described. The inclusion of waves in the manoeuvring analysis introduces three main parameters to be considered: wave frequency, wave amplitude and wave propagation direction. The model presented here is able to provide a good quantitative analysis for manoeuvring in head waves. For other initial wave propagation directions, only a qualitative analysis is possible, e.g., prediction of the ship's drift direction. For a general quantitative analysis, fundamental improvements in the equations of motion and the propulsion modelling are required.

6.3 Outlook

Based on the present study, three future research directions are recommended.

First, the calculation of the added masses can be further generalized by including the boundary conditions directly on the free surface. When using the finite volume method with Euler equations, the free surface was simplified as a flat plane. As the VOF capturing method was inadequate to resolve the free surface, a tracking method seems to be more appropriate. With this kind of method, the kinematic and dynamic boundary conditions can be enforced directly on the free surface.

Second, the main limitation of an Abkowitz-type model is that the propeller rotation rate cannot be changed once the coefficients were determined. One possibility to overcome this limitation is to additionally model the thrust. This means having a model for X, Y, N, and T. This division is only mathematical, i.e., the captive tests should still be performed with the ship fully appended to account for the flow interaction between hull, propeller and rudder.

Third, it is important to find consistent equations of motion for manoeuvring in waves. For this, the behaviour of the added mass seems to be relevant. Added masses in manoeuvring are taken at zero frequency, but in seakeeping they are taken at infinite-frequency. This seems to suggest that a generalized expression for the added mass is needed in such a way that, when the ship is sailing in calm water, the added mass is reduced to a zero-frequency added mass, and when there are waves, it takes the form of the infinite added mass.

A Skew symmetric matrix and vector cross product

A vector cross product can be represented as a matrix-vector multiplication. For instance, let's have two vectors $\mathbf{a}, \mathbf{b} \in \mathbb{R}^3$, with components $\mathbf{a} = (a_1, a_2, a_3)^\intercal$ and $\mathbf{b} = (b_1, b_2, b_3)^\intercal$. The cross product $\mathbf{a} \times \mathbf{b}$ can be expressed as the skew symmetric matrix $\mathbf{S_w}(\mathbf{a})$ of the first vector multiplied by the second vector

$$\mathbf{a} \times \mathbf{b} = \mathbf{S_w}(\mathbf{a})\mathbf{b} \tag{A.1}$$

where $\mathbf{S_w}(\mathbf{a})$ and $\mathbf{b}$ are

$$\mathbf{S_w}(\mathbf{a}) = \begin{bmatrix} 0 & -a_3 & a_2 \\ a_3 & 0 & -a_1 \\ -a_2 & a_1 & 0 \end{bmatrix} \quad \text{and} \quad \mathbf{b} = \begin{bmatrix} b_1 \\ b_2 \\ b_3 \end{bmatrix} \tag{A.2}$$

Proving the above equation is straightforward, making the matrix and vector multiplication we will find the same expression as the cross vector product. Some important properties of the skew symmetric matrix are:

1. $\mathbf{S_w}(\mathbf{a}) = -[\mathbf{S_w}(\mathbf{a})]^\intercal$
2. $[\mathbf{S_w}(\mathbf{a})]^2 = \mathbf{S_w}(\mathbf{a})\mathbf{S_w}(\mathbf{a}) = [\mathbf{S_w}(\mathbf{a})][\mathbf{S_w}(\mathbf{a})]^\intercal - |\mathbf{S_w}(\mathbf{a})|^2\mathbf{I}$
3. $|\mathbf{S_w}(\mathbf{a})|^2 = \mathbf{trace}[\mathbf{S_w}(\mathbf{a})\mathbf{S_w}(\mathbf{a})^\intercal]$, where **trace** is the sum of the diagonal elements.

B Nondimensionalization

Comparison of forces and other ship related parameter are commonly carried with non-dimensional variables. The two conventions for non-dimensionalizing these variables are known as Prime System I and Prime System II. Table B.1 lists these non-dimensional variables and their associated parameters. Where the symbol U is the instantaneous ship speed, L is the ship's characteristic length, T is the ship's draft, and ρ is the density of the fluid. In the thesis I followed the Prime System I convention.

Table B.1: Normalized variables and parameters used for Prime System I and Prime System II

Variable	Prime System I	Prime System II
Length	L	L
Mass	$0.5\rho L^3$	$0.5\rho L^2 T$
Inertia moment	$0.5\rho L^5$	$0.5\rho L^4 T$
Time	L/U	L/U
Reference Area	L^2	LT
Position	L	L
Angle	1	1
Linear velocity	U	U
Angular velocity	U/L	U/L
Linear acceleration	U^2/L	U^2/L
Angular acceleration	U^2/L^2	U^2/L^2
Force	$0.5\rho U^2 L^2$	$0.5\rho U^2 LT$
Moment	$0.5\rho U^2 L^3$	$0.5\rho U^2 L^2 T$

Bibliography

Abkowitz, Martin A. (1964). *Lectures on Ship Hydrodynamics – Steering and Manoeuvrability*. Report No. Hy-5. Hydro-Og Laboratorium.

– (1969). *Stability and Motion Control of Ocean Vehicles*. The MIT Press. ISBN: 978-0-262-51006-6.

Ahnert, Karsten and Markus Abel (2007). "Numerical differentiation of experimental data: local versus global methods". In: *Computer Physics Communications* 177.10, pp. 764–774. ISSN: 00104655. DOI: 10.1016/j.cpc.2007.03.009.

Branch, Mary Ann, Thomas F. Coleman, and Yuying Li (1999). "A subspace, Interior, and Conjugate Gradient Method for Large-Scale Bound-Constrained Minimization Problems". In: *SIAM Journal on Scientific Computing* 21.1, pp. 1–23. ISSN: 1064-8275, 1095-7197. DOI: 10.1137/S1064827595289108.

Burmester, Simon, Guilherme Vaz, and Ould el Moctar (Aug. 1, 2020). "Towards credible CFD simulations for floating offshore wind turbines". In: *Ocean Engineering* 209, p. 107237. ISSN: 0029-8018. DOI: 10.1016/j.oceaneng.2020.107237.

Cao, Yusong, William W. Schultz, and Robert F. Beck (1991). "Three-dimensional desingularized boundary integral methods for potential problems". In: *International Journal for Numerical Methods in Fluids* 12.8, pp. 785–803. ISSN: 1097-0363. DOI: 10.1002/fld.1650120807.

Carrica, Pablo, Farzad Ismail, Mark Hyman, Shanti Bhushan, and Frederick Stern (2013). "Turn and zigzag maneuvers of a surface combatant using a URANS approach with dynamic overset grids". In: *Journal of Marine Science and Technology* 18.2, pp. 166–181. ISSN: 1437-8213. DOI: 10.1007/s00773-012-0196-8.

Clarke, David (2003). "The foundations of steering and manoeuvring". In: *Proceedings of the IFAC conference on manoeuvering and controlling marine crafts*. Girona, Spain.

Cura-Hochbaum, Andrés (2006). "Virtual PMM Tests for Manoeuvring Prediction". In: 26th ONR Symposium on Naval Hydrodynamics. Rome, Italy.

Cura-Hochbaum, Andrés and Sebastian Uharek (2016). "Prediction of ship manoeuvrability in waves based on RANS simulations". In: *31st Symposium on Naval Hydrodynamics*. Monterey, California.

el Moctar, Ould (2001). "Numerical computations of flow forces in ship manoeuvring". In: *Ship Technology Research* 48, pp. 98–123.

el Moctar, Ould, Udo Lantermann, Philipp Mucha, Jens Höpken, and Thomas E. Schellin (2014). "RANS-Based Simulated Ship Maneuvering Accounting for Hull-Propulsor-Engine Interaction". In: *Ship Technology Research* 61.3, pp. 142–161. ISSN: 0937-7255. DOI: 10.1179/str.2014.61.3.003.

el Moctar, Ould, Thomas E. Schellin, and Heinrich Söding (2021). *Numerical Methods for Seakeeping Problems*. Springer International Publishing. ISBN: 978-3-030-62560-3. DOI: 10.1007/978-3-030-62561-0.

el Moctar, Ould, Vladimir Shigunov, and Tobias Zorn (2012). "Duisburg Test Case: Post-Panamax Container Ship for Benchmarking". In: *Ship Technology Research* 59.3, pp. 50–64. DOI: 10.1179/str.2012.59.3.004.

Eloot, Katrien (2006). "Selection, experimental determination and evaluation of a mathematical model for ship manoeuvring in shallow water". ISBN: 9789085780922. dissertation. Ghent University.

Ferziger, Joel H., Milovan Peric, and Robert L. Street (2020). *Computational Methods for Fluid Dynamics*. 4th ed. Springer International Publishing. ISBN: 978-3-319-99691-2. DOI: 10.1007/978-3-319-99693-6.

Fournarakis, Nikos, Apostolos Papanikolaou, Dionysia Chroni, Shuukui Liu, and Timoleon Plessas (2016). "Estimation of the maneuvering characteristics of the DTC containership using URANS based simulations". In: *Maritime Technology and Engineering III: Proceedings of the 3rd International Conference on Maritime Technology and Engineering*. Lisbon, Portugal.

Gronarz, Andreas (1997). "Rechnerische Simulation der Schiffsbewegung beim Manövrieren unter besonderer Berücksichtigung der Abhängigkeit der Wassertiefe". in German. PhD thesis. Gerhard-Mercator-Universität - Gesamthochschule Duisburg.

He, Shi, Paula Kellett, Zhiming Yuan, Atilla Incecik, Osman Turan, and Evangelous Boulougouris (2016). "Manoeuvring prediction based on CFD generated derivatives". In: *Journal of Hydrodynamics* 28.2, pp. 284–292. ISSN: 1878-0342. DOI: 10.1016/S1001-6058(16)60630-3.

Hirano, Masayoshi, Junshi Takashina, Yoshifumi Takaishi, and Toshihiko Saruta (1980). "Ship Turning Trajectory in regular waves". In: *Publication of: West Japan Society of Naval Architects* 60.

Imlay, Frederick (1961). *The Complete Expressions for "Added Mass" of a Rigid Body Moving in an Ideal Fluid*. 1528. David Taylor Model Basin.

ITTC, The Specialist Committee on Manoeuvring in Waves (2021). *Final Report and Recommendations to the 29th ITTC*.

Jin, Yuting, Jonathan Duffy, Shuhong Chai, and Allan R. Magee (2019). "DTMB 5415M dynamic manoeuvres with URANS computation using body-force and discretised propeller models". In: *Ocean Engineering* 182, pp. 305–317. ISSN: 0029-8018. DOI: 10.1016/j.oceaneng.2019.04.036.

Kaidi, S., H. Smaoui, and P. Sergent (2018). "CFD Investigation of Mutual Interaction between Hull, Propellers, and Rudders for an Inland Container Ship in Deep, Very Deep, Shallow, and Very Shallow Waters". In: *Journal of Waterway, Port, Coastal, and Ocean Engineering* 144.6. Publisher: American Society of Civil Engineers, p. 04018017. DOI: 10.1061/(ASCE)WW.1943-5460.0000458.

Kim, Daejeong, Tahsin Tezdogan, and Atilla Incecik (2022). "Hydrodynamic analysis of ship manoeuvrability in shallow water using high-fidelity URANS computations". In: *Applied Ocean Research* 123, p. 103176. ISSN: 0141-1187. DOI: 10.1016/j.apor.2022.103176.

Kim, Dong Jin, Kunhang Yun, Jong-Yong Park, Dong Jin Yeo, and Yeon Gyu Kim (2019). "Experimental investigation on turning characteristics of KVLCC2 tanker in regular waves". In: *Ocean Engineering* 175, pp. 197–206. ISSN: 00298018. DOI: 10.1016/j.oceaneng.2019.02.011.

Korotkin, Alexandr I. (2009). *Added Masses of Ship Structures*. Red. by R. Moreau. Vol. 88. Fluid Mechanics and Its Applications. Dordrecht: Springer Netherlands. ISBN: 978-1-4020-9431-6 978-1-4020-9432-3. DOI: 10.1007/978-1-4020-9432-3.

Letki, L. and D. A. Hudson (2005). *Simulation of ship manoeuvring performance in calm water and waves*. Ship Scienvce Report. University of Southampton, Southampton, UK, p. 106.

Liu, Jialun (2017). "Impacts of rudder configurations on inland vessel manoeuvrability". ISBN: 9789462335622. Dissertation (TU Delft). DOI: 10.4233/uuid:bef6c12f-5804-407b-a4c6-f7949541f21c.

Lu, Suli, Xide Cheng, Jialun Liu, Shijie Li, and Hironori Yasukawa (2022). "Maneuvering modeling of a twin-propeller twin-rudder inland container vessel based on integrated CFD and empirical methods". In: *Applied Ocean Research* 126, p. 103261. ISSN: 0141-1187. DOI: 10.1016/j.apor.2022.103261.

Luo, Weilin (2016). "Parameter Identifiability of Ship Manoeuvring Modeling Using System Identification". In: *Mathematical Problems in Engineering* 2016. Publisher: Hindawi, e8909170. ISSN: 1024-123X. DOI: 10.1155/2016/8909170.

Lurie, A.I. (2002). *Analytical Mechanics*. Springer Berlin Heidelberg. ISBN: 9783540456773.

Lyu, Wenjing and Ould el Moctar (2017). "Numerical and experimental investigations of wave-induced second order hydrodynamic loads". In: *Ocean Engineering* 131.Supplement C, pp. 197–212. ISSN: 0029-8018. DOI: https://doi.org/10.1016/j.oceaneng.2016.11.047.

Menter, F. R. (1994). "Two-equation eddy-viscosity turbulence models for engineering applications". In: *AIAA Journal* 32.8, pp. 1598–1605. ISSN: 0001-1452, 1533-385X. DOI: 10.2514/3.12149.

Mewes, Simon (2021). "Numerical prediction of Hydrodynamic Damping and Loads on a Floating Offshore Wind Turbine". PhD thesis. University of Duisburg-Essen.

Moukalled, F., L. Mangani, and M. Darwish (2016). *The Finite Volume Method in Computational Fluid Dynamics: An Advanced Introduction with OpenFOAM® and Matlab*. Fluid Mechanics and Its Applications. Springer International Publishing. ISBN: 978-3-319-16873-9. DOI: 10.1007/978-3-319-16874-6.

Mucha, Philipp (2017). "On Simulation-based Ship Maneuvering Prediction in Deep and Shallow Water". PhD thesis. University of Duisburg-Essen.

Mucha, Philipp, Thorsten Dettmann, Victor Ferrari, and Ould el Moctar (Feb. 1, 2019). "Experimental investigation of free-running ship manoeuvers under extreme shallow water conditions". In: *Applied Ocean Research* 83, pp. 155–162. ISSN: 0141-1187. DOI: 10.1016/j.apor.2018.09.008.

Mucha, Philipp, Ould el Moctar, Thorsten Dettmann, and Matthias Tenzer (May 4, 2017). "Inland waterway ship test case for resistance and propulsion prediction in shallow water". In: *Ship Technology Research* 64.2, pp. 106–113. ISSN: 0937-7255. DOI: 10.1080/09377255.2017.1349723.

Muzaferija, Samir and Milovan Peric (1999). "Computation of free surface flows using interface-tracking and interface-capturing methods". In: *Nonlinear Water Wave Interaction*. Computational Mechanics Publications. Southampton: WIT Press, pp. 59–100. ISBN: 978-1-85312-545-4.

Newman, John Nicholas (2018). *Marine hydrodynamics*. 40th anniversary edition. Cambridge: MIT press. ISBN: 978-0-262-53482-6.

Norrbin, Nils (1960). *A study of course keeping and maneuvering performance*. Report 45. Göteborg, Sweden: Swedish State Shipbuilding Experimental Tank.

– (1971). *Theory and observations on the use of a mathematical model for ship manoeuvring in deep and confined waters*. Report 68. Swedish State Shipbuilding Experimental Tank.

Oberhagemann, Jan (2016). "On prediction of wave-indusced loads and vibration of ship structures with finite volume fluid dynamic methods". PhD thesis. University of Duisburg-Essen.

Oltmann, Peter and Som Deo Sharma (1984). *Simulation of combined engine and rudder maneuvers using an improved model of hull-propeller-rudder interactions*. TUHH Universitätsbibliothek. DOI: 10.15480/882.929.

Quadvlieg, Frans and Joris Brouwer (2011). "KVLCC2 benchmark data including uncertainty analysis to support manoeuvring predictions". In: pp. 325–338.

Sanada, Yugo, Haitham Elshiekh, Yasuyuki Toda, and Frederick Stern (2019). "ONR Tumblehome course keeping and maneuvering in calm water and waves". In: *Journal of Marine Science and Technology* 24.3, pp. 948–967. ISSN: 0948-4280, 1437-8213. DOI: 10.1007/s00773-018-0598-3.

Shigunov, Vladimir, Ould el Moctar, Apostolos Papanikolaou, Robert Potthoff, and Shukui Liu (2018). "International benchmark study on numerical simulation methods for prediction of manoeuvrability of ships in waves". In: *Ocean Engineering* 165, pp. 365–385. ISSN: 0029-8018. DOI: 10.1016/j.oceaneng.2018.07.031.

Siemens Digital Industries Software (2021). *Simcenter STAR-CCM+*. Version 2021.3.

Sigmund, Sebastian and Ould el Moctar (2018). "Numerical and experimental investigation of added resistance of different ship types in short and long waves". In: *Ocean Engineering* 147.Supplement C, pp. 51–67. ISSN: 0029-8018. DOI: https://doi.org/10.1016/j.oceaneng.2017.10.010.

Skejic, Renato (2013). "Ships Maneuvering Simulations in a Seaway: How close are we to reality?" In: IWNTM13: International Workshop on Nautical Traffic Models 2013.

Söding, Heinrich (1993). "A method for accurate force calculations in potential flow". In: *Ship Technology Research* 40, pp. 176–186.

Söding, Heinrich, Vladimir Shigunov, Thomas E. Schellin, and Ould el Moctar (2014). "A Rankine Panel Method for Added Resistance of Ships in Waves". In: *Journal of Offshore Mechanics and Arctic Engineering* 136.3. ISSN: 0892-7219. DOI: 10.1115/1.4026847.

Söding, Heinrich, Alexander von Graefe, Ould el Moctar, and Vladimir Shigunov (Aug. 23, 2013). "Rankine Source Method for Seakeeping Predictions". In: ASME 2012 31st International Conference on Ocean, Offshore and Arctic Engineering. American Society of Mechanical Engineers Digital Collection, pp. 449–460. DOI: 10.1115/OMAE2012-83450.

Sprenger, Florian, Adolfo Maron, Guillaume Delefortrie, Thibaut van Zwijnsvoorde, Andrés Cura-Hochbaum, Antonio Lengwinat, and Apostolos Papanikolaou (2017). "Experimental Studies on Seakeeping and Maneuverability of Ships in Adverse Weather Conditions". In: *Journal of Ship Research* 61.3, pp. 131–152. ISSN: 0022-4502, 1542-0604. DOI: 10.5957/JOSR.170002.

Stern, F., K. Agdraup, S. Y. Kim, Andrés Cura-Hochbaum, K. P. Rhee, F. Quadvlieg, P. Perdon, T. Hino, R. Broglia, and J. Gorski (2011). "Experience from SIMMAN 2008 — The First Workshop on Verification and Validation of Ship Maneuvering Simulation Methods". In: *Journal of Ship Research* 55.02, pp. 135–147. ISSN: 0022-4502. DOI: 10.5957/jsr.2011.55.2.135.

Sutulo, Serge and Carlos Guedes Soares (2006). "A unified nonlinear mathematical model for simulating ship manoeuvring and seakeeping in regular waves". In: *Proc. Int. Conf. on Marine Simulation and Ship Manoeuvrability (MARSIM)*.

– (2011). "Mathematical models for simulation of manoeuvring performance of ships". In: *Maritime Engineering and Technology*. Ed. by Carlos Guedes Soares, Y. Garbatov, N Fonseca, and AP Teixeira, pp. 661–698.

Tello Ruiz, Manasés, Maxim. Candries, Marc Vantorre, Guillaume Delefortrie, P. Peeters, and F. Mostaert (2012). *Ship manoeuvring in waves: a literature review*. WL Reports 00_096. Antwerp, Belgium: Flanders Hydraulics Research & Ghent University.

Timman, Reinier and John Nicholas Newman (Mar. 1, 1963). "The Coupled Damping Coefficients of a Symmetric Ship". In: *Journal of Ship Research* 6.1, pp. 1–7. ISSN: 0022-4502, 1542-0604. DOI: 10.5957/jsr.1962.6.1.1.

Toxopeus, SL (2011). "Practical application of viscous-flow calculations for the simulation of manoeuvring ships". ISBN: 9789075757057. Dissertation (TU Delft, preparation external). Wageningen: Marin.

von Graefe, Alexander (2014). "A Rankine source method for ship ship interaction and shallow water problems". PhD thesis. University Duisburg-Essen.

Wang, Jianhua and Decheng Wan (2018). "CFD Investigations of Ship Maneuvering in Waves Using naoe-FOAM-SJTU Solver". In: *Journal of Marine Science and Application* 17.3, pp. 443–458. ISSN: 1993-5048. DOI: 10.1007/s11804-018-0042-4.

Wilcox, David C. (1993). *Turbulence modeling for CFD*. La Cãnada, California: DCW Industries, Inc. 460 pp. ISBN: 978-0-9636051-0-8.

Wolff, Karsten (1981). *Ermittlung der Manövriereigenschaften fünf repräsentativer Schiffstypen mit Hilfe von CPMC-Modellversuchen*. TUHH Universitätsbibliothek. DOI: 10.15480/882.841.

Yasukawa, Hironori (2006). "Simulations of Ship Maneuvering in Waves: (1st report: turning motion)". In: *Journal of the Japan Society of Naval Architects and Ocean Engineers* 4.0, pp. 127–136. ISSN: 1880-3717, 1881-1760. DOI: 10.2534/jjasnaoe.4.127.

– (2008). "Simulations of Ship Maneuvering in Waves: (2nd report: zig-zag and stopping maneuvers)". In: *Journal of the Japan Society of Naval Architects and Ocean Engineers* 7.0, pp. 163–170. ISSN: 1880-3717, 1881-1760. DOI: 10.2534/jjasnaoe.7.163.

Yasukawa, Hironori and Yasuo Yoshimura (2015). "Introduction of MMG standard method for ship maneuvering predictions". In: *Journal of Marine Science and Technology* 20.1, pp. 37–52. ISSN: 0948-4280, 1437-8213. DOI: 10.1007/s00773-014-0293-y.

Zentari, Lahbib, Ould el Moctar, Jan Lassen, Rink Hallmann, and Thomas E. Schellin (2022). "Experimental and numerical investigation of shallow water effects on resistance and propulsion of coupled pusher-barge convoys". In: *Applied Ocean Research* 121, p. 103048. ISSN: 0141-1187. DOI: 10.1016/j.apor.2022.103048.

Zentari, Lahbib, Simon Tödter, Ould El Moctar, Jens Neugebauer, and Thomas E. Schellin (2023). "Experimental and numerical investigation of the gap flow between a pusher and a barge in deep and shallow water". In: *Applied Ocean Research* 132, p. 103466. ISSN: 01411187. DOI: 10.1016/j.apor.2023.103466.

Zhang, Wei, Zao-Jian Zou, and De-Heng Deng (2017). "A study on prediction of ship maneuvering in regular waves". In: *Ocean Engineering* 137.Supplement C, pp. 367–381. ISSN: 0029-8018. DOI: https://doi.org/10.1016/j.oceaneng.2017.03.046.

Zwijnsvoorde, Thibaut van, Guillaume Delefortrie, Marc Vantorre, Patrik Peeters, and Frank Mostaert (2015). *SHOPERA: Final Report Model Tests*. WL Reports 12_045. Antwerp, Belgium: Flanders Hydraulics Research & Ghent University.

DOI: 10.17185/duepublico/81271
URN: urn:nbn:de:hbz:465-20231124-161100-8